Advanced Electron Microscopy of Novel Ferromagnetic Materials and Ferromagnet/Oxide Interfaces in Magnetic Tunnel Junctions

By

Fengyuan Shi

A dissertation submitted in partial fulfillment of

the requirements for the degree of

Doctor of Philosophy

(Materials Science)

at the

UNIVERSITY OF WISCONSIN-MADISON

2013

Abstract

We have studied novel ferromagnetic (FM) materials and FM electrode/tunnel barrier interfaces in magnetic tunnel junctions (MTJs) by advanced electron microscopy including scanning transmission electron microscopy (HRSTEM) and electron energy loss spectroscopy (EELS). MTJs are one of the prototypical spintronic devices, with applications in magnetic random access memory, sensors and read heads. The performance of MTJs depends on several factors, including the FM electrodes and the FM/tunnel barrier interfaces. Therefore, to realize the high performance of MTJs, we first need high quality ferromagnetic electrodes with high spin polarization.

High-quality Fe_3O_4 and Fe_4N electrodes with theoretically predicted -100% spin polarization were fabricated by various methods and investigated by HRSTEM and STEM EELS. The Fe_3O_4 and Fe_4N thin films indeed have low defect density and good crystallinity, but when integrated as electrodes in a MTJ, problems emerged. In a $Fe_4N/AlO_x/Fe$ MTJ, the magnetoresistance was negative, but relatively small, due to a defective Fe_3O_4 reaction layer formed at the Fe_4N/tunnel barrier interface revealed by HRSTEM and EELS. The interfacial reaction layer was thin and discontinuous which made the direct imaging difficult. Therefore, STEM EELS was used to map out the reaction layer. A Fe_3O_4 reaction layer was also found in a nominally symmetric $CoFe/AlO_x/CoFe$ MTJs after annealing, which also exhibited inverse TMR and a non-symmetric bias dependence.

We also investigated the MTJs with the Heusler alloy Co_2MnSi as one or both electrode and crystalline MgO as the tunnel barrier, which exhibit quite high TMR due to coherent tunneling. We showed that the Co_2MnSi/MgO interface in these junctions is dominated by a configuration of a pure Mn plane bonded across the interface to O. This was the first observation

of that interface termination. The MnMn/O interface termination has 100% spin polarization which explains in part the high TMR in the junctions, especially at room temperature. HRSTEM images also show that the fraction of MnMn/O interface termination increases with increasing Mn concentration in the CMS electrode.

Acknowledgement

I would like to express the deepest appreciation to my supervisor Professor Paul Voyles, who continually conveyed a spirit of adventure in regard to research and scholarship, and an excitement in regard to teaching. Without his supervision, constant help and greatest patience, my research and this dissertation would not have been possible.

I would like to thank my committee members, Professor John Perepezko, Professor Paul Evans, from Materials Science and Engineering Department and Professor Mark Rzchowski from Physics Department and Professor Huifang Xu from Geology Department. Their research and attitude on materials science inspired me continuously.

I would like to thank Prof. Austin Chang and Dr. Hua Xiang in Materials Science and Engineering Department for their collaborations and help on part of my research project. I would like to thank Prof. Yamamoto and Dr. Hongxi Liu in Hokkaido University in Japan for their collaboration.

In addition, many thanks to our group members, Alex Kvit, Ye Zhu, Yi Feng, Jinwoo Huang, Li He, Andrew Yankovich, Dylan Schweiss and Pei Zhang. Without your help and support, I cannot finish my degree. I also want to thank to DOE and C-SPIN center for their financial support.

At last, I would like to thank all my friends and family for their love and support during my entire Ph.D.

Table of Contents

Abstract i

Acknowledgement iii

Chapter 1 Magnetic Tunnel Junctions 1

1.1 Magnetic Tunnel Junctions 1

1.2 Interface Dependence 5

1.3 Temperature Dependence 6

1.4 Bias Voltage Dependence 8

1.5 Ferromagnetic materials with high spin polarization 9

1.5.1 Fe_3O_4 9
1.5.2 Fe_4N 11
1.5.3 Co_2MnSi 12
1.6 Coherent Tunneling in MTJs with MgO (001) Tunnel Barrier 15

Chapter 2 Experimental Techniques 17

2.1 TEM/STEM Sample Preparation Techniques for Cross-Section Samples 17

2.1.1 Tripod Polishing 17
2.1.2 Ion milling 20
2.2 Conventional Transmission Electron Microscopy 21

2.2.1 Basics of Conventional Transmission Electron Microscopy 21
3.1.2 Two-beam Dark Field TEM for Imaging Defects 23
2.3 Scanning Transmission Electron Microscopy 26

2.3.1 Basics of Scanning Transmission Electron Microscopy 26
2.3.2 STEM Image Simulation by Frozen Phonon Multislice Algorithm 31
2.3.3 Thickness Measurement by Position Averaged Convergence Beam Diffraction 33
2.4 Cs Corrected STEM Electron Energy Loss Spectroscopy 35

2.4.1 Basics of Electron Energy Loss Spectroscopy 35
2.4.2 EELS Spectrum Imaging and Data Processing 39
2.5 Experimental Conditions for STEM Imaging and STEM EELS 41

Chapter 3 High quality ferromagnetic electrodes with high spin polarization 43

3.1 Optimization of Fe_3O_4 Thin Films on Buffered Si Substrate 43

3.1.1 Fe_3O_4 Thin Films Grown on TiN buffered Si by Reactive Sputtering 43
3.1.2 Fe_3O_4 Thin Films Grown by CO_2/CO Selective Oxidation on a Ag (TiN) Buffered Si Substrate 46

3.2 Fe_4N and $(Co_xFe_{1-x})_4N$ Thin Film Grown by Reactive Sputtering on a TiN Buffered Si Substrate..54

3.2.1 Fe_4N Thin film on TiN Buffered Si Substrate 54
3.2.2 $(Co_xFe_{1-x})_4N$ Thin Film on TiN Buffered Si Substrate 57

Chapter 4 Ferromagnet/Oxide Interfaces in Magnetic Tunnel Junctions with AlO_x Tunnel Barriers 62

4.1 Formation of Fe_3O_4 at CoFe/AlO_x Interfaces in a Nominally Symmetric Ag Buffered MTJ ..62

4.2 Fe_3O_4 Reaction Layer at Fe_4N/AlO_x Interface in a Fe_4N/AlO_x/Fe MTJ 76

Chapter 5 Ferromagnet/Oxide Interfaces in Co_2MnSi/MgO Magnetic Tunnel Junctions.. 83

5.1 MTJ Structure and Fabrications 84

5.2 Determination of MnMn/O Interface Termination 84

5.3 Channeling Effect on EELS Quantification of CMS 100

Chapter 6 O K edge ELNES of Fe oxides investigated by STEM EELS............................ 104

Chapter 7 References.. 112

Chapter 1 Magnetic Tunnel Junctions

1.1 Magnetic Tunnel Junctions

Magnetic tunnel junctions (MTJs) consist of two ferromagnetic (FM) electrodes separated by an insulating tunnel barrier as shown in **Figure 1.1 (a) and (b)**. The ferromagnetic materials used as FM electrodes are usually transition metals or metal alloys such as Fe or CoFe. The tunnel barrier is usually made from ultrathin films of materials such as AlO_x or MgO. The barrier must be so thin (a few nm or less) that electrons can tunnel through it under an applied bias voltage.[1]

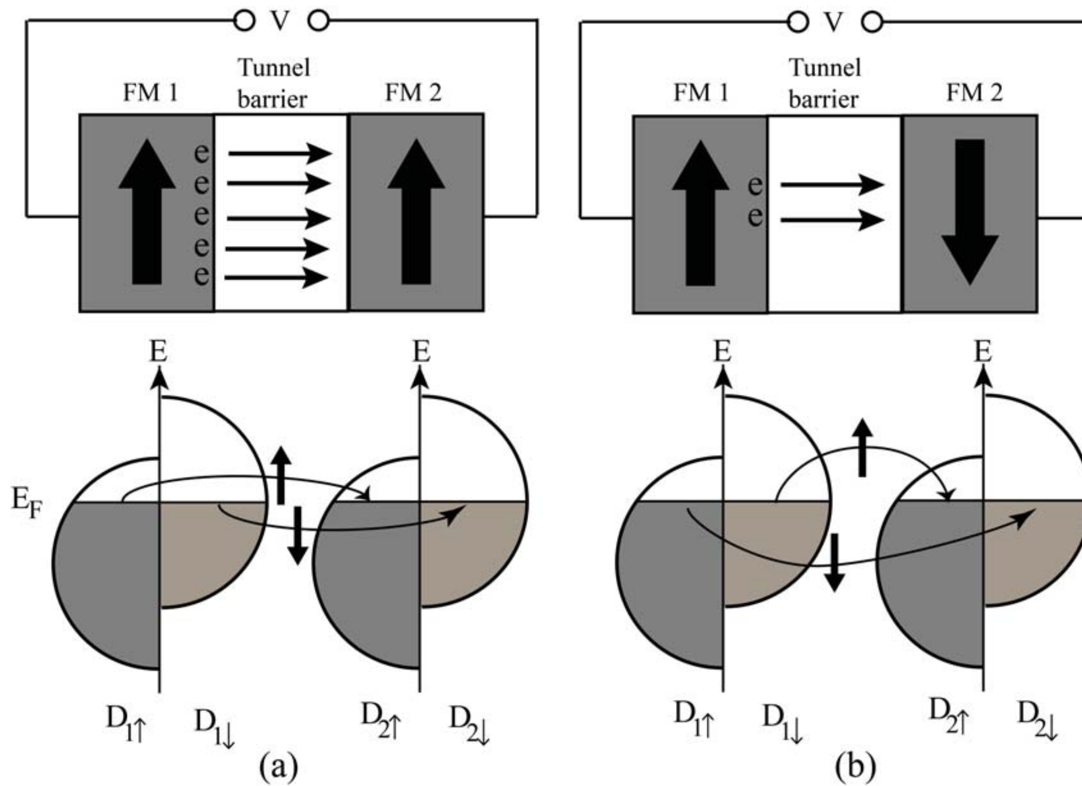

Figure 1.1 Schematics of the TMR effect in a MTJ. (a) Magnetizations in the two FM electrodes are aligned parallel. (b) Magnetizations are aligned antiparallel. $D_{1\uparrow}$ and $D_{1\downarrow}$ are the density of states at E_F for the majority-spin and minority-spin bands in FM electrode 1, respectively. $D_{2\uparrow}$ and $D_{2\downarrow}$ are the density of states at E_F for the majority-spin and minority-spin bands in FM electrode 2, respectively.

The tunneling current can be changed by changing the relative magnetization directions of the two ferromagnetic electrodes, and this phenomenon is called tunneling magnetoresistance (TMR) as shown in the top two panels in **Figure 1.1**. If the magnetizations of the two FM electrodes are parallel, the tunneling resistance is small, but if the magnetizations of the two FM electrodes are anti-parallel, the tunneling resistance is larger. This "two states" property makes MTJs suitable for memory devices in computers. TMR is the consequence of spin dependent tunneling (SDT) due to the imbalance between the electron current carried by spin-up and spin-down electrons from the two FM electrodes tunneling through the thin tunnel barrier.[1] An early model for TMR was proposed by Jullière in 1975,[2] in which TMR depends on the spin polarization of the FM electrodes as shown in Equation (1).

$$TMR= \frac{2P_1P_2}{1\text{-}P_1P_2} \quad (1.1),$$

where P_1 and P_2 are the spin polarization of the FM electrodes at Fermi level. P is defined as

$$P_\alpha \equiv \frac{D_{\alpha\uparrow}(E_F)- D_{\alpha\downarrow}(E_F)}{D_{\alpha\uparrow}(E_F)+ D_{\alpha\downarrow}(E_F)};\ \alpha = 1, 2 \quad (1.2),$$

in which $D_{\alpha\uparrow}(E_F)$ and $D_{\alpha\downarrow}(E_F)$ are the densities of states (DOS) of the electrode at the Fermi energy (E_F) for the majority-spin and minority-spin bands respectively.[1] If P_1 and P_2 are both positive, positive or normal TMR is expected.

Jullière's model can explain some of the experimental results, such as in CoFe/AlO_x/CoFe MTJs,[3] in which, TMR was 67% - 74%, consistent with the value predicted by Jullière's model 69%. However, in a $La_{2/3}Sr_{1/3}MnO_3$ (001) (LSMO)/$SrTiO_3$/LSMO MTJ, [4,5] the TMR value was 1800%, much higher than 360% predicted by Jullière's model. Stearn[6] proposed that different electronic states of electrons in FM electrodes have different tunneling probabilities, but, that model still only considered the effect of the FM electrode on SDT.

Slonczewski[7] assumed that two identical FM electrodes were separated by tunnel barrier with a square potential. After solving the Schrödinger equation, he found that the conductance (G) has a linear relationship with the cosΘ, in which Θ is the angle of magnetization between two FM electrodes as shown in **Equation (1.3)**.

$$G(\Theta) = G_0 (1 + P^2 \cos\Theta) \qquad (1.3).$$

P is the effective spin polarization, which contains a factor related to the barrier height. Equation (1.3) shows that TMR not only depends on the FM electrode itself, but also related to the tunnel barrier and interfaces of FM/barrier.

Magnetic tunnel junctions (MTJs) are widely used in nonvolatile magnetic random access memory (MRAM), read head sensors for hard discs and large arrays of sensors for imaging and ultralow field sensors.[8,9] The development of spintronic devices has been benefiting from the evolving of the novel materials and development of fundamental solid state physics.[10] However, there are still problems that prevent us to fully commercialize the spintronic devices: for example, when spintronic devices become very small, the stability of the devices is getting worse due to the thermal fluctuation. The stability issue is the main reason why we strive for a high TMR for the junctions.

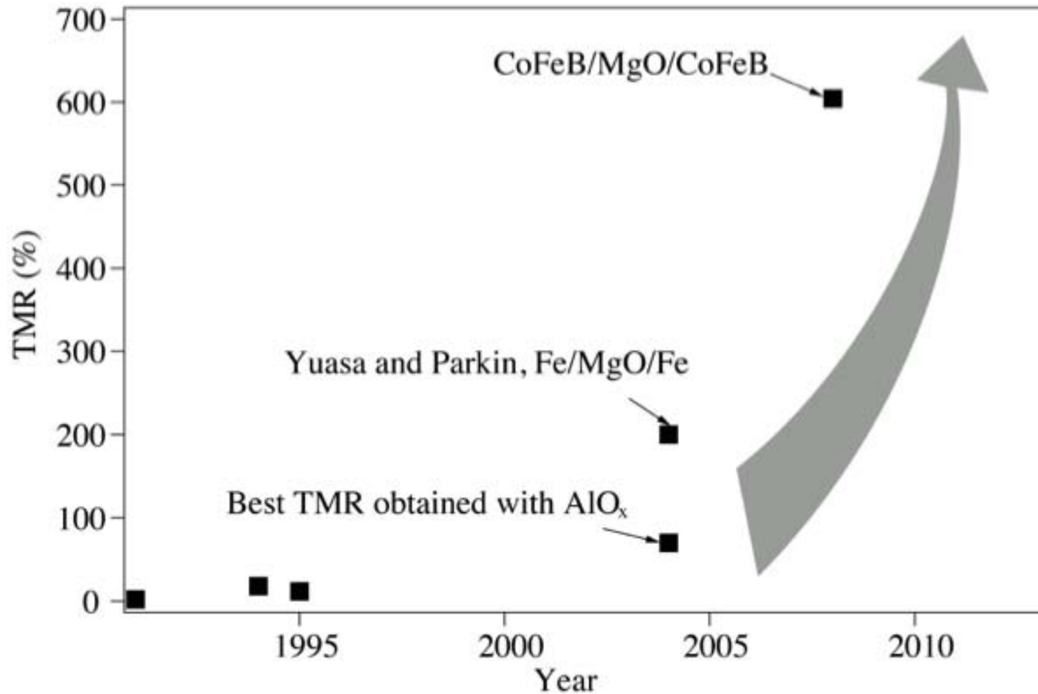

Figure 1.2 History of room temperature TMR of magnetic tunnel junctions. Refs: 11, 12, 13, 14, 15, 16, 19

Jullière's discovery of 14% TMR in his Fe/Ge-O/Fe at 4.2 K did not attract too much attention at the time. Then two decades later, in 1995, Miyazaki *et al.*[11] found 18% TMR in a Fe/AlO_x/Fe tunnel junction and Moodera *et al.*[12] found 11.8% TMR in junctions with electrodes of CoFe and Co. The highest TMR at room temperature observed to date with aluminum oxide insulators is ~70% [13,14] as shown in **Figure 1.2**. There was a huge boost of TMR (>200% at RT) in Fe/MgO/Fe junctions in 2004 obtained almost the same time by Yuasa and Parkin[15,16] because of coherent tunneling predicted in the junctions with the crystalline MgO (001) tunnel barrier.[17,18] In 2008, Ikeda *et al.*[19] obtained 604% TMR at room temperature in a fully optimized junction with CoFeB alloy as the ferromagnetic electrode contacting the MgO (001) tunnel barrier.

Figure 1.2 shows the TMR of MTJs increases with the development of new materials (e.g. CoFeB[19]) and solid-state physics (coherent tunneling theory[20]). In order to get high TMR in

MTJs, the idea seems simple: high crystal quality, defectless ferromagnetic electrodes and uniform tunnel barrier.[21] However, when we integrate those high quality essential elements into a real device (e.g. MTJs), non-perfect behaviors are observed. Why the device performance is not perfect? We use electron microscopy to answer this question and finally we hope to find the answer to the question: how we can optimize the performance of the MTJs.

This thesis is organized as following: Chapter 1 and Chapter 2 serve as an introduction to magnetic tunnel junctions and experimental techniques, respectively. Chapter 3 presents the results on the growth mechanism and crystal quality of the Fe_3O_4,[22,23] Fe_4N[24] and $(CoFe)_4N$[25] thin films. Chapter 4 presents the results of FM/oxide interfaces in MTJs with AlO_x tunnel barrier including CoFe/AlO_x interfaces[26] and Fe_4N/AlO_x interfaces. Chapter 5 presents the determination of interface termination in a Co_2MnSi/MgO based MTJ with MgO as the tunnel barrier. Finally, Chapter 6 presents the systematic study on O K edge of Fe oxides to demonstrate the differences between Fe_3O_4 and Fe_2O_3 by STEM EELS.

1.2 Interface Dependence

Experimental evidence shows that if we improved the structural quality and the ferromagnet/tunnel barrier interfaces, the TMR increases.[27] This is inconsistent with Jullière's theory. **Equation (1.1)** exhibits inverse TMR if P_1 and P_2 have different signs. However, Co/AlO_x shows positive spin polarization, although Co has intrinsic negative spin polarization.[28,29] In contrary, Co/STO does give negative spin polarization, which means that besides FM electrodes, TMR depends on the tunnel barrier and the FM/tunnel barrier interfaces as well.[30] Tsymbal *et al*.[31] showed that bonding between transition metals and the tunnel barrier can greatly affect the tunneling properties across the junctions. When s-like electrons dominate tunneling, the TMR is positive. When d-like electrons dominate, the TMR is negative.

In a NiFe/Ta_2O_5/AlO_x/NiFe double-barrier MTJ,[31,32] the tunneling process at the NiFe/Ta_2O_5 interface is dominated by d-electrons, but tunneling at the AlO_x / NiFe interface is dominated by s-electrons. The spin polarizations are opposite for s- and d- electrons, which causes the negative TMR. Itoh and Inoue[33] calculated the electronic states of transition metal / Al_2O_3 interfaces, and they found that imperfect metal / tunnel barrier interface can result in a sign reversal of the SP due to the presence of imperfectly oxidized Al at the interfaces. Tsymbal *el al.*[34] also found SP of and an Fe surface in contact with vacuum switches from positive to negative when the Fe is oxidized.

Defects and disorder present in the FM electrodes and FM/tunnel barrier interfaces also affect the interfacial electronic states that contribute to tunneling. The tunneling electrons will scatter at defects, leading to coupling of bulk and interface states, which will affect the SP across the interfaces. For example, the sign of the TMR can be affected by the impurities like carbon at the interfaces, because of electrons scattered by the impurities like carbon enhancing d-like electrons tunneling, leading to inverse TMR.[35] LeClair *et al.* demonstrated in experiments that the coupling of bulk and interfacial electronic states controls the tunneling properties in the Co/AlO_x/Co junction with both Cu[36] and Ru[37] inserted in between Co and AlO_x.

All this theoretical and experimental evidence show that SDT is not just an intrinsic property of the ferromagnetic electrodes but depends on the entire junction structures and electronic properties including the insulating tunnel barrier and the ferromagnet/insulator interfaces.

1.3 Temperature Dependence

TMR decreases when increasing temperature. Early phenomenological model proposed by Shang *et al.*[38] shows that the spin polarization P decreases with increasing temperature due to

the spin wave excitations. The relationship between spin polarization P and temperature T can be described by P (T) = P (0)(1 − α$T^{3/2}$), where P (0) is the spin polarization at T = 0 K. However, this model still only considers the contribution from the FM electrode. Another model involves spin flip scattering by magnetic impurities in the barrier by Vedyayev *et al*.[33] They proposed that the number of electrons contributing to spin flip scattering increases with increasing temperature, which results in the drop of TMR. However, still, these models do not take into account of the ferromagnet/tunnel barrier interfaces.

The FM/tunnel barrier interface can also affect the temperature dependence of MTJs. If electrons tunneling from the majority-spin band to the minority-spin interface states interact with thermally excited magnons at finite temperature, spin-flip scattering occurs, leading to increasing tunneling conductance for the anti-parallel magnetization configuration and decreasing TMR ratio at finite temperatures.[39] For example, in a MTJ with Co_2MnSi (CMS)/MgO interfaces, Mavropoulos *et al.*[39] showed that the critical role of interface states of half metallic electrodes/tunnel barrier for spin-dependent tunneling in half-metal-based MTJs. Ishikawa *et al.*[40] provided strong experimental evidences of the strong temperature dependence of TMR on the interfacial states of minority spin at E_F in a CMS/MgO/CMS MTJs. They discovered a possible process that can lead to the non-symmetric behavior of conductance under applied bias voltage, which is the evidence of minority state existing at E_F. The tunneling scenario is that the electrons tunnel to the interfacial states and are spin flipped by the magnons excited by the fast electrons.

The size of this interface-based effect varies with the materials system. Yamamoto *et al.(personal communication)* used γ to characterize the size of the temperature dependence. γ is defined as the ratio between TMR at 4.2 K and TMR at room temperature. In a CoFe/MgO/CMS

MTJ, TMR at RT is 335%, but TMR at 4.2 K is 1024%.[41] γ is 3.06 for this CMS/MgO based junction. But in a CoFe/MgO/CoFe MTJ, γ is 1.36.[42] In a similar system, CoFeB/MgO/CoFeB MTJ, γ is 1.89 with TMR 604% at RT and 1144% at 5 K.[19] These examples indicate that the spin polarization of the CMS/MgO interface exhibits stronger temperature, which is due to the soft spin stiffness of Co terminated CMS/MgO interfaces predicted by spin resolved LDOS.[43] Therefore, to understand the temperature dependence of the MTJs, fully characterization of FM/tunnel barrier interface is the critical.

1.4 Bias Voltage Dependence

TMR decreases when increasing applied bias voltage. Bias voltage dependence depends on both FM/barrier interfaces and FM electrodes. One explanation proposed by Zhang *et al*.[44] suggested that the dropping of TMR can be attributed to the spin-flip process by the exciting magnons at the interface of FM electrode/tunnel barrier. At the zero bias, the electrons from one FM electrode travel fast and arrive at the second FM electrode without scattering much. However, when there is a bias voltage, the electrons will lose energy by emitting a magnon and thereby flipping the electron spin, which decreases the TMR. However, experiment by Wulfhekel *et al.*[45] in a Co MTJ with vacuum as the tunnel barrier contradicted Zhang's model. They observed no decreasing on TMR when increasing bias voltage. Therefore, they suggested that the dropping of TMR depends on the imperfection of the real tunnel barrier.

Electronic structures of FM electrodes can also affect the bias voltage dependence. If we apply a bias voltage to a MTJ, then the transport electrons can access a different part of the DOS. Therefore, the conductance becomes energy dependent, which leads to the variation of TMR regarding to the applied voltage. This mechanism is sensitive to the type of ferromagnet. In a Co/AlO_x/Co MTJ, LeClair *et al.* [46] found that there is a strong bias dependence of TMR on the

phases of Co by using different crystalline phases of Co. They found that if upper Co and lower Co electrodes have different phases, eg. fcc and hcp, the bias dependence showed strong non-symmetric pattern, but if both of the electrodes are polycrystalline, then the bias dependence is almost symmetric.

1.5 Ferromagnetic materials with high spin polarization

Although interfacial effects are important, high bulk spin polarization of the FM electrodes is a necessary precondition for achieving high TMR in an MTJ. Introducing negative spin polarization, a material with a higher density of states in the spin channel anti-aligned to the magnetization than the aligned channel, has the potential to introduce new device functionalities, such as three-state devices. To that end, we have explored several new materials with either measured or predicted high intrinsic spin polarization, sometimes negative, for applications in MTJs.[30,32,47]

1.5.1 Fe_3O_4

Fe_3O_4 (Magnetite) has been predicted by theoretical calculations to be a half metal with negative spin polarization (SP) at room temperature (RT).[48] The space group of Fe_3O_4 is F*d3m*. As shown in **Figure 1.3**, a close-packed face-centered-cubic structure is formed by the oxygen atoms with the smaller iron atoms occupying the interstitial positions. Fe^{3+} occupies all tetrahedral A sites and half of octahedral B sites, and Fe^{2+} sits only in the another half of the B sites, which makes Fe_3O_4 ferrimagnetic. A high negative SP of -80 ± 5% in Fe_3O_4 (111) thin films has been experimentally confirmed at RT.[49] Combined with a high Curie temperature of 860 K, Fe_3O_4 is one of the most promising magnetic materials for thin-film spintronic devices.[50,51]

However, most of the MTJs with Fe_3O_4 as electrodes did not produce inverse or high TMR,[52-54] which can be attributed to defects and the existence of other phases in the electrode or at the interfaces between electrodes and tunnel barriers.[53,55-58] For example, in Fe_3O_4, the magnetization saturates only at very large applied field due to the presence of antiferromagnetic-coupled anti-phase boundaries (APBs)[59-63]. More experimental results will be discussed in Chapter 3.

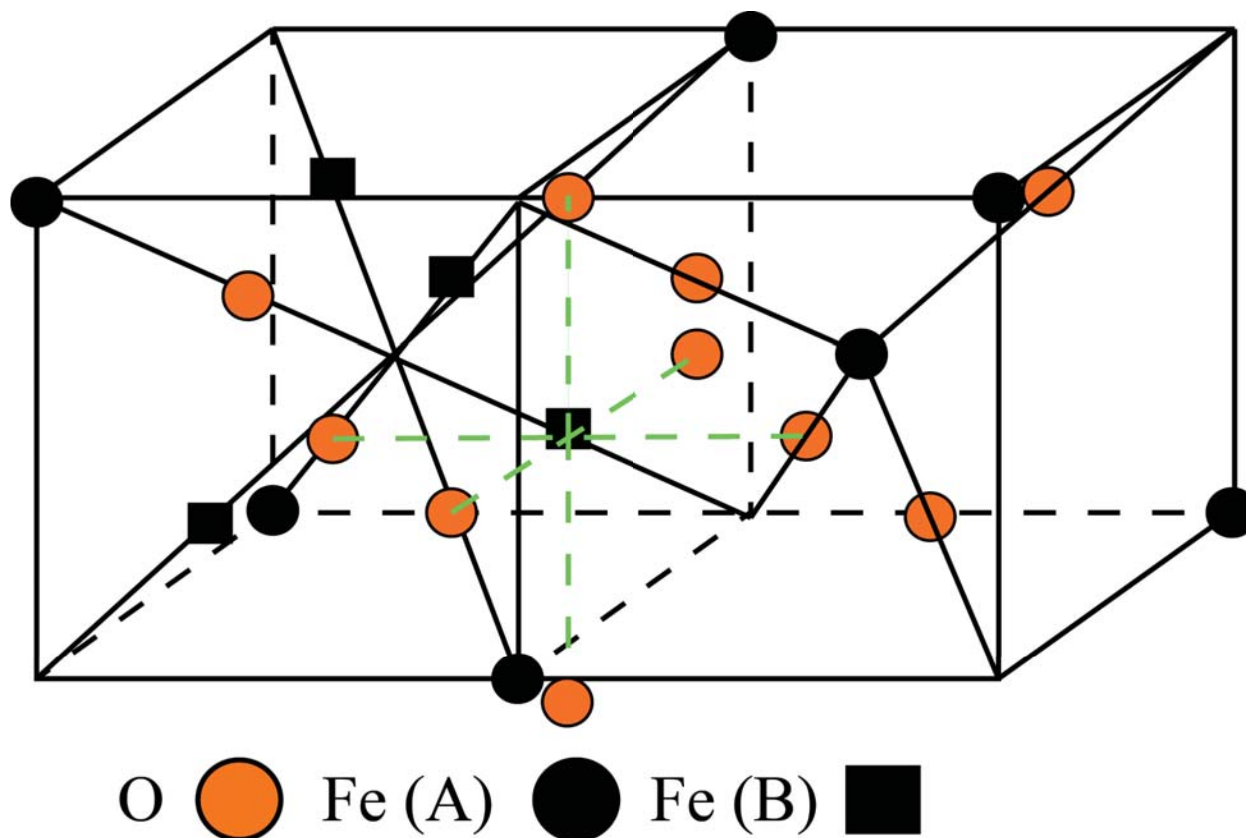

Figure 1.3 The crystal is made of alternate stacking of the two cubes which form the basis in a face-centered-cubic (fcc) lattice.

1.5.2 Fe_4N

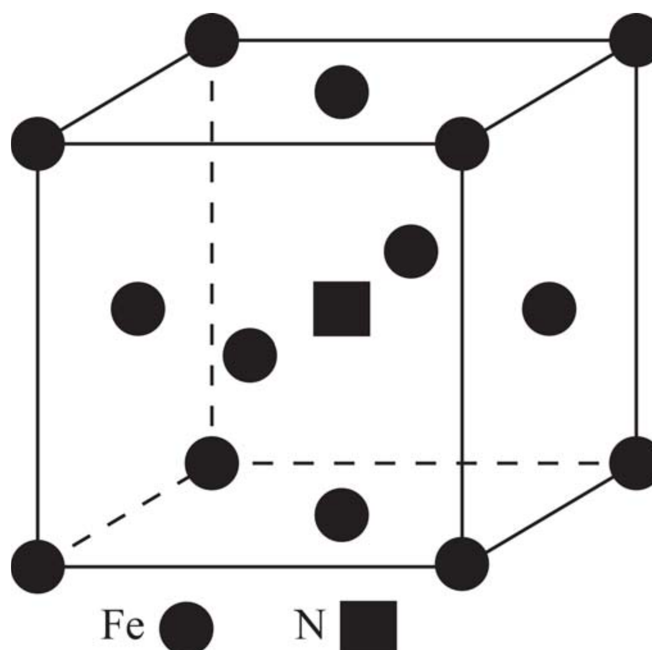

Figure 1.4 Crystal structure of Fe_4N. Fe atoms are labeled as circles and N atom is labeled as square.

Another candidate, Fe_4N also has been recently predicted theoretically for nearly perfect negative spin polarization of the conduction current.[64] The total conductivity is dominated by the Fe *3d* electrons because of the strong local interaction between Fe *4s* and N *2p* electrons.[65,66] -59% negative SP at RT has been reported for a (100)-oriented epitaxial Fe_4N film.[57,67] Combined with the high Curie temperature of 494 °C, Fe_4N is promising for spintronic devices.

The crystal structure of Fe_4N is shown in **Figure 1.4 (b)**. Fe_4N has an anti-perovskite crystal structure, where the Fe cations occupy the two nonequivalent sites, namely, the corner sites and face-centered sites, while the nitrogen sits at the body-centered positions.[68] Simpler crystal structure of Fe_4N may avoid some of the defect related problems of Fe_3O_4. Fe_4N is a metastable intermediate phase with respect to decomposition of Fe and N.[66]

Record-holding TMR in MTJs with Fe_4N electrode of -75% was achieved by Komasaki *et al.*[57] in a Fe_4N/MgO/CoFeB based MTJ. To avoid interface oxidation, an ultrathin Mg layer (0.4 nm) was inserted in between Fe_4N and MgO. However, in a similar junction without the ultrathin inserted Mg, the TMR was only -18.5%.[69] These two different results suggested that the preventing the oxidation of Fe_4N is the key for obtaining high TMR.

1.5.3 Co_2MnSi

Heusler alloy Co_2MnSi with $L2_1$ structure (space group $Fm\bar{3}m$) are predicted to have 100% spin polarization at Fermi level (E_F) at room temperature.[70] The half metallic behavior of the Heusler alloys origins from the distinguish behavior between spin up and spin down electrons: the electrons responsible for the metallic behavior share the same spin and the electrons with the opposite spin are insulating.[71,72]

As a promising materials for spintronic devices,[73,74] Heusler alloys have attracted great interest both theoretically and experimentally.[70] The Heusler $L2_1$ alloys have high Curie temperatures (*Tc*), which are important in the application of half metals at finite temperature. For example, Co_2MnSi has a Curie temperature of 985 K.[75]

Heusler alloys with $L2_1$ structure a formula of X_2YZ, in which X atoms usually are Cr, Mn, Fe, Co Ru and Rh; Y atoms are usually Ti, V, Cr, Mn and Fe; Z atoms are Al, Si, Ge, Sn and As. The structure can be described by four interpenetrating fcc lattices. The $L2_1$ crystal structure has the positions: X_1 (¼, ¼, ¼), X_2 (¾, ¾, ¾), Y (0 0 0), and Z (½, ½, ½).[70] For Heusler alloy in B2 phase, Yand Z randomly occupy each other's sites and X sites stay undisturbed. A2 phase Heusler alloy is the complete disordered phase, in which X, Y and Z atoms randomly sit on the Heusler alloy cubic lattice. It produces Bragg reflections with non-zero structure

amplitudes when the Miller indices of the scattering planes are either all odd or all even. The reflections are of 3 types with structure amplitudes given by:

(1) h, k, l, all odd

$F(1\ 1\ 1) = 4|[(f(X_1)-f(X_2))^2 + (f(Y)-f(Z))^2]^{1/2}|$

(2) (h+k+l)/2 = 2n+ 1

$F(200)= 4|f(X_1)- f(Y) +f(X_2) -f(Z)|$

(3) (h+k+l)/2 = 2n

$F(220) = 4|f(X_1)+f(X_2)+f(Y)+f(Z)|$

$f(X_1)$, $f(X_2)$, f(Y) and f(Z) are the scattering factors for the atoms on the X_1, X_2, Y and Z sites respectively. The reflections for which (h + k+ 1)/2 = 2n (group (3)) are unaffected by the state of chemical order. But the remaining two groups of reflections are superlattice reflections, which will change with respect to the chemical disorders.

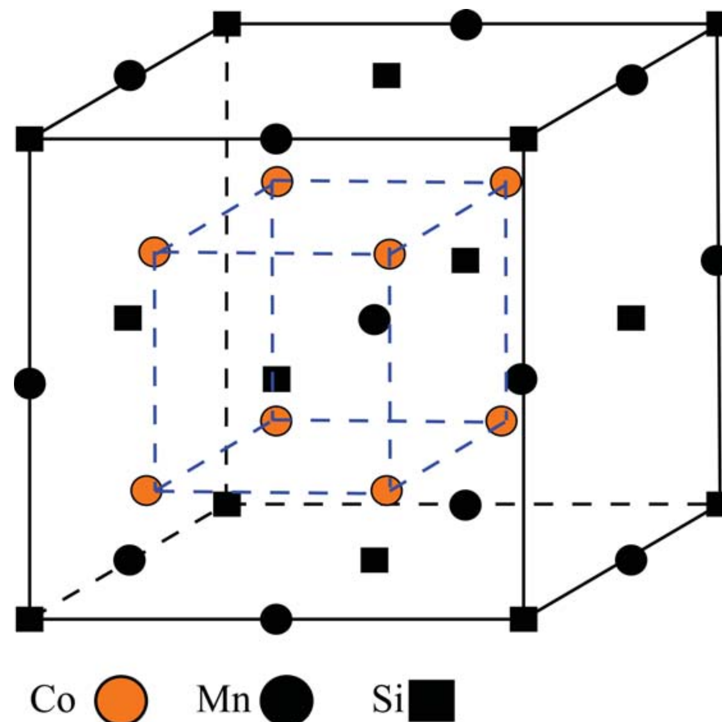

Figure 1.5 Crystal structure of Co_2MnSi in $L2_1$ phase.

Co_2MnSi (CMS) with $L2_1$ structure, which can give 100% spin polarization at Fermi level at room temperature.[71,76] As described in the last paragraph, Mn and Si occupy different site (000) and (½, ½, ½) separately for CMS in $L2_1$ phase shown in **Figure 1.5**.

Relatively low TMR in MTJs with CMS electrodes[74,77-79] suggests the presence of structural disorder in the CMS electrodes or non-perfect CMS/tunnel barrier interfaces. One possible structural disorder can be that B2 or A2 phase coexist with $L2_1$ phase in CMS, which leads to decrease in the spin polarization of the CMS. From X-ray diffraction, we can evaluate the percentage of B2 or A2 phases in CMS. For CMS, X_1=X_2=Co, Y = Mn and Z = Si. Therefor, the structure amplitudes reduce to the following:

(1) F(111) = 4|f(Mn)-f(Si)|

(2) F(200) = 4|2f(Co)-(f(Mn)+f(Si))|

(3) F(220) = 4|2f(Co) + f(Mn)+f(Si)|

As if CMS in B2 phase, since Mn and Si sites are mixed together, therefore group (1) reflection will be zero. We can obtain the relative phase ratio by the relative peak intensity of the F(111) and F(200).[80]

The second structural defect that leads to low TMR signal could be antisite defects, especially Co antisite defects, which add character across E_F and destroy the half metallic properties.[81] Antisite defects are point defects. There are four main types of point defects in CMS including Mn antisite defect (Mn_{Co}), Co antisite defect (Co_{Mn}), Co-Mn swap and Mn-Si swap as shown in **Table 1**. Although the formation energy of Mn_{Co} is lower than the other three types of defects shown in **Table 1**, Co antisites defects are predicted more detrimental to the half metallic state of CMS.[82] Therefore, controlling the antisites defects in CMS is necessary in experiments for obtaining high TMR in CMS based MTJs as shown by Yamamoto *et al*.[40]

Table 1 Formation energy (in eV) for different defect types in Co_2MnSi.[81]

Defect type	Formation energy (eV)
Co antisite	0.8
Mn antisite	0.33
Co-Mn swap	1.8
Mn-Si swap	1.33

Neutron diffraction and Extended X-Ray Absorption Fine Structure (EXAFS)[82,83] have been used to evaluate the concentration of Co antisite defect. The concentration of the Mn antisite and Co antisite defect are measured to be 14% and 5%~7% respectively.[82,83]

1.6 Coherent Tunneling in MTJs with MgO (001) Tunnel Barrier

Jullière's theory assumes that the tunneling probabilities are the same for all tunneling states, which is almost true for amorphous tunnel barrier such as AlO_x.[1] However, for crystalline MgO (001) tunnel barrier, although it has no state across E_F, simulation shows electrons with Δ_1 state has the highest DOS across the E_F still propagate through evanescent states of MgO, which will result in high tunneling probability,[16] and this phenomenon is called coherent tunneling.[84] Electron with other Bloch states such as Δ_5 and $\Delta_{2'}$ have DOS 10^{-5} order of lower, so the contributions from those states are negligible. Coherent tunneling requires that $k_{||}$ is conserved during electron tunneling.

MgO works as a "spin filter" selecting electrons with preferred Δ_1 Bloch state.[84] Majority Bloch states with Δ_1 symmetry (or other symmetries) in the Fe electrode decay as evanescent states with Δ_1 symmetry (or other symmetries) in MgO barrier. The slow decay state Δ_1 only

occurs only for majority spins, not minority spins. Thus the conductance of majority state is much higher than that of minority state. This spin filter process results in extremely high TMR even for junctions without 100% spin polarized FM electrodes. It is why high TMR is expected in the Fe/MgO/Fe junctions.[85]

Yuasa[15] and Parkin[16] independently demonstrated over 200% TMR at room temperature in a Fe/MgO/Fe MTJ, confirming that the coherent tunneling does exist at Fe / MgO (001) tunnel barrier interface as the theory predicted.[17,18] Besides Fe, Co/MgO,[86] CoFeB/MgO[87] and Co_2MnSi/MgO[88] MTJs also exhibit coherent tunneling. Compared with the similar junctions with AlO_x tunnel barrier, TMR in MTJs with MgO tunnel barrier is much higher.

Coherent tunneling is also affected by the interfacial states.[17] Zhang *et al.*[89] and Tusche *et al.*[90] predicted that an atomic layer thick FeO at the interface of Fe/MgO greatly reduces the TMR of the MTJ. Zhang *et al.*[89] also found that the interfacial FeO layer has little effect when the magnetizations of two FM electrodes are anti-parallel compared to the parallel case. However, experimentally, Zermatten *et al.*[91] found that the conductance has been reduced by the interface FeO layer for both anti-parallel and parallel-aligned case. Tusche *et al.*[90] also suggested that the structural symmetry and coherency are more important to achieve high TMR. Their calculation shows that a junction with FeO layers inserted in between both side of the interfaces shows much higher TMR than the one with FeO inserted on only one side of interface. The perfect interface is also easily destroyed by the interface roughness related disorder. Perfect coherent tunneling is hard to achieve, therefore, the experimental TMR[16,19,92] is still substantially lower than the theoretical predicted values.[17]

Chapter 2 Experimental Techniques

2.1 TEM/STEM Sample Preparation Techniques for Cross-Section Samples

2.1.1 Tripod Polishing

The cross-section TEM/STEM sample preparation technique mainly follows the procedures developed by Voyles *et al.*[93] First, we prepared a "sandwich" of samples by gluing two pieces of samples together with the thin films side facing each other. Then we polished the sample by tripod polishing. The final thinning step was to remove the polishing damages and further thin the specimen by low-angle ion milling.

Since the polishing recipe for Si is well developed, the detailed recipe for a sample with MgO substrate is presented here as an example to demonstrate the polishing procedure step by step. The differences between Si and MgO are as follows. (1) MgO is transparent, but Si is not. For Si, when it is thinner than 50 nm, it is red color on the thin edge, and when the sample is viewed under an optical microscope, the Si becomes transparent. However, since MgO is always transparent, it is difficult to tell the thickness. (2) MgO is harder than Si and much easier to crack when it gets thin, so it is difficult to polish MgO to final thickness by pure tripod polishing. (3) MgO reacts with water, which means during polishing, we cannot use water to wash off the polished dust, and polishing with oil is not as efficient as polishing with water. The sample surface is also easily scratched by the unwiped MgO dust. The solution I have used is first to use water for polishing instead of oil, and then to use the Allied High Tech Inc. "blue lube", which is an alcohol-based diamond suspension, for the final finishing step to remove the reacted surface layer. Finally, I further thinned the sample and removed the damaged layer by ion milling.

(1) Making the "sandwich"

First, I cut two small pieces (2 mm×1.5 mm) along the desired direction (for MgO, along [100] and [010] are the easy cleavage directions) and glued them together with the thin film sides facing each other using Allied High Tech epoxy 110. The epoxy contains two parts: one part is resin (part A), and the other is adhesive (part B). To maintain good viscosity and a thin glue line, the ratio between part A and part B should be 10:1. The glued sandwich was cured on the hot plate at 100 °C~150 °C for 5~10 min. The color of the cured epoxy was dark brown but transparent. The procedure is shown in **Figure 2.1.1**.

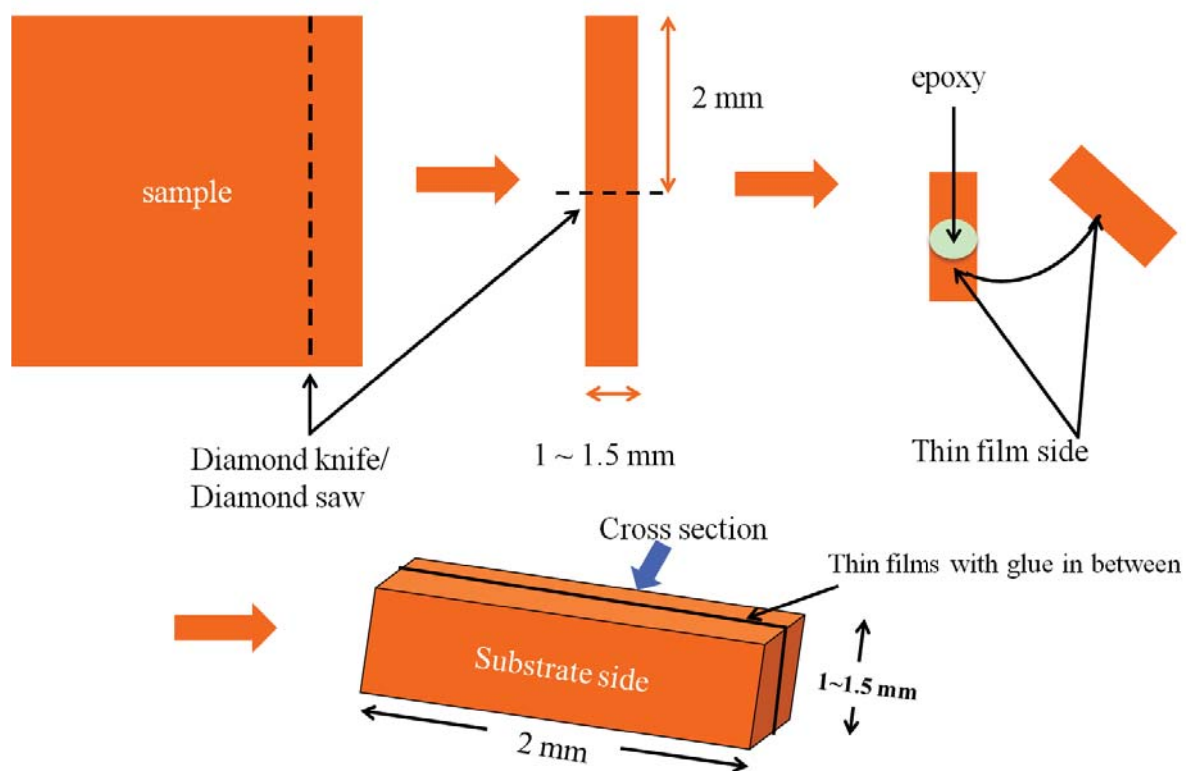

Figure 2.1.1 A schematic of the cuts necessary to make a "sandwich" for a TEM cross-section sample.

(2) First side polishing

We first glued the sandwich to an Allied aluminum-polishing stub using Crystal Bond. We then measured the thickness of the sample using a digital micrometer. Before we mount the sample on the stub, the ideal thickness of the sample is 0.8 mm ~ 1 mm to minimize the

polishing time. If the sample is thicker than 1 mm, we can polish with 30-μm diamond lapping film from Allied High Tech Inc. to thin the sample to 1 mm. The recipe for the first side polishing consists of the following steps:

1. Polish the sample to 700 μm with 15 μm lapping film at 100 rpm and sample load 0.04 g (No. "4" labeled on the polishing wheel);
2. Polish the sample to 650 μm with 6 μm lapping film at 75 rpm and sample load 0.03 g (No. "3" labeled on the polishing wheel);
3. Polish the sample to 600 μm with 3 μm lapping film at 50 rpm and sample load 0.02 g (No. "2" labeled on the polisher wheel);
4. Polish the sample to 590 μm with 1 μm lapping film at 50 rpm and sample load 0.01 g (No. "1" labeled on the polishing wheel);
5. Polish the sample until the surface is free of scratches with 0.1 μm lapping film at 30 rpm with green lube and sample load nearly 0 (No. "0" labeled on the polishing wheel).

As we polished, we cleaned up the polished MgO dust by holding a folded piece of paper on the diamond lapping film to minimize the scratches on the sample surface. After the first side was polished, we put the sample with the stub on the heating plate to make the Crystal Bond soft. We then picked the sample up with tweezers and mounted the sample on the transparent stage using LOCTITE 460 (super glue) with the polished surface facing down. We waited at least 2 hours until the super glue completely dried beneath the specimen, and then started the second side polishing.

(3) Second side polishing

Before we polished the second side, we needed to set the polishing angle to 2°, which corresponds to two and half clockwise rotations of the screw for the tripod plane. The recipe for the second side polishing is shown below:

1. Polish the sample to 250 μm with 15 μm lapping film at 100 rpm and sample load 0.04 g;
2. Polish the sample to 150 μm with 6 μm lapping film at 75 rpm and sample load 0.03 g;
3. Polish the sample to 60 μm with 3 μm lapping film at 50 rpm and sample load 0.02 g;
4. Polish the sample with 1 μm lapping film at 50 rpm and sample load 0.01 g until the edge of the glass polishing mount is polished as well as the sample. This criteria ensures that at least we have a reasonable thin sample. The thin part will crack off, even with just a little force on it, so, slow polishing with small force are essential to obtain a good TEM sample at this step;
5. Polish the sample with 0.1 μm lapping film at 30 rpm with blue lube and sample load nearly 0 until no scratches.

We used acetone to wash off the sample from the transparent stage. At the same time, we cleaned the Mo sample ring using cleanser 409 to remove the mechanical oil left on the Mo ring. We then put M-bond glue on the Mo ring and picked up the polished specimen. We left it to dry for at least 1 hr. Then we heated up the sample at 120 °C for 1 hr to make the M-bond conductive. Finally, we used the ion mill to remove the polishing artifact and further thinned the sample.

2.1.2 Ion milling

Ion milling is used after the tripod polishing to remove polishing damages, additional scratches and contaminations on the surface. The ion milling machine I used is the Fischione 1010.

For samples with MgO substrates, we first used ion beam energy 5 kV and 5 mA beam current for 1 hr, followed by 4 kV and 5 mA for 1.5 hr. Finally, we used beam energy 1.5 kV and 5 mA beam current for 15 min to remove the ion milling damages on the specimen. The milling angle was 8°.

For samples with Si substrates, we first used ion beam energy 4 kV and 5 mA beam current for 1 hr, and then we used beam energy 1.5 kV and 5 mA current for 15 min to remove the damage on the surface of specimen. The milling angle was 8° ~ 9°.

Liquid nitrogen cooling was used to reduce the redepositions of soft metals such as Ag and Au. Before being investigated under a microscope, the samples were plasma-cleaned to avoid contamination for 10 min for MgO or 3 min for Si with 25% O_2+Argon (balanced) at 22 psi with a Fischione plasma cleaner model 9020.

2.2 Conventional Transmission Electron Microscopy

2.2.1 Basics of Conventional Transmission Electron Microscopy

Conventional transmission electron microscopy (CTEM) is widely used in characterizations of microstructures and microanalysis of materials, especially the multilayer thin films.[94]

In a typical TEM, there are five main subsystems, the electron gun, the illumination stage, the objective lens, the magnification and projection system and the detector system. The purpose of the electron gun and illumination stage is to create an electron beam in a well-defined reference state. The electron beam coherence can be used as a measurement of how well the electron beam is formed. The temporal coherence length represents the energy spread of the electron beam: the smaller the energy spread, the bigger the temporal coherent length. All

electrons emitted from the gun reach to a cross over formed by the electron-magnetic lenses. To form a useful imaging source, condenser lenses and apertures are used below the cross over. Spatial coherence is defined to characterize the interference of the electrons passing through the apertures. The spatial coherence improves at a cost of the beam current when the condenser aperture gets smaller. Therefore, a compromise has to be made between the spatial coherence and the beam current.

The objective lens (OL) is used to form the primary image and diffraction pattern from the sample. The OL is the strongest lens in the microscope. The diffraction pattern sits in the back focal plane of the OL, and the image is in the selected area plane. The projection system uses multiple lenses magnify the image or diffraction pattern onto the detectors. We have used a range of detectors including the viewing screen, imaging plates and charge-coupled device (CCD) cameras.[95]

High resolution TEM (HRTEM) is useful for imaging the multilayer thin films like MTJs. In **Figure 2.2.1**, a typical HRTEM image of a MTJ sample, the layered structure CoFe/AlO_x/CoFe, is shown. For example, the tunnel barrier AlO_x can be identified since it is brightest due to its amorphous structure and low atomic number. We can also resolve the interface roughness between CoFe and AlO_x tunnel barrier using this technique.

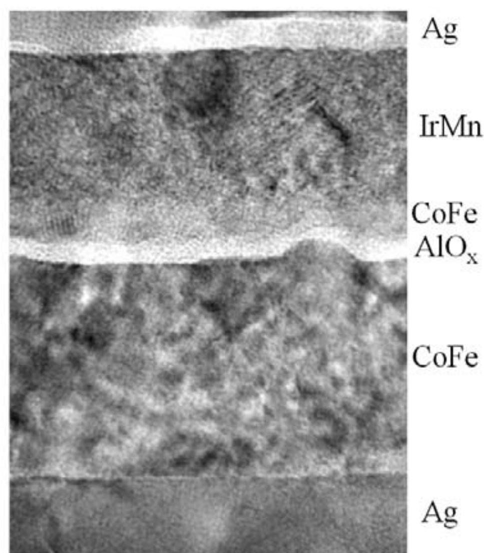

Figure 2.2.1 A typical TEM image of a magnetic tunnel junction consisting of multilayer thin films.

HRTEM can extract structure information at the atomic scale. The electron beam goes through a sample in which Bragg diffraction happens from different crystal planes, and the contrast arises from the interference between diffracted beams with the transmitted beam.[95] The contrast mechanism of HRTEM images is phase contrast, which can be used to retrieve structure information.[94] For HRTEM, an objective aperture is needed to capture beams with different reciprocal space vector **g**. Each **g** vector corresponds to one set of lattice fringes in the HRTEM images. How many sets of planes one can see in the image depends on the parameters of the microscope, such as the spatial resolution and the size of the objective aperture. Since complicated phase information is contained in the images, TEM image simulation with regard to sample thickness and defocus is necessary to correctly interpret the structure.[95]

3.1.2 Two-beam Dark Field TEM for Imaging Defects

Imaging defects such as dislocations, grain boundaries, or stacking faults is another important application of CTEM, especially a two-beam condition TEM.[96] The mechanism of the

defect imaging is well understood. Unlike a perfect crystal, the crystallographic symmetry is broken around the defects, which means that the periodic crystal field is disturbed at the defects. When the translational symmetry of a crystal is broken, atoms are displaced with a displacement vector **R** with respect to the perfect Bravais lattice translation vectors **r**. Denoting the potential in a perfect crystal as **V**(**r**), the disturbed crystal potential at the defects can be expressed as **V**(**r** + **R**). **V**(**r** + **R**) is a local quantity, affecting only the point at which a defect exists. The Darwin-Howie-Whelan (DHW) equations for the perfect crystal[95] need to be modified for the defect case. As shown in Equation (2.1), compared to the DHW equation for the perfect crystal, the only difference is the replacement of s_g with $s_g + g \cdot \frac{dR}{dz}$.

$$\frac{d\phi_g}{dz} - 2\pi i(s_g + g \cdot \frac{d\boldsymbol{R}}{dz})\phi_g = i\pi \sum_{g'} \frac{e^{i\theta_{g-g'}}}{q_{g-g'}} \phi_{g'} \tag{2.1}$$

$$s_g + g \cdot \frac{d\boldsymbol{R}}{dz} = s_g + \frac{d(\boldsymbol{g}\cdot\boldsymbol{R})}{dz} \tag{2.2}$$

Here $\boldsymbol{s_g}$ is the excitation error. $|s_g|$ is the distance in reciprocal space between the Ewald sphere and the end point of vector **g**. The direction of s_g describes the orientation of the planes with wavevector **g** with respect to the Ewald sphere. $s_g + g \cdot \frac{d\boldsymbol{R}}{dz}$ is then the effective position-dependent excitation error. The derivative $\frac{d(\boldsymbol{g}\cdot\boldsymbol{R})}{dz}$ is taken parallel to the electron beam direction, as shown in Equation (2.2). As a result, the displacement vector **R** can only be probed for a particular two-beam condition if $\boldsymbol{g} \cdot \boldsymbol{R}$ changes with respect to the beam direction. Only the variation of **R** along the depth direction can be detected. $\boldsymbol{g} \cdot \boldsymbol{R}$ is also known as the criterion for visibility of the defects.

A proper experimental setup is necessary to detect the defects based on the criterion of $\boldsymbol{g} \cdot \boldsymbol{R}$. Orienting the specimen to a two-beam condition allows the operator to select the proper diffracted beams, which enhance or weaken the contrast of certain defects. The steps required to

set up the correct two-beam condition in the CTEM are as follows. (1) Identify the displacement vector **R** prior to the CTEM experiment, and choose an appropriate **g**. (2) Create a **g**-3**g** diffraction condition by tilting the sample so that $\mathbf{s_g}$ is strongly excited while $\mathbf{s_{3g}}$ is equal to zero. Experimentally, we first tilt the sample to a proper zone axis, which contain pairs of **g** vectors suitable for defect imaging. Then we tilted the sample to make one **g** vector more excited than the other paired **g** vector. Third, we switched the image mode to dark field mode, which allows us to tilt the electron beam. Finally, we tilted the weak **g** vector back to optical axis and made it strongly excited. The objective lens aperture needs to be inserted to select the **g** vector at the optical axis.[97]

Planar defects with discontinuous displacement vector **R**, for example APBs in Fe_3O_4,[95] can be imaged in a two-beam TEM image. The displacement vector **R** across the APBs is a translational vector of the disordered crystal structure, but not of a translational vector of the crystal. The APBs can be either planar or curved. If the APBs are isotropic, then the fault will be curved because there are no favored planes for the APBs. On the other hand, if the APBs are anisotropic, then the APBs will be formed at specific planes. For example, in Fe_3O_4, the displacement vector **R** is along 1/4a<110>. Imaging an APB requires selecting the proper **g** vector that satisfies the **g**-3**g** condition for the two-beam condition of the CTEM. The discovery of low defect density Fe_3O_4 thin film using images of APBs will be discussed in Chapter 3.

Qualitative understanding of CTEM images of defects based on the DHW formalism is straightforward. It enables characterization of defect crystallography and density. Detailed understanding of all the contrast features in a CTEM image, while often not needed, requires image simulations.

2.3 Scanning Transmission Electron Microscopy

2.3.1 Basics of Scanning Transmission Electron Microscopy

In scanning transmission electron microscopy (STEM), we usually use high angle annular dark field (HAADF) detector to detect the elastically scattered electrons. The contrast mechanism in HAADF STEM is incoherent imaging. The detector angle of HAADF detector is sufficient large to allow the strong, Bragg diffracted beams to pass through the hole in the detector undetected, leaving only the thermal diffuse scattering from phonons, and some higher order Laue zone scattering. The phases of the scattered electrons are also averaged out in the HAADF mode. As a result, the intensity *I* in STEM is approximately proportional to $Z^{1.7}$ where Z is the atomic number. The images taken using HAADF detector are called Z-contrast images. In comparison with CTEM, *Z*-contrast STEM combines high resolution with a faithful representation of the object, thanks to due to the incoherent nature of the imaging.[98,99] STEM can also be used to image interface ordering[100] and defects in semiconductors[101]. **Figure 2.3.1** shows a typical HRSTEM image of a MTJ with a Co_2MnSi (CMS) top electrode, an MgO tunnel barrier and a CoFe bottom electrode, in which we can easily identify all the layers based on their intensity. At CMS/MgO interface, although significant interfacial strain exists due to the large lattice mismatch between these two materials, the contrast remains interpretable and steps of MgO are also clearly resolved.

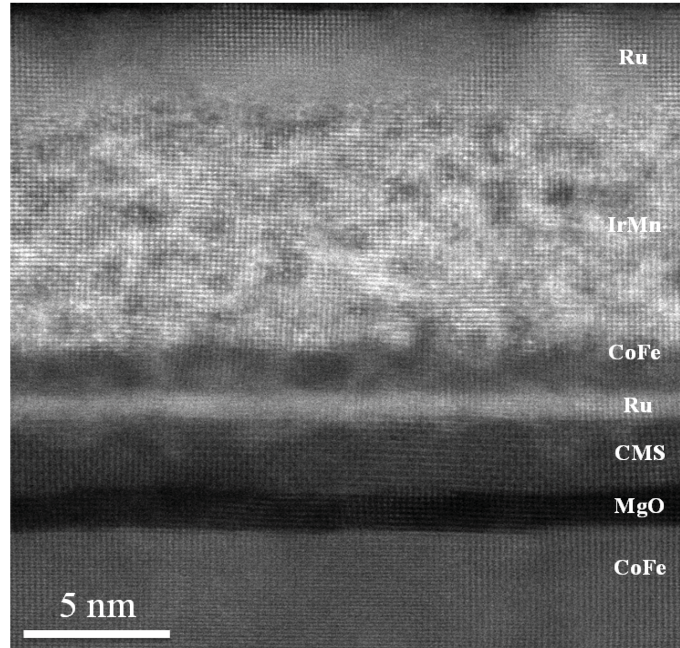

Figure 2.3.1 A typical HRSTEM image of a CoFe/MgO/CMS MTJ

All the electronic-magnetic lenses in the TEM or STEM have aberrations. Spherical aberration (C_s) and chromatic aberration (C_c) are the two main aberrations in the microscope. The development of aberration corrected STEM is necessary to improve the resolution to the sub-Angstrom regime. An aberration corrector produces negative C_s using multipole lenses, such as quadrupole-octupole and hexapole lenses. The negative C_s provided by the aberration corrector compensates the positive aberration of the objective lens,[95] and makes it possible to achieve a total of nearly-zero C_s.[102] Taking the advantage of aberration corrected STEM, we can use a larger probe-forming aperture to obtain a high beam current and high resolution.

So why are STEM images incoherent, and why is the intensity solely dependent on the atomic number? We will use a simplified case to demonstrate the incoherent imaging for STEM.[99] The probe can be described as a wave packet with amplitude $P(\boldsymbol{R})$ throughout the thickness of the specimen,

$$P(\boldsymbol{R}) = \int A(K) e^{i(K \cdot R)} dK \qquad (2.3).$$

The aperture function *A(K)* is

$$A(K) = H(K)e^{i\chi} \quad (2.4),$$

in which *H(K)* is the amplitude of the aperture function, which is zero outside of the aperture and one inside. χ is defined as

$$\chi = \frac{\pi}{\lambda}\left(\Delta f\theta^2 + \frac{1}{2}C_S\theta^4\right) \quad (2.5),$$

where Δf is the defocus. The aberration terms have been included in the phase x. The amplitude ψ_s scattered into the direction $\mathbf{K_f}$ can be calculated from the first Born approximation from

$$\Psi_S(\boldsymbol{K_f}) = c\int e^{-i\boldsymbol{K_f}\cdot\boldsymbol{R}} V(\boldsymbol{R})P(\boldsymbol{R}-\boldsymbol{R_0})dR \quad (2.6),$$

where $V(\boldsymbol{R})$ is the projected potential and $c = \frac{m}{2\pi h^2}$. Integrating the scattered intensity $|\Psi_S|^2$over all the final states $\mathbf{K_f}$**,** and using the identity

$$\int e^{-i\boldsymbol{K_f}(\boldsymbol{R}-\boldsymbol{R}')} dK_f = 4\pi^2\,\delta(\boldsymbol{R}-\boldsymbol{R}') \quad (2.7),$$

give the total scattered intensity as

$$I(\boldsymbol{R_0}) = \int\left|\Psi_S(\boldsymbol{R}-\boldsymbol{R_0})\right|^2 O(\boldsymbol{R})d\boldsymbol{R} \quad (2.8),$$

$$I(\boldsymbol{R_0}) = |\Psi_S|^2 \otimes O \quad (2.9),$$

in which, $\otimes$ represents a convolution of the probe intensity profile with an object function *O* given by

$$O(\boldsymbol{R}) = \sum_{i=1}^{N} Z_i^n \delta(\boldsymbol{R} - \boldsymbol{R_0}) \quad (2.10).$$

In **Equation (2.10)**, the value of *n* depends on the experimental condition, which can be determined by STEM image simulation under specific conditions. **Equation (2.9)** shows that the intensity of the image depends only on the atomic number Z and no phase is involved.

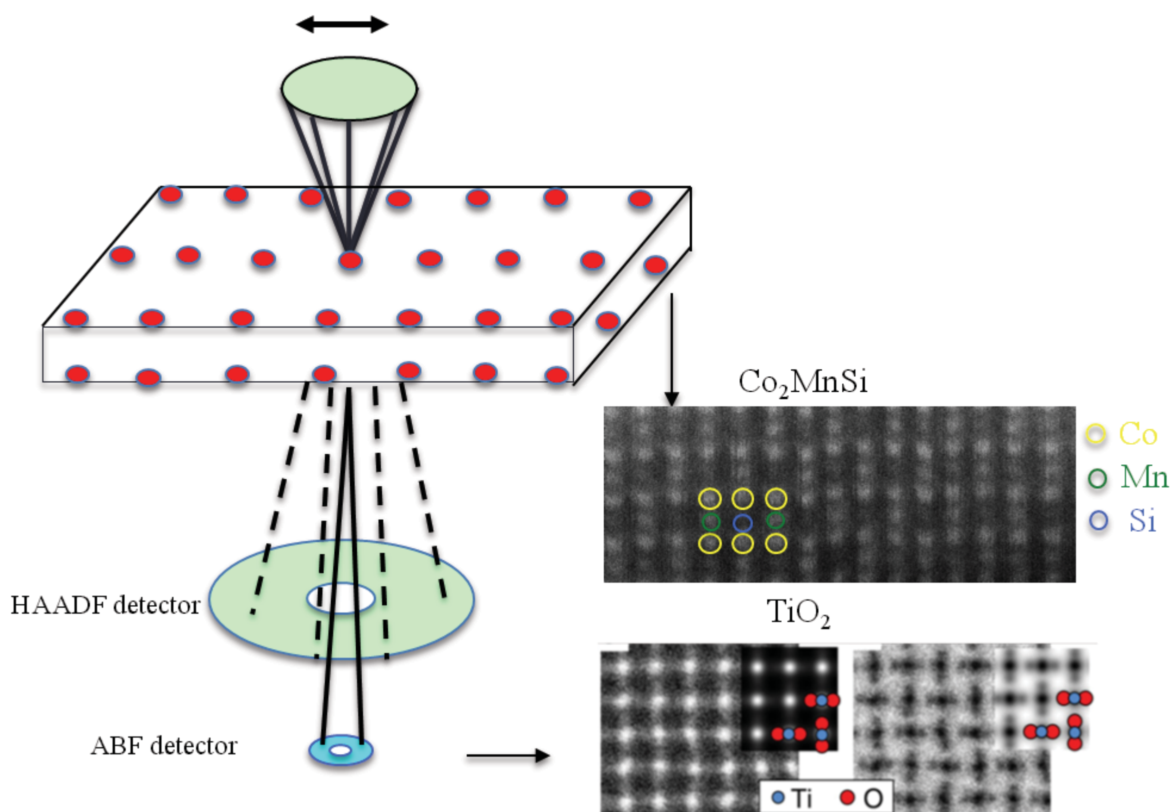

Figure 2.3.2 Schematic show of HAADF and ABF STEM. Examples of HAADF image of Co_2MnSi and ABF image of TiO_2 (Ref: [103]) are shown.

Due to the strong Z dependence of the intensity in HAADF STEM images, seeing light element columns can be difficult when there are heavy elements present in the same image, such as O atoms in Fe_3O_4. Annular bright field (ABF) imaging is a technique that allows us to reliably resolve light elements and heavy elements columns simultaneouly.[103] **Figure 2.3.2** presents a schematic of the detectors for HAADF and ABF STEM, in which the detector angle of ABF imaging is much smaller than that of HAADF imaging. The predominant electrons that contribute to the HAADF images are the thermal diffuse scattered electrons. For ABF imaging, the dominant contribution is signal from the elastically scattered electrons, which has a weak dependence on atomic number.

ABF and HAADF STEM share the same advantage of insensitivity to sample thickness,[104] which can be explained by *s*-state channeling theory. An *s*-state Bloch wave is tightly bonded to the atom columns, so with the electron probe positioning on the atom column, the *s* states are strongly excited compared to other states such as *p* states. Just as in HAADF STEM imaging, if the ABF detector angle spans a moderate range, some destructive interference occurs which reduces the coherence. The ABF imaging therefore is insensitive to the variation of the specimen thickness. The robust imaging of both light elements and heavy elements with respect to thickness of the sample is favorable compared to usual BF imaging.

ABF image is an absorption image; therefore, all the atoms appear dark on a bright background. For light element columns, the absorption effect is small, but for heavy element columns, the absorption is larger. To explore the optimal experimental conditions for ABF imaging, image simulation is needed.[104] For a probe convergence angle of 22 mrad, the optimal experimental conditions are 12 mrad and 22 mrad for the ABF detector inner and outer angle, respectively.

Figure 2.3.3 shows simultaneously acquired HAADF and ABF images of a Fe_3O_4 specimen along [110] zone axis. The HAADF image in **Figure 2.3.3** (a) shows that only Fe atoms are visible as labeled by the red circles, but the ABF image in **Figure 2.3.3** (b) shows both Fe and O (blue circles) columns simultaneously.

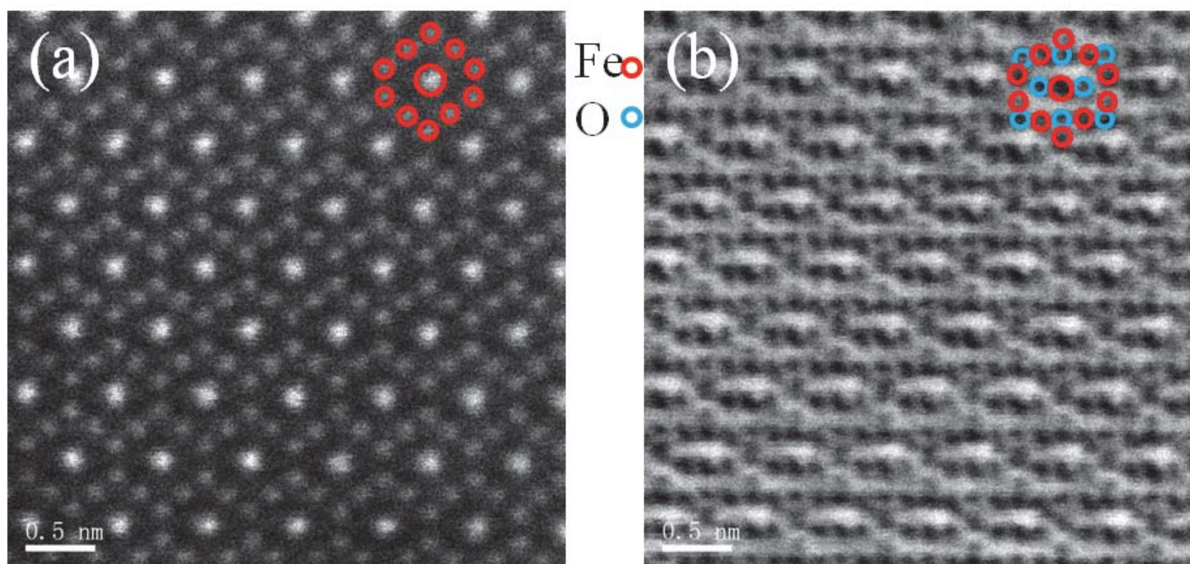

Figure 2.3.3 Simultaneously acquired HAADF and ABF images along Fe_3O_4 [110] zone axis are shown in (a) and (b), respectively.

2.3.2 STEM Image Simulation by Frozen Phonon Multislice Algorithm

Although STEM images are more straightforward to interpret than TEM images, we still need to compare our experimental results with the simulated images to obtain a quantitative understanding of the STEM image intensity, especially when defects or strains exists in the images.

The multislice algorithm is the most precise method of simulating non-periodic structures such as interfaces and defects. The simulated sample consists of a series of phase objects with the wave propagating in free space between them. The phase objects are “slices” through the whole sample, which is why the simulation algorithm is called “multislice”. Each slice should be thin enough to be a phase object. The approximation of the phase object is that an object changes the phase of the scattered electron wave but not the amplitude. When the phase change is much

smaller than 90° (π/2), the object is called a weak phase object (WPO). The exact slice thickness depends on the crystal structure of the sample, but ideally it is only one atom thick.

The basic steps to carry out the multislice simulation are as follows. (1) Divide the sample into thin slices according to its crystal structure. (2) Propagate the wave function through the whole sample model one slice at a time. TDS also needs to be included in the multislice simulation by using a frozen phonon algorithm.[105] The period of phonons is typically on the order of 10^{-3} s, 13 orders of magnitude longer than the time it takes for a 100 kV electron to propagate through a 100 nm specimen, ~ 10^{-16} s. As a result, we can make the frozen phonon approximation that when the electrons "travel" through the crystals, the lattice is "static" to electrons.

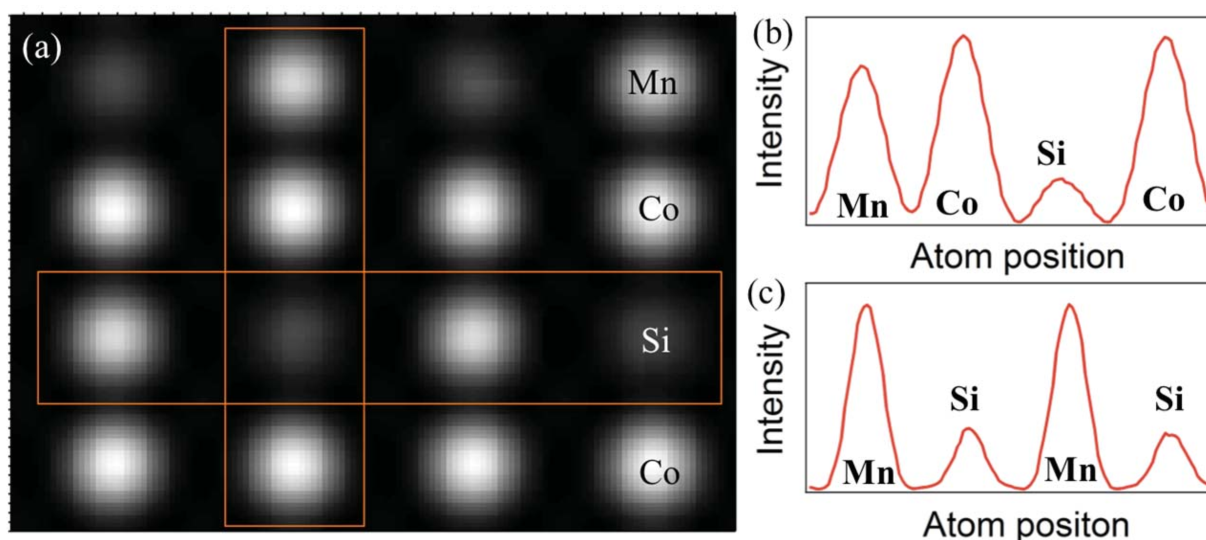

Figure 2.3.4 (a) Simulated STEM image of CMS along [110]. (b) and (c) are vertical and horizontal intensity profiles along the windows drawn in (a), respectively.

A 128×128 pixel simulated image of Co_2MnSi in the $L2_1$ with a thickness of 3.3 nm ordered structure along [110] is shown in **Figure 2.3.4 (a)**, with a thickness ~3.3 nm. Other simulation conditions include a beam energy of 200 kV, a convergence angle of 17.5 mrad and the HAADF detector angle of 53.9~269.5 mrad. **Figure 2.3.4 (b) and (c)** show the vertical and

horizontal intensity profiles taken in the orange windows in Figure 2.3.4 (a), respectively, which clearly show the different intensity of each column as labeled in the figures. Further analysis was done to investigate the “Z-contrast” behavior of the images in **Figure 2.3.4** (a). **Figure 2.3.5** shows the dependence of image intensity on camera length (CL). The plot in **Figure 2.3.5 (b)** shows that with different CL, the dependence of intensity on Z changes. The smaller the CL (CL = 77 mm), the more closely we can obtain the pure Z-contrast image: I $\sim Z^{1.7}$. The results of image simulation in **Figure 2.3.4** and **2.3.5** show that acquiring a pure Z-contrast image requires a smaller camera length. What changes when increasing CLs is the HAADF detector angle. Smaller CLs give larger HAADF detector angles. Larger HAADF detector angles suppress the diffraction and phase contrast in the STEM images, which leaves us a “pure” Z-contrast image. In experiments, however, the image intensity becomes dimmer as the CL becomes smaller. Therefore, compromise has to be made between Z-contrast image and image intensity.

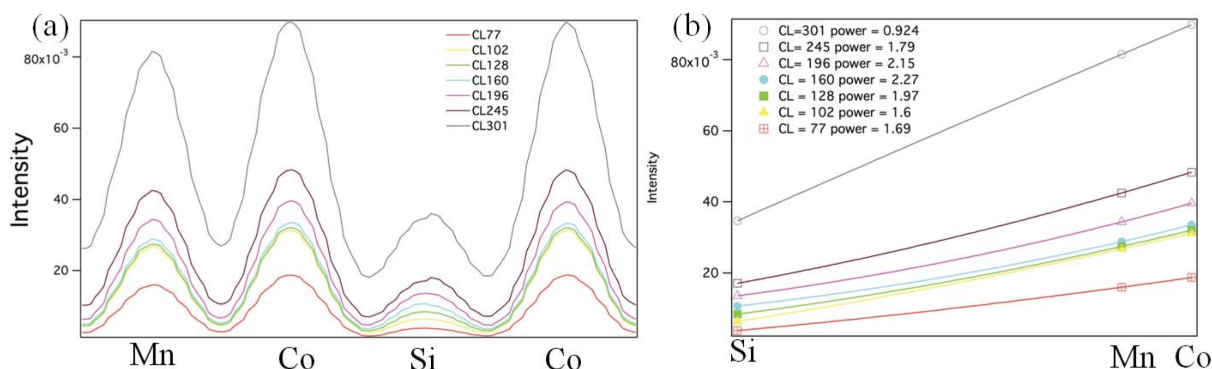

Figure 2.3.5 (a) A series of intensity profiles taken in the vertical window in Figure 2.3.4 (a) with different camera lengths (CLs). (b) Power law fittings for intensity at different CLs.

2.3.3 Thickness Measurement by Position Averaged Convergence Beam Diffraction

To compare simulated and experimental results, we must know the thickness of the experimental sample. There are several methods to measure the sample thickness including two-

beam convergent beam diffraction (CBED),[97] the electron energy loss spectroscopy (EELS) log–ratio approach[106] and position average CBED (PACBED).[107,108] Two-beam CBED for thickness measurements can be accurate down to the unit cell level for specimens with thicknesses >50 nm.[109] However, such thickness is too large to be useful for atomic resolution imaging in STEM. Furthermore, this method requires tilting the sample away from the zone-axis conditions used for imaging, potentially causing discrepancy between the areas used for imaging and those used in determining the thickness.

EELS log–ratio approach is also not suitable for determining the thickness of samples used in high-resolution STEM. If the inelastic mean free path is known, the log–ratio method can be accurate within ±10%.[110] However, for the thin (<20 nm) specimens used in lattice resolution imaging, surface plasmons begin to play a critical role and the accuracy and precision decrease dramatically.[111] Other aspects of EELS will be discussed in Chapter 3.3.[106]

Compared to the other two methods, PACBED provides more accurate values of sample thicknesses from 0 to 100 nm, with sample tilts of less than 1 mrad.[112] Furthermore, we can use the same optical condition of the microscope for HRSTEM, which means that the patterns can be recorded accompanying the STEM images. The PACBED method is universal as long as unit-cell sizes are small enough so that only the first or second order Bragg angles are within the convergence semiangle. While more accurate thickness determination is possible by applying pattern-matching simulation,[113] the accuracy of PACBED is sufficient for thin specimens used for HRSTEM imaging.

The theory of PACBED patterns can be analogous to the CBED patterns, which is well established for simulation.[105] Therefore, we can simulate the PACBED patterns in a way similar to CBED.

At the entrance surface of the sample, the wavefunction for a STEM probe is

$$\psi(h, z=0) = A(h)\, exp\,(-2\pi i h \cdot R) \quad (2.11).$$

The intensity a single CBED pattern can be calculated as in:

$$I\ (\boldsymbol{q}+\boldsymbol{G},\boldsymbol{R},t) = \sum_H |S(\boldsymbol{q},t)A(\boldsymbol{q}+\boldsymbol{H})\ exp(-2\pi i(\boldsymbol{q}+\boldsymbol{H})\cdot\boldsymbol{R})\ |^2 \quad (2.12),$$

in which S is the scattering matrix. The PACBED pattern is the average of all CBED patterns for different probe positions.

$$\bar{I}\,(\boldsymbol{q}+\boldsymbol{H},t) = \sum_H |S(\boldsymbol{q},t)H(\boldsymbol{q}+\boldsymbol{H})|^2 \quad (2.13),$$

from which we can see that the intensity of the PACBED pattern is also independent of the aberrations.

Experimentally, we scan the beam with a large convergence angle across a relatively small area (1 nm × 1 nm), which typically contains a few unit cells of the specimen, and at the same time, we acquire the PACBED pattern with the Gatan GIF camera. For PACBED simulation, a series of CBED patterns are simulated as a function of probe positions and then averaged together.

PACBED doesn't work for amorphous materials, so the measured thickness is only the thickness of the crystal part of the specimen, not amorphous overlayers.

2.4 Cs Corrected STEM Electron Energy Loss Spectroscopy

2.4.1 Basics of Electron Energy Loss Spectroscopy

Electron energy loss spectroscopy (EELS) uses inelastic scattered electrons to characterize the chemical information of materials.[106] Some electrons lose a fraction of their energy by an inelastic scattering process. Each element has a unique energy loss spectrum, which can be used as identification for chemical states. A typical complete EEL spectrum has three

parts: zero-loss peak, low loss peaks including plasmon-loss peaks and core-loss peaks. The zero-loss peak (ZLP) is usually used to align the spectrometer. The full width of half maximum (FWHM) of the ZLP can be used to define the energy resolution of the entire EELS spectrum. The plasmon peak arises from excitation of plasmons, collective oscillations of the valence electron density of the sample. We can obtain the local thickness of the sample (t) by the log-ratio method based on the intensity ratio between zero loss peak and plasmon peaks, as shown in Equation (2.14).

$$t/\lambda = \log(I/I_0) \quad (2.14),$$

in which t is the thickness of the sample, λ is the electron inelastic mean free path; I_0 is the intensity of the zero loss peak, and I is the intensity of the plasmon peak. Equation (3.14) shows that measurements of the thickness of the sample rely on an accurate knowledge of λ.

Energy resolution and spatial resolution are two key factors in EELS. The energy resolution is determined by the spectrometer and the electron source. In TEM mode, the spatial resolution is a function of the spectrometer entrance aperture and its effective size at the plane of the specimen. In STEM mode, the spatial resolution of EELS is the size of the probe. Taking advantage of the Cs corrector and the large condenser aperture, a sub angstrom probe can be obtained[106] with more current and in a much more compact form compared to the illumination in TEM mode, which allows us to characterize interfaces without delocalization caused by the tails of the probe.[111] However, in a real sample, the probe broadens as electrons travel through the sample. Electrons spread laterally into the sample due to the elastic scattering, which degrades the spatial resolution of EELS. The illuminated volume is proportional to $t\alpha$ in which α is the convergence angle. However, the broadening effect is less prominent for a crystalline sample due

to the electron channeling,[114] which delays the beam broadening up to several nm below the entrance surface. This channeling effect enables the atomic resolution in STEM EELS mapping.[111]

The spatial resolution of EELS is also limited by the width of the associated interaction potential.[111] Based on the classical description of the particle scattering, the delocalization problem arises since the inner-shell electron ejected by the passage of a high–energy electron will scatter some distance away from the atom. The length scale of this delocalization problem is about 2~5 nm and inversely proportional to the energy loss. In the case of the core level loss in samples discussed here, (typically a few hundred to ~1000 eV), delocalization caused by the inelastic scattering is a smaller effect than residual probe aberrations.[106]

Information of chemical states of the specimen can be extracted from the core-loss peaks. The core-level electrons in the sample are excited to the empty states above the Fermi level. Variations in the single scattering intensity $I(\Delta E)$ can be described by the Fermi's Golden rule[111]

$$I(\Delta E) \propto d\sigma/dE \propto |M(E)|^2 \delta(E_i - E_f - \Delta E) N(E) \quad (2.15),$$

in which σ is the cross section of the scattering event; *M(E)* is an atomic transition matrix, which affects the overall shape of the element edge in EELS and is determined by the atomic physics; *N(E)* is the empty density of state (DOS), which depends on the chemical and crystallographic environment of the excited atom; the delta (δ) function enforces the conservation of energy. Because the core-level states are highly localized, *N(E)* is a local density of states at the site of excited atom. From **Equation (2.15)**, transitions occur only when the final states are empty, so EELS is sensitive to the unoccupied states above the Fermi level. The transition usually obeys the dipole transition rule, which requires that $\Delta l = \pm 1$ where l is the annular momentum. The

dipole transition rule applies to the prominent $L_{2,3}$ edges of transition metals elements and $M_{4,5}$ edges of the lanthanides, which have a high density of unfilled 4f states. If the collection angle is big compared to the momentum transfer, non-dipole transition (dipole forbidden transition) can also be captured in the spectrum and affect the shape of the edges.[111] For example, $M_{2,3}$ edges of La_2O_3, which corresponds to $\Delta l = 2$, has been observed when using a 100 mrad collection angle.[111]

Core-loss spectra show pronounced fine structure within 50 eV of the ionization threshold, which is called near edge fine structures (ELNES).[111] ELNES is related to the local DOS, which reflects the charge redistribution in bonding or the nature of the conduction bands. Consequently ELNES provides information on charge distribution, conduction band, coordination and structures of the local states.[115] The ELNES spectrum is unique for each compound and hence can be used as fingerprints to precisely identify a compound.. In addition, the signal at the near-edge region is also strong compared to other regions and can be used as a monitor for local defects.

The disadvantage of ELNES is the lack of an accurate model to describe all edges in all materials. The core-hole in the inner shell is one of the factors that prevent us from achieving a simple interpretation of the ELNES. In the case where the core-hole effect dominates ELNES provides information about the excited state instead of the ground state electronic structures of the materials. For metals, the core hole effect is often negligible because the core hole is well screened by the free electrons in the metal. For ionic insulators, a core hole effect is also small. For covalent insulators or even semiconductors, however, the qualitative chemical behavior is difficult to describe. For example, the core hole effect has a considerable effect close to the threshold in Si, a typical semiconductor. The difference between the theoretical calculation

(ground state) and experimental result is about 0.1 eV for the threshold energy loss. In transition metal carbides, the core hole effect as large as 1-2 eV has been reported for the threshold enegy.[116] Therefore, although ELNES can give us information about the local electronic structures of the sample, core hole effects need to be considered in order to fully understand the ELNES of the materials of interest.

The intensity of core-loss edges can be used to measure the compositions of the specimen. For a specimen with two elements *a* and *b*, the atomic ratio *a* to *b* can be calculated as follows

$$\frac{N_a}{N_b} = \frac{I_{ka}(\beta,\Delta_a)}{I_{jb}(\beta,\Delta_b)}\frac{\sigma_{jb}(\beta,\Delta_b)}{\sigma_{ka}(\beta,\Delta_a)} \quad (2.16),$$

in which *N* is the areal density (atoms per unit area) of the element, equal to the product of its concentration and the specimen thickness; Δ_a and Δ_b are the energy integration windows for *a* and *b* separately; *j* and *k* are the indices of edges and β is the collection angle; σ is the cross section.

EELS is particularly suitable for light element analysis such as C, O and N. Transition metals also show strong *L* edges in the EEL spectra. However, for heavy elements such as Au and Pt, energy dispersive spectroscopy (EDX) is better for measuring composition.

2.4.2 EELS Spectrum Imaging and Data Processing

One of the key advantages of STEM is that any signal that varies with the probe position can be used for imaging. The difference in angular distributions of the elastic scattering and inelastic (or thermal diffuse) scattering ensures that we can acquire both signals simultaneously using the ADF detector and EELS spectrometer respectively. Since the ELNES of core loss signals reflects the local density of electronic states, the combination of STEM imaging and

EELS allows us to explore the structure and chemical information at the same time; it even allows atomic resolution mapping of the electronic structure of the materials.[117]

The EEL spectrum image (SI) is a 3D data matrix, in which each pixel in the SI contains full chemical and position information.[106,118] An EELS SI data cube contains the probe positions expressed in x and y as well as the energy loss ΔE.[119] The acquisition of EELS SI can be time consuming, thus the sample drift can induce artifacts including loss of spatial resolution and apparent mixing at interfaces.

In order to minimize the sample drift, we have to compromise between acquisition time and spectrum signal-to-noise ratio. As we reduce the exposure time, sample drift is reduced, but noise increases. Weighted principle component analysis (PCA) is often introduced to de-noise the EELS SI data set.[120] The general concept of PCA is to reduce the dimensionality of the original data matrix by excluding noise, leaving only the components that sufficiently describe the original dataset without losing significant information.

Mathematically, we first decompose the EELS SI data matrix with dimension $((x \times y), \Delta E)$ into two matrices, a score matrix and a loading matrix, according to Bosman *et al.*[120] Each row of the loading matrix $((x \times y), \boldsymbol{n})$ contains the eigenvalues of the original EELS SI data matrix, which are maximally uncorrelated with each other. Each column of the score matrix $(\boldsymbol{n}, \Delta E)$ contains the amplitude of the eigenspectrum in the loading matrix. $\boldsymbol{n}$ is equal to the smaller dimension between $(x \times y)$ and ΔE. The individual product of each row of the loading and column of the score matrices is called a principal component. The matrix decomposition can be performed by singular value decomposition (SVD).[120] In the decomposed matrices, the principal components are ordered from high to low by the fraction of the total spectral variance they represent. Thus,

the first few principles components represent the real, correlated signal in the SI and the rest of the components represent uncorrelated noise. After decomposing and reordering, the principle components can be used to reconstruct the data matrix. Since the number of meaningful principle components is much smaller than the data dimension ***n***, the noise contribution can be greatly reduced. Therefore, PCA is a mathematical approach that allows us to identify independent spectra features as principle components, reduce the noise components, and finally reconstruct the data matrix.

Weighted PCA is an optimized approach to deal with noisy data. The data is typically weighted by the standard deviation of the Poisson counting noise of the data matrix, which is equal to the square root of the number of counts. This weighting considers the fact that the experimental noise varies with the detector channels and pixel numbers. Weighted PCA allows us to reorganize the data matrix and normalize the distributions of the data noise.[120] Therefore, when processing EELS SI data, we used the weighted PCA instead of the pure PCA.

2.5 Experimental Conditions for STEM Imaging and STEM EELS

HRSTEM experiments were performed on a FEI Titan STEM with CEOS probe aberration corrector operated at 200 kV with a spatial resolution ~0.1 nm, 24.5 mrad convergence angle and 25 pA probe current. Unless otherwise noted, the high-angle annular dark-field (HAADF) detector subtended 54 to 270 mrad. All the HRSTEM images have been smoothed with a Gaussian filter smaller than the 0.1 nm instrumental resolution to reduce shot noise.

Annular bright field STEM images were acquired with collection angles of 11 to 24 mrad. Z-contrast images simultaneously acquired with ABF images required collection angles of 112 to 560 mrad, resulting in higher noise in the Z-contrast image.

Unless otherwise noted, the EELS SIs were acquired with energy resolution of 0.8 eV, convergence angle 24.5 mrad, and collection angle 52 mrad. EELS SIs were acquired on a GIF 865 equipped on the Titan, with energy dispersion 0.2 eV/pixel. EELS quantifications were carried out by DigitalMicrograph software, which implements the standard quantification method described by Egerton.[111] All EELS SIs were processed by weighted PCA, now a plugin in DigitalMicrograph. The number of principle components that were used to reconstruct the data varied from SI to SI.

Chapter 3 High quality ferromagnetic electrodes with high spin polarization

3.1 Optimization of Fe_3O_4 Thin Films on Buffered Si Substrate

The negative spin polarization in Fe_3O_4 can produce a negative TMR in an MTJ with a positive SP second electrode like CoFe. Negative TMR means that the highest tunneling resistance is for parallel electrode magnetizations according to Julliere's model, as shown in Equation (1). However, most MTJs with a single Fe_3O_4 electrode have not produced inverse TMR, or any TMR of large magnitude.[56,121-123] One of the reasons may be defects and other Fe oxide phases in the Fe_3O_4 electrodes.[56,121,124] Two approaches could increase TMR in Fe_3O_4 based MTJs. First, development of high-quality Fe_3O_4 thin films could let its fundamental spin characteristics emerge in MTJs. Second, Fe_3O_4 / tunnel barrier interfaces need to be flat, since the performance of MTJs depends on the interfaces between the ferromagnetic electrodes and the tunnel barrier.[47] In particular, coherent tunneling, which contributes to the extremely high TMR of Fe/MgO[125] and related devices like CoFeB/MgO[126], requires flat interfaces to preserve the in-plane carrier momentum.[18] Therefore, a low defect density, smooth ferromagnetic electrode is essential for high-performance MTJs. We explored the growth of Fe_3O_4 thin films grown by different methods including reactive sputtering and selective oxidation. We found that with selective oxidation, the quality of Fe_3O_4 thin films on buffered Si is comparable to films grown by molecular beam epitaxy (MBE).

3.1.1 Fe_3O_4 Thin Films Grown on TiN buffered Si by Reactive Sputtering

Thin Film Fabrication

We first fabricated the Fe_3O_4 thin films by reactive sputtering. Dr. Hua Xiang prepared the multilayer stacks by DC magnetron sputtering. Multilayer stacks with the structure of Si / TiN (10) / Fe_3O_4 (*t*) (nm) were grown by DC magnetron reactive sputtering in a home-built system with base pressure better than 1.0×10^{-7} Torr. The TiN buffer was prepared at 550 °C.[77] The same deposition system was used for other thin films fabrication. Therefore, the descriptions of the depositing system will not be described in Chapter 3 and 4. After the substrate was cooled to RT, Fe_3O_4 layers with different thicknesses (*t*) were deposited on the TiN/Si structure at substrate temperatures (T_s) of RT, 150, 250, 300, and 400 °C, by three different dc sputtering powers, 30, 60, and 120 W.

Results and Discussions

Optimal fabrication conditions were explored by X-Ray diffraction (XRD) done by Dr. Hua Xiang. The depositing power and T_s played important roles in the growth of Fe_3O_4 thin films. The XRD results indicated that with smaller sputtering power (30 W), the Fe_3O_4 films had better quality compared to the one grown with large sputtering power (120 W). XRD results showed that the full width of half maximum (FWHM) of Fe_3O_4 (400) peak deceased as T_s increased up to 400 °C, indicating the improvement of the Fe_3O_4 crystal quality.

In **Figure 3.1.1 (a)**, a TEM image shows a Fe_3O_4 thin film with columnar growth was formed, despite the fact that we have epitaxial growth Fe_3O_4 on TiN buffered Si at T_s = 250 °C, which is indicated by the selective area diffraction (SAD) pattern shown in **Figure 3.1.1 (c)**. The formation of Fe_3O_4 was confirmed by XPS, showing both Fe^{2+} and Fe^{3+} peak, which is characteristic for Fe_3O_4. No satellite peak in between Fe $2p_{1/2}$ and Fe $2p_{3/2}$ indicates no Fe_2O_3 existing in the Fe_3O_4 thin film.[127] Due to the columnar growth, a rough Fe_3O_4 surface is shown in **Figure 3.1.1 (b)**, including a deep gap between two grains, indicated by an orange arrow. This

huge roughness would be detrimental to coherent tunneling in the MTJs with Fe_3O_4/MgO structure.[125]

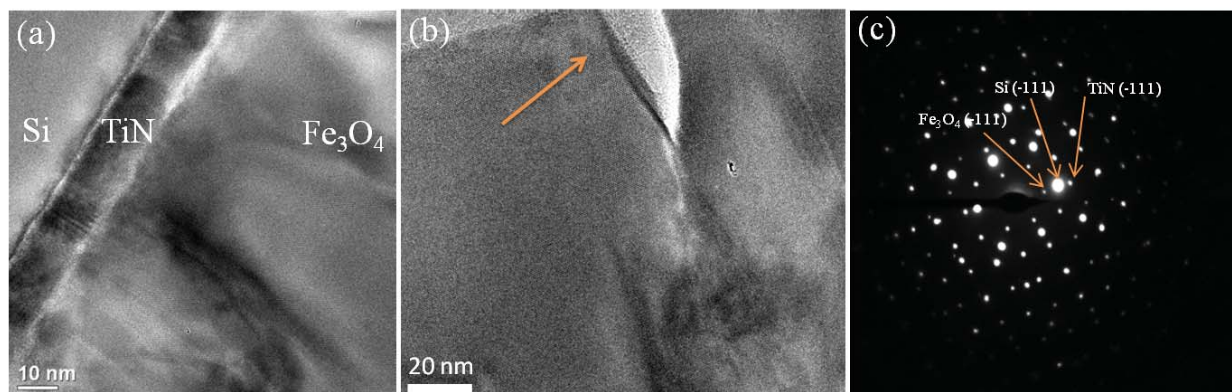

Figure 3.1.1 Low magnification and HR-TEM images along the Si [110] zone axis of the 270 nm Fe_3O_4 films deposited on TiN buffered Si (001) at 250 °C, (b) the surface of the Fe_3O_4 thin film grown at 250 °C, the arrow indicates a gap on the surface (c) selected area diffraction pattern of the entire Si (001)/TiN/Fe_3O_4 stack.

Magnetization loops measured on the Fe_3O_4 thin films grown at T_s = 300 °C and T_s = 400 °C are shown in **Figure 3.1.2**. The effects of the Si / TiN bilayer have been subtracted from the data. The magnetization of the Fe_3O_4 film is still not completely saturated even up to 6000 Oe, which is due to the antiferromagnetically coupled APBs arising from Fe sublattice stacking faults.[59] APBs also lead to super-paramagnetic behavior of Fe_3O_4 when the thickness of Fe_3O_4 is less than 5 nm, making such films useless for MTJs.[59,61,62,128] The density of APBs is strongly influenced by the growth conditions and the substrate.

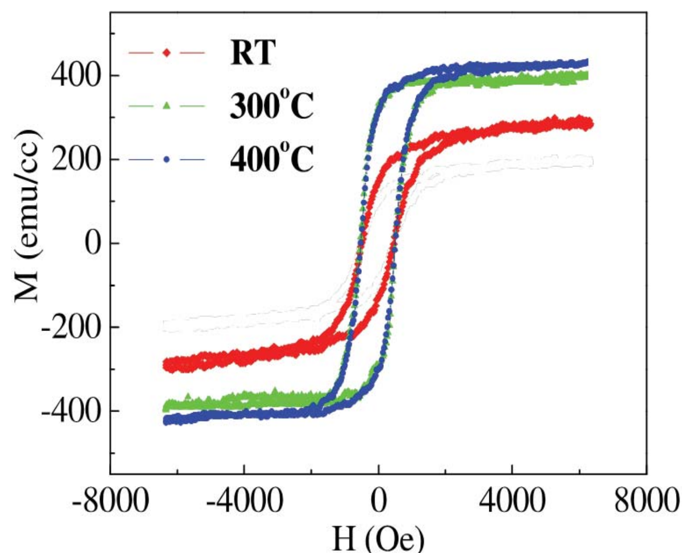

Figure 3.1.2 The RT magnetization loops of the 270 nm-thick Fe_3O_4 films prepared at different *T*s on TiN buffered Si (001). Acquired by Dr. Hua Xiang.

3.1.2 Fe_3O_4 Thin Films Grown by CO_2/CO Selective Oxidation on a Ag (TiN) Buffered Si Substrate

Introduction

The surface roughness of Fe_3O_4 thin films grown on MgO substrates is typically smaller than one unit cell of Fe_3O_4, and the smallest reported roughness is 0.2 nm.[129] A typical roughness for Fe_3O_4 thin film on Si[130-132] is larger than 1 nm. In order to achieve thin films with smoother surface and lower defect density on Si, we applied a novel oxidation method to let the Fe_3O_4 form in equilibrium by selective oxidation of a smooth Fe thin film.

Fe_3O_4 has been synthesized previously by post-annealing an Fe thin film in an O_2 atmosphere.[49,133,134] In most cases, post-annealed Fe_3O_4 films show smaller saturation magnetization fields than films deposited as Fe_3O_4 directly due to a lower density of APBs.[134,135] However, reliably controlling the formation of single-phase Fe_3O_4 is difficult. Mori *et al.*[136] reported that the oxide formed by exposing a bulk Fe (110) at 300°C to 1×10^{-6} Torr O_2 is FeO.

On the other hand, Kim et al.[137] reported that the final product of oxidation of a Fe (110) film at 250 °C in 5×10^{-7} Torr O_2 can be Fe_3O_4, depending on oxidation time and oxygen partial pressure.

Experimentally, we can utilize a mixture of two gases with a defined ratio such as $CO_2(g)/CO(g)$ and $H_2O(g)/H_2(g)$ to control the O_2 partial pressure through the chemical reactions $2CO + O_2 \leftrightarrow 2CO_2$ and $2H_2 + O_2 \leftrightarrow 2H_2O$, respectively.[138] By precisely controlling the ratio of the two gases, we can select the O_2 partial pressure that allows Fe_3O_4 to form in thermodynamic equilibrium. Here, we used a thermodynamic calculation to determine the specific P_{CO2}/P_{CO} ratio range which allowed us to form Fe_3O_4. **Figure 3.1.3** shows the calculated Fe-O phase diagram in terms of temperature (T) and log (P_{CO2}/P_{CO}). From the reaction equilibrium between O_2 (g), CO_2 (g) and CO (g), the P_{CO2}/P_{CO} ratio corresponding to certain fixed oxygen chemical potential can be readily obtained by thermodynamic calculations based on the known Gibbs energies.[138]

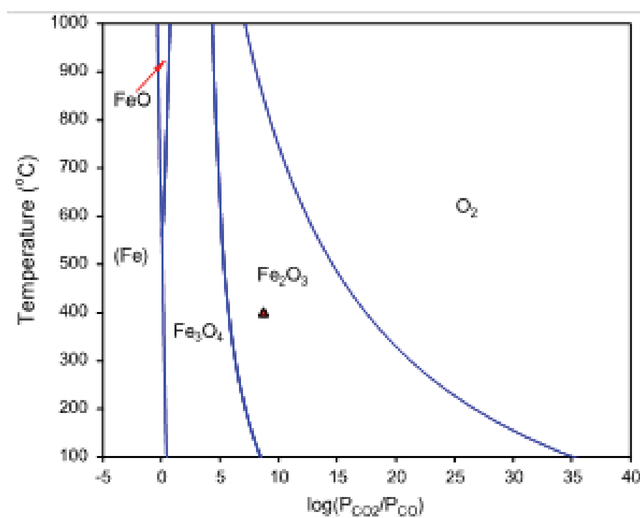

Figure 3.1.3 The calculated Fe–O phase diagram in terms of temperature as a function of $\log(P_{CO2}/P_{CO})$. The red triangle represents the P_{CO2}/P_{CO} ratio with the same chemical potential as pure O_2 at 10^{-7} Torr. Calculated by Dr. Chuan Zhang.

Thin Film Fabrications

The TiN buffer was reactively sputtered on Si substrates via domain matching epitaxy (DME)[139] in a 6 mTorr Ar and 0.5 mTorr N_2 mixture at a substrate temperature of 550 °C.[140] Ag

buffers were deposited at RT in 3 mTorr Ar. Epitaxial Fe was grown at room temperature and then annealed at 400 °C for 10 min to both improve the epitaxial growth quality and reduce the surface roughness. We used a CO_2/CO 1000:1 gas mixture to selectively oxidize the Fe layer. Epitaxial Fe_3O_4 thin films were produced by oxidation at 160 °C under 100 Torr of CO_2/CO and at 400 °C under 6 Torr. The details of TEM sample preparations are described in **Chapter 3.1**. Magnetization loops were measured by vibrating sample magnetometry (VSM). Surface roughness of the Fe_3O_4 thin films was measured by atomic force microscopy (AFM).

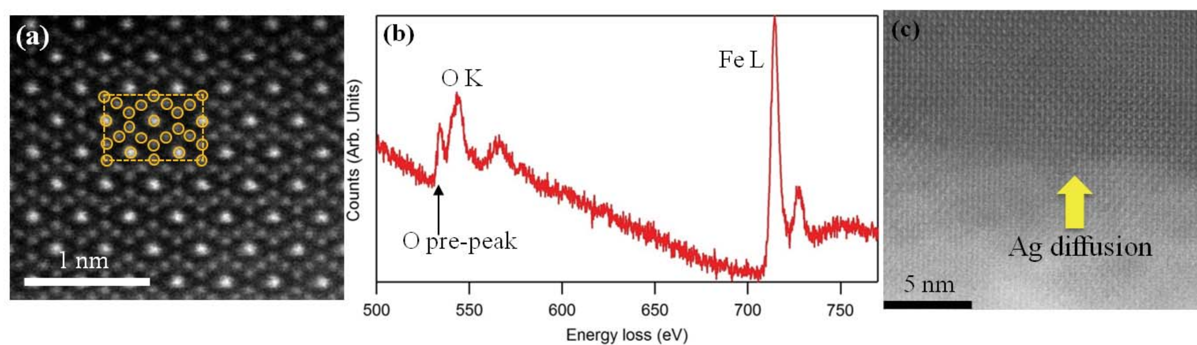

Figure 3.1.4 (a) HR-STEM image of the oxidized Fe_3O_4 structure; (b) EEL spectrum on the Fe_3O_4 layer, including the distinct O pre-peak, O K and Fe L edges. (c) HRSTEM image shows the Ag diffusion from the buffer layer.

Results and Discussions

First, we fabricated Fe_3O_4 by selective oxidation on Ag buffered Fe_3O_4.[23] The rms roughness measured by AFM was 0.61±0.03 nm, which was much smoother than the reactively sputtered Fe_3O_4 thin film. As shown in **Figure 3.1.4 (a)**, the HRSTEM image shows the Fe_3O_4 thin film along the [110] zone axis. The red circles in **Figure 3.1.4 (a)** present the positions of the Fe columns, and O columns are not visible due to its low atomic number. The dashed rectangle box defines a unit cell along Fe_3O_4 [110] zone axis. The EEL spectrum in **Figure 3.1.4 (b)** shows clear O K and Fe $L_{2,3}$ edges. The shape of the O K edge pre peak reflects the Fe

valence states, which is consistent with the results we obtained on a Fe_3O_4 nanoparticle standard sample as shown in **Figure 3.1.5**. In **Figure 3.1.5**, we intentionally added offset to the spectrum in red, otherwise two spectra are almost identical, especially the first three peaks. More detailed investigation on O K edges in Fe oxides is discussed in **Chapter 6**.

Selective CO_2/CO oxidation of Fe on Ag-buffered Si yielded Fe_3O_4 with somewhat lower surface roughness,[23] but during growth, the Ag diffuses into the Fe_3O_4 thin film, as is shown in **Figure 3.1.4** (d). Thus, instead of using Ag as the buffer, we used TiN, which also epitaxially grows on Si by domain match epitaxy.[141]

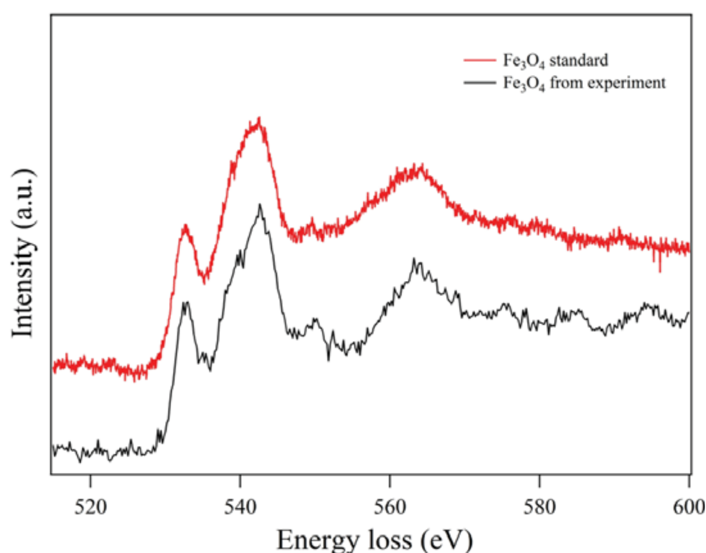

Figure 3.1.5 EEL spectra of O K edge of Fe_3O_4 from experiment and a Fe_3O_4 standard.

Figure 3.1.6 (a) is a HRSTEM image of a Fe_3O_4 thin film on TiN buffered Si produced by selective oxidation at 160 °C, showing the Fe_3O_4 lattice along a [110] direction. The HRSTEM image in **Figure 3.1.6 (b)** shows a sharp interface between the TiN buffer and the unoxidized Fe. There are nanovoids at the Fe_3O_4/Fe interface that are associated with the steps of the Fe layer, as is indicated by the orange dashed lines in **Figure 3.1.6 (c)**. **Figure 3.1.6 (d)** shows an AFM image of the Fe_3O_4, indicating an rms roughness of 0.34±0.03 nm. This is

comparable to the roughness of Fe_3O_4 thin films on MgO,[142] and much smoother than the sputtered Fe_3O_4 on buffered Si.[130]

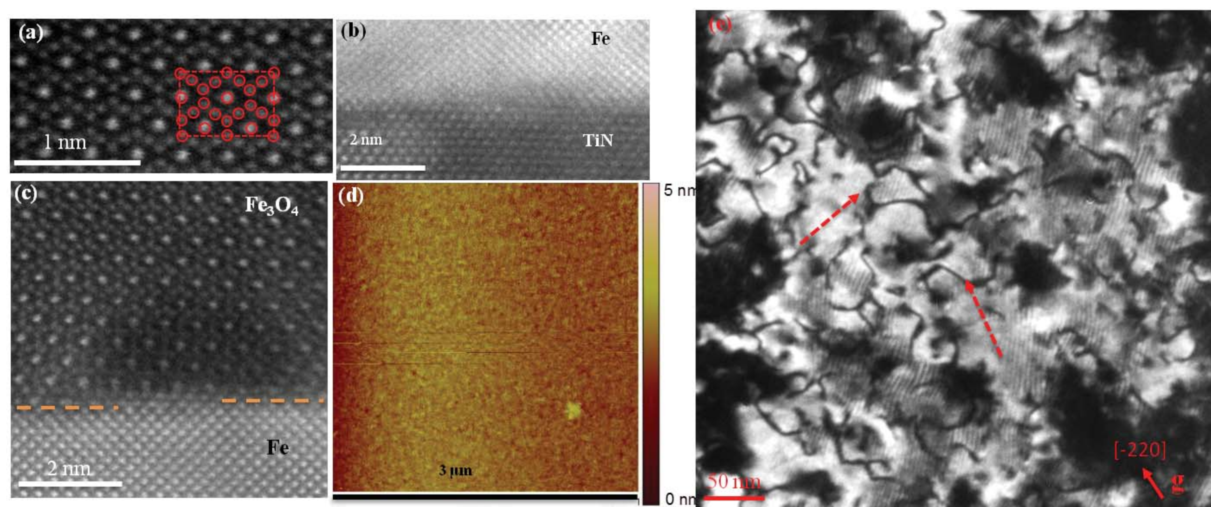

Figure 3.1.6 Results on Fe_3O_4 thin films grown at 160 °C. (a) HRSTEM on Fe_3O_4 thin film. The red dots are the positions of Fe columns (b) sharp interfaces between TiN and Fe (c) HRSTEM image of the defect at the interface of Fe_3O_4 and Fe. The dashed orange lines indicate the steps of the Fe (d) AFM on the Fe_3O_4 thin film. (e) Dark field TEM image using the (220) reflection for the [001] orientated Fe_3O_4 thin film grown at 160°C with a thickness 19.34 nm.

The APBs of a Fe_3O_4 thin film grown at 160 °C with a thickness ~19 nm are shown in **Figure 3.1.6 (e)**. The antiphase domain size of our Fe_3O_4 thin film is 50~100 nm, which is more than twice the length and four times the area of previous antiphase domains in Fe_3O_4 thin films with similar thickness grown on Al_2O_3 substrates.[143] The size of anitiphase domains in Fe_3O_4 generally increases with film thickness, but the domain size for our Fe_3O_4 thin film is comparable to or even larger than previously reported for 50 nm thick Fe_3O_4 thin films on α-Al_2O_3 (0001) by MBE[143] and on MgO substrates.[144] The magnetization loop of this structure (not shown) is dominated by residual, unoxidized Fe below the Fe_3O_4.

Under oxidation at 400 °C, Fe_3O_4 still forms, as is shown in the HRSTEM image in **Figure 3.1.7** (a). The pre-peak feature of the O K edge and the Fe L edge extracted from an

EELS SI taken on the area in **Figure 3.1.7 (a)** are shown in **Figure 3.1.7 (c)**. **Figure 3.1.7 (b)** shows that there is a second phase formed at the interface between TiN and Fe. EELS on the reaction layer, shown in **Figure 3.1.7 (d)**, has distinct Ti L, O K and Fe L edges. The measured atomic ratio Fe/Ti is 2.1±0.2 by EELS. The crystal structure of the second phase is consistent with Fe_2TiO_4, also known as ulvöspinel, which is an inverse spinel with similar lattice parameter to Fe_3O_4 with Ti^{4+} occupying the octahedral B sites.[145,146]

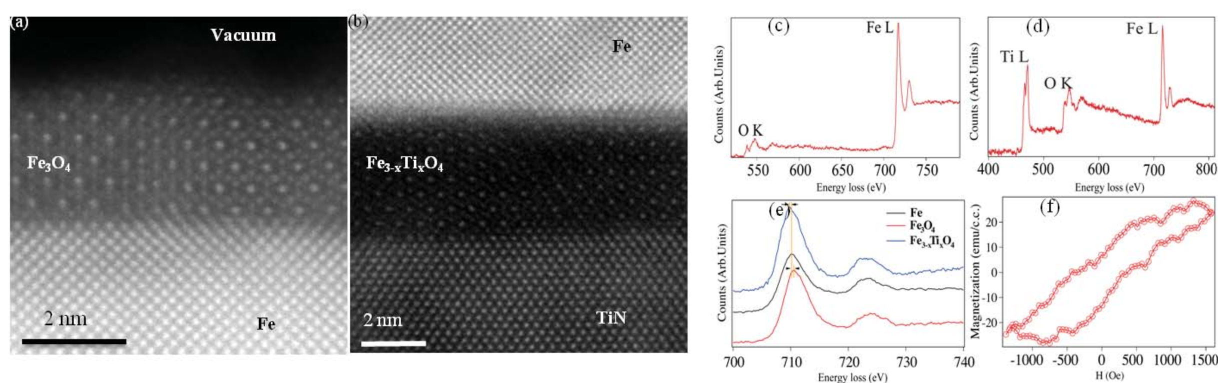

Figure 3.1.7 HRSTEM and EELS results on Fe_3O_4 thin films grown at 400 C. (a) HRSTEM image on Fe_3O_4 with a sharp interface in between Fe_3O_4 and Fe. (b) HRSTEM on interface between TiN and Fe, with the reaction layer. (c) EELS on Fe_3O_4 thin film with O K edge ELNES and Fe L edges. (d) EELS on the reaction layer shows Ti L, O K and Fe L edges. (e) Fe L edge core level shift among Fe_3O_4, Fe and $Fe_{3-x}Ti_xO_4$. The shift between Fe_3O_4 and Fe is 0.33 ± 0.04 eV to the higher energy loss; Fe L edge on $Fe_{3-x}Ti_xO_4$ shifts 0.51 ± 0.05 eV to the to the lower energy loss compared to Fe. (f) Magnetization loop for Fe_3O_4 thin film grown at 400 °C for 6 hr.

Fe_2O_3 and Fe_3O_4 are difficult to distinguish from the HRSTEM images, but O K edge ELNES[147] and Fe L edge core level shifts[148] can reflect the Fe valence in Fe oxides. The splitting between O K edge pre peak and main peak shown in **Figure 3.1.7 (c)** is consistent with our EELS measurement on a Fe_3O_4 standard under similar experimental conditions. The Fe L edge on Fe_3O_4 shifts 0.33±0.05 eV to the higher energy loss compared to the un-oxidized Fe shown in **Figure 3.1.7 (e)**, which is consistent with the formation of Fe_3O_4.[148] The relative Fe L edge shifts among Fe, Fe_2TiO_4 and Fe_3O_4 are shown in Figure **3.1.7 (e)**. The Fe L edge of the Fe_2TiO_4 is

shifted 0.51±0.05 eV to lower energy compared to Fe. That is smaller than the reported value,[148,149] which may suggest the second phase is non-stoichiometric. The magnetization loop of this structure in **Figure 3.1.7 (f)** shows paramagnetic-like behavior, which we attribute to the magnetic properties of the second phase.[150]

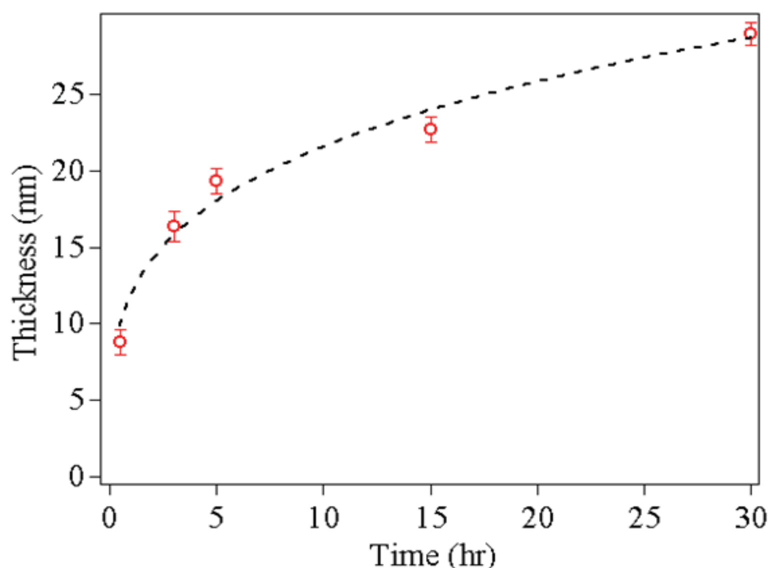

Figure 3.1.8 A power law growth model for Fe_3O_4 grown at 160 °C fitting by $x=At^m$ in which x is the thickness, t is the growth time, A is the constant and m is the power.

Growth kinetics for the Fe_3O_4 thin films grown at 160 °C are shown in **Figure 3.1.8**. A power law $x = At^m$ was fit to the data, in which x (nm) is the thickness measured from the STEM images, t (hr) is the growth time, m is the power, and A is a multiplicative factor. For the best fit, m=0.26±0.02 and A=11.8±0.8. The power 0.26±0.02 is consistent with ¼, not the parabolic law commonly obtained for Fe oxidation.[151] However, a ¼ power law growth model was reported for the oxidation of Ni at 500 °C,[151] which was modeled assuming that field-induced cation vacancy transport is the rate-limiting process. The same mechanism may control the growth of our films oxidized at 160 °C.

We believe that the formation of the second phase at the Fe_3O_4/TiN interface at 400 °C involves two steps. First, TiN is oxidized to Ti oxides and releases N_2. Second, Fe and O_2 react

with the Ti oxides at the Fe/TiN interface. The oxidation of TiN to Ti oxides is thermally activated, and from the reported activation energy,[152,153] the reaction rate of TiN oxidation at 400 °C is 10^6 times higher than that at 160 °C. TEM done at the Fe/TiN interface annealed in vacuum shows no second phase, which indicates that the oxygen comes from the supplied CO_2/CO gas mixture. In these experiments, we also changed the total gas pressure, but because the CO_2/CO ratio was constant, that does not change the O chemical potential. The only thermodynamic variable that was changed was the temperature.

Conclusions

In conclusion, single-phase Fe_3O_4 thin films were grown by reactive sputtering, but the surface roughness is too large and there are too many APBs, which make such Fe_3O_4 thin film not applicable in MTJs.

Low-defect, smooth Fe_3O_4 thin films suitable for nanoscale spintronic applications were fabricated on Si substrates by CO_2/CO gas selective oxidation using both Ag and TiN buffers. Fe_3O_4 thin films on Ag buffered Si showed improvement of the surface roughness compared to films grown by reactive sputtering. However, Ag diffusion into Fe_3O_4 thin films became a problem. By using TiN buffer, we fabricated the Fe_3O_4 thin film with comparable surface roughness as Fe_3O_4 grown on MgO substrate by MBE. Increasing the oxidation temperature to 400 °C leads to a second phase layer between the TiN and Fe. The formation of the reaction layer is related to the high activation energy of TiN oxidation, so no oxidation occurred at lower temperature. At 160 °C, the Fe_3O_4 thickness follows a ¼ power law in time, providing easy access to nanometer-thick films with low density of anti-phase boundaries.

3.2 Fe_4N and $(Co_xFe_{1-x})_4N$ Thin Film Grown by Reactive Sputtering on a TiN Buffered Si Substrate

3.2.1 Fe_4N Thin film on TiN Buffered Si Substrate

Introduction

As discussed in Chapter 1.4, Fe_4N is suitable for spintronic devices due to its high spin polarization at E_F at RT. Fabrication of Fe_4N thin films requires careful control of kinetic factors such as temperature, N_2 pressure and deposition power.[24] Navio *et al.*[154] investigated the thermal stability of Fe_4N / Cu(001) structure and found that Fe_4N decomposed to Fe_xN at 425 °C. Wu *et al.*[155] studied the thermal stability of Fe_4N nanoparticles and found that these particles were stable in air up to 400 °C and then decomposed and oxidized to Fe_2O_3 at higher temperature. Sunaga *et al.*[69] reported the fabrication of single phase Fe_4N film at RT, but other studies indicated that the Fe_4N phase was only stable at elevated temperatures and other Fe_xN phases were present in the RT fabricated films.[156] Therefore, fabricating single-phase, stable Fe_4N is a challenging task for reactive sputtering.

Thin Film Fabrication

Fe_4N layers with nominal thickness of 45nm were deposited on the TiN / Si(001) structure by DC reactive sputtering at different substrate temperatures (T_s), i.e. RT, 200, 250, 300, 350 and 400 °C under the DC sputtering power of 30, 50 and 80 W. The gas mixture during reactive sputtering was 6 mTorr Ar and 2.5 mTorr N_2, respectively.

Results and Discussions

Optimal growth conditions were explored using XRD. XRD results (acquired by Dr. Hua Xiang, not shown) of Fe_xN thin films showed that only small deposition power (30W) and large N_2 concentration (30%) gave rise to epitaxial growth of Fe_4N thin film on TiN buffered Si (001)

substrate. Substrate temperature (*Ts*) also played an important role: Fe_xN (other iron nitride phases, except Fe_4N) peak still appeared in the XRD results when substrate temperature is 200 °C, but when the substrate temperature increased to 250 and 300 °C, the Fe_xN peaks disappeared and the Fe_4N (002) peak became more pronounced.

The Fe_4N (002) peak disappeared when *Ts* increased to 400 °C, indicating the decomposition of the Fe_4N thin films. This is consistent with Navio *et al.*[154] Post-annealing conditions are also critical for the Fe_4N thin films. When annealing the thin films in a vacuum at 250~400 °C, the Fe_4N thin film decomposed, while on annealing in N_2 atmosphere at the same temperatures, the thin films remained stable.

Therefore, the optimal fabrication conditions for a stable Fe_4N thin film are (1) small deposition power and large N_2 concentration; (2) *Ts* < 400 °C and (3) annealing in N_2 atmosphere.

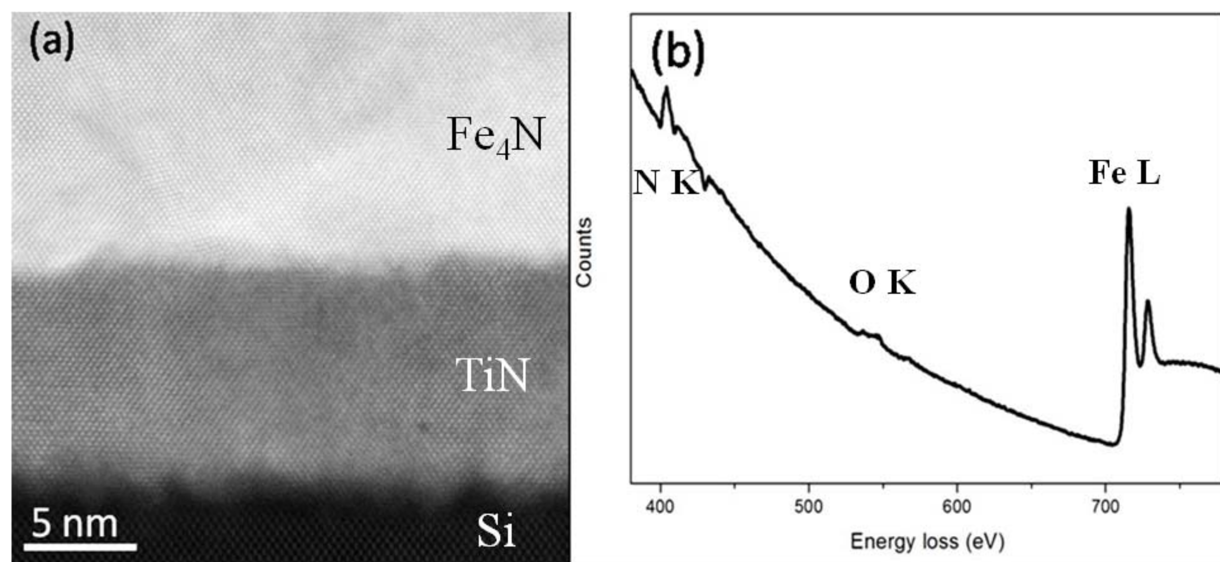

Figure 3.2.1 (a) HRSTEM image of all three layers from bottom to top is Si, TiN and Fe_4N, separately; (b) EELS spectrum on Fe_4N layer.

Epitaxial Fe_4N thin films prepared at T_s=300°C and 30% N_2 are shown in **Figure 3.2.1**. The HRSTEM image along Fe_4N [110] shows a good epitaxial relationship for Si, TiN and Fe_4N

layers in **Figure 3.2.1 (a)**. Surface roughness is 0.41 ± 0.03 nm, suitable for spintronic devices. **Figure 3.2.1 (b)** shows the EELS measurement of Fe_4N thin film, which gives N/Fe atomic ratio 0.2 ± 0.027, indicating that the Fe_4N film is nearly stoichiometric. Magnetization loops show that the magnetization easy axis of Fe_4N on Si (001) substrate followed the Fe easy axis [110] after post annealing the sample in vacuum.

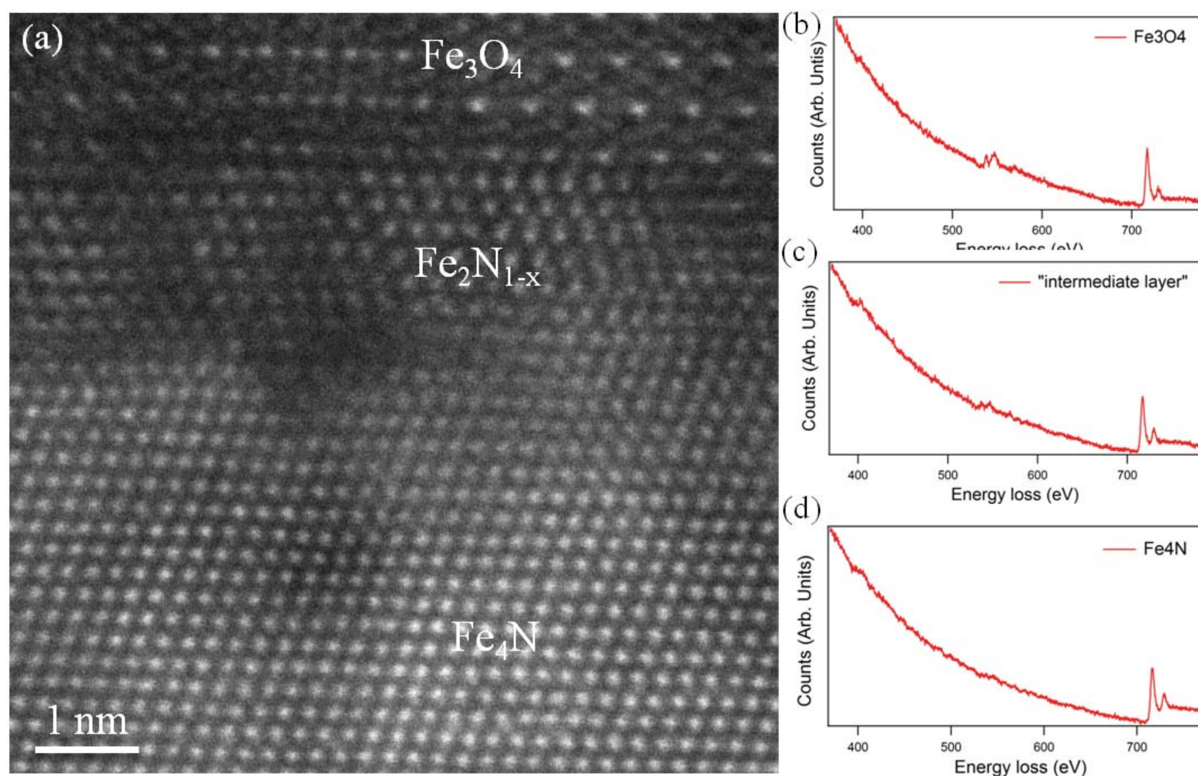

Figure 3.2.2 (a) surface oxidation of Fe_4N. The three layers in the (a) are identified as Fe_3O_4, Fe_2N_{1-x} and Fe_4N. (b) to (d) are EEL spectra for the layers from top to bottom, respectively.

We also investigated the thermal stability of Fe_4N thin films at RT in atmosphere. **Figure 3.2.2 (a)** shows an oxide layer on top of Fe_4N thin film left uncapped Fe_4N in air. The EEL spectrum in **Figure 3.2.2 (b)** is consistent with the O K edge ELNES of a Fe_3O_4 standard. Therefore, the oxidation layer is Fe_3O_4. The phase transformation from Fe_4N to Fe_3O_4 at RT is thermodynamically favorable, since the standard Gibbs formation energies of Fe_4N and Fe_3O_4 are +3.8 kJ/mol and -1015.4 kJ/mol, respectively. At the Fe_4N / Fe_3O_4 interface, there is an

intermediate layer as shown in **Figure 3.2.2 (a)**. The intermediate layer has a larger lattice constant than that of the Fe_4N thin film. EELS quantification based on the spectra in **Figure 3.2.2 (c)** shows that the composition of the intermediate layer is close to ε-Fe_2N_{1-x}, which is consistent with Somers *et al.*[157] However, **Figure 3.2.2 (c)** also shows a small O K edge, indicating that the intermediate layer, ε-Fe_2N_{1-x} has O in its lattice, which may be another reason why the lattice of ε-Fe_2N_{1-x} expanded compared to Fe_4N. **Figure 3.2.2 (d)** shows the EEL spectra from the Fe_4N thin film, in which almost no O is detected. The easy oxidation of Fe_4N thin film suggests that a capping layer such as Al is essential to keep Fe_4N stable at room temperature under in atmosphere atm.

3.2.2 $(Co_xFe_{1-x})_4N$ Thin Film on TiN Buffered Si Substrate

Introduction

Co_4N is also a ferromagnetic material with the same fcc structure as Fe_4N.[158,159] Similar to Fe_4N, Co_4N has the minority spin electron dominant conduction current, which was recently predicted to be nearly half metallic.[158,159] The spin polarization of Co_4N at the Fermi level is predicted to be -0.875, which is much larger than that of Fe_4N (-0.675), suggesting that Co_4N could be useful for spintronics applications. However, Matsuoka *et al.*[160] found that instead of Co_4N, a mixed phase of Co nitride including Co_2N and Co_3N forms by reactively sputtering Co with N_2. Other approaches like heating CoN precursor up to 500 °C yielded a mixture of different CoN_x phases, but without a trace of Co_4N.[161] Ito *et al.*[162] reported the growth of Co_4N thin films on $SrTiO_3$ substrates by MBE using NH_3 plasma.

Adjusting the relative composition of Co_xFe_{1-x} may lead us to the ordered Co_3FeN phase with fully spin polarized electrons at Fermi level or might create stable films with higher spin polarization than Fe_4N.[68] Therefore, we attempted to fabricate $(Co_xFe_{1-x})_4N$ films on TiN

buffered Si(001) substrates by dual target reactive co-sputtering under similar conditions to Chapter 3.2.1. Composition films were fabricated, but single-phase $(Co_xFe_{1-x})_4N$ was not achieved. We found that iron nitrides are much more likely to form than cobalt nitrides, which may also suggest the possible reason for the difficulty of fabricating pure phase Co_4N thin film.

Thin Film Fabrication

Bilayers with the structure of Si (001) / TiN / $(Co_xFe_{1-x})_4N$ were grown in the same sputtering chamber as in Chapter 3.2.1. After the substrate was cooled to RT, the $(Co_xFe_{1-x})_4N$ layer was deposited on the TiN/Si(001) structure by co-sputtering from Fe and Co targets simultaneously at substrate temperature (T_s) of 300 °C. During the reactive sputtering process, the deposition power for Fe target was kept at DC 55 W, but Co target was rf sputtered at different powers, i.e. 20, 30, 45, 60, 80, 120, 200, 250 and 300 W. The gas mixture for $(Co_xFe_{1-x})_4N$ layer deposition is 6 mTorr Ar mixed with 2.5 mTorr N_2.

Results and Discussions

We used XRD to test whether we grew $(Co_xFe_{1-x})_4N$ phase. However, with Co sputtering power 20 W, we found only Fe_4N peaks at ~ 23.4º in XRD, and no trace of Co nitrides. **Figure 3.2.3** shows STEM investigations of such a thin film. Without a capping layer on top of the thin film, an oxidation layer formed as shown in **Figure 3.2.3** (a). **Figure 3.2.3** (b) is a higher magnification view of the same layer. The oxidation layer has a similar structure as the one on top of Fe_4N thin film shown in **Figure 3.2.2** (a). The EEL spectrum of the surface oxidation layer in **Figure 3.2.3(c)** also has a pre peak in O K edge and no Co L edge, which means that the surface oxidation is completely Fe oxide. In **Figure 3.2.3** (d), the EEL spectrum shows that only Fe and N edges are presented, which might be due to the small Co sputtering power.

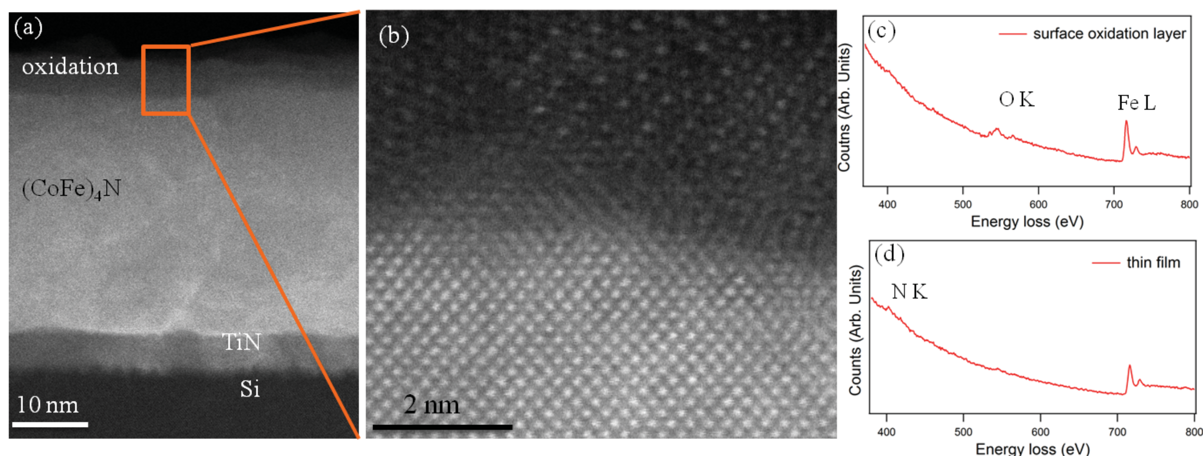

Figure 3.2.3 $(Co_xFe_{1-x})_4N$ thin film with Co rf deposition power 20 W. (a) A low magnification STEM image of the multilayer thin film. (b) A HRSTEM image of the interfaces between surface oxidation layer and the thin film. (c) and (d) are EEL spectra from surface oxidation layer and thin film, respectively.

With increasing Co sputtering power, XRD showed that the peaks of Fe_4N disappeared and a peak at 50° emerged. This peak can be attributed to either Co_4N or fcc Co (002) because of the close lattice parameter between these two materials. High resolution XRD found that 2θ is 51.73°, a little larger than the 2θ=51.52° of bulk fcc Co(002) peak, which suggests the epitaxial fcc Co phase with out-of-plane compressive stress rather than the possible Co_4N phase formation.

Figure 3.2.4 shows the thin films deposited with Co sputtering power 300 W. **Figure 3.2.4** (a) shows the low magnification STEM image of the thin film. The surface still has a thin oxidized layer, but it is smoother than the thin film with Co depositing power 20 W shown in **Figure 3.2.3** (a). A HRSTEM image in **Figure 3.2.4** (b) shows the structures of the surface oxidation layer, which is different from what is shown in **Figure 3.2.3** (b). In **Figure 3.2.4** (c), the EEL spectrum on the surface oxidation layer reveals that the oxidation layer contains Co and Fe with a Fe/Co ratio 0.52 ± 0.12. The EEL spectrum on the thin film in **Figure 3.2.4** (d) shows only Co L edges with Fe/Co ratio 0.12 ± 0.01 and no N K edge. We concluded that the peak

shown in XRD around 50º is from fcc Co instead of Co_4N. From the results shown in **Figure 3.2.3** and **3.2.4**, iron nitrides form more easily than cobalt nitrides, which might be the reason why the Co_4N thin film is difficult to fabricate.

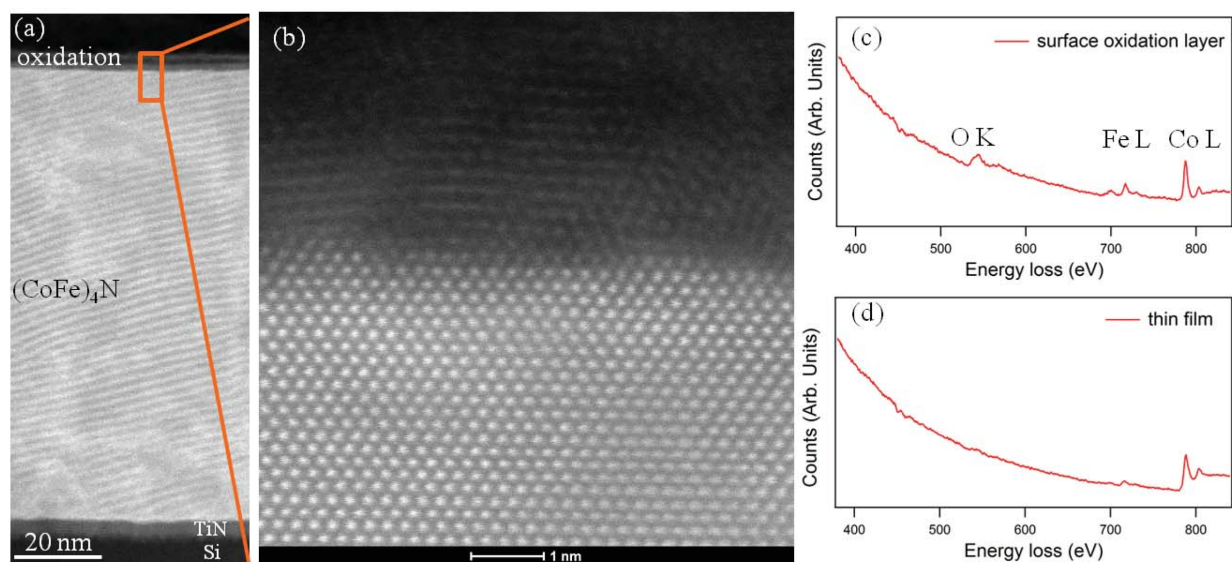

Figure 3.2.4 $(Co_xFe_{1-x})_4N$ thin film with Co rf deposition power 300 W. (a) A low magnification STEM image of the multilayer thin film. (b) A HRSTEM image of the interfaces between surface oxidation layer and the thin film. (c) and (d) are EEL spectra from surface oxidation layer and thin film, respectively.

Conclusions

We have fabricated epitaxial, nearly stoichiometric Fe_4N thin film on TiN buffered Si (001) substrate by reactive sputtering confirmed by HRSTEM and STEM EELS. We have explored the optimal growth conditions that lead to form a stable Fe_4N thin film, including small deposition power, large N_2 concentration, $T_s < 400$ °C, N_2 atmosphere annealing. Fe_3O_4 has formed on top of Fe_4N thin film if without a capping layer. The formation of Fe_3O_4 was thermodynamically favorable. Our results suggest that (1) a proper capping layer is essential to prevent surface oxidation on Fe_4N thin films; (2) integrating Fe_4N into a MTJ can be problematic due to its easy-oxidation nature.

$(Co_xFe_{1-x})_4N$ film films with increasing Co content were prepared on TiN buffered Si(001)

substrates. When the Co content is low, the thin film mainly consists of Fe_4N, while with the increasing Co rf sputtering powers, fcc Co is the main phase of the thin films.

Chapter 4 Ferromagnet/Oxide Interfaces in Magnetic Tunnel Junctions with AlO_x Tunnel Barriers

4.1 Formation of Fe_3O_4 at $CoFe/AlO_x$ Interfaces in a Nominally Symmetric Ag Buffered MTJ

Introduction

Most of the $CoFe/AlO_x/CoFe$ MTJs exhibit positive TMR due to the positive SP across $CoFe/AlO_x$ interfaces.[5,54,163-167] However, Du *et al.* observed inverse TMR in a $CoFe/AlO_x/CoFe$ junction in a MTJ with over-oxidized AlO_x tunnel barrier.[54] They speculated that Fe_3O_4 formed at the interface, but did not present any data supporting this hypothesis. Yang *et al.*[167] showed that XPS exhibited Fe^{3+} and Fe^{2+} peaks typical of Fe_3O_4 from an over-oxidized $CoFe/AlO_x$ interface, but their results were from a half junction, so they could not be correlated directly to TMR properties.

In order to investigate the local structural and composition information in full junctions, we applied Cs-corrected HRSTEM and STEM EEL SI to both interfaces of a $CoFe/AlO_x$ MTJ. We compared three types of junctions: MTJ (1): A $CoFe/AlO_x/CoFe$ MTJ deposited on a Ag buffer layer on Si, which exhibits inverse TMR after field cooling; MTJ (2): the same MTJ before field cooling, which exhibits normal TMR; and MTJ (3): A $CoFe/AlO_x/CoFe$ MTJ deposited on a TiN buffer, which exhibits normal TMR, both before and after field cooling. Based on the O K-edge ELNES[147] and the Fe $L_{2,3}$ edge core level shifts,[148] both $CoFe/AlO_x$ interfaces in the inverse TMR junctions have some regions covered with Fe_3O_4. EELS SI shows that the Fe_3O_4 is not a continuous film, and as a result, it is not visible as a distinct layer in the HRSTEM images. We find no Fe_3O_4 in the normal TMR junctions, although some other Fe

oxides are present, so we ascribe the inverse TMR to negative spin polarized tunneling from Fe_3O_4.

MTJ Fabrication and STEM Experiment

The MTJ multilayer stack was fabricated by Dr. Hua Xiang. The normal TMR junctions consisted of Si (001)/TiN (200) (9 nm)/$Co_{75}Fe_{25}$ bcc (200) (20 nm)/ AlO_x tunnel barrier (1.7~2 nm)/ $Co_{75}Fe_{25}$ (5 nm) / $Ir_{22}Mn_{78}$ (20 nm)/Ag (100 nm). The bottom electrode was epitaxial. The AlO_x tunnel barrier was formed by rf sputtering of 1.2 nm of Al metal followed by *in situ* rf plasma oxidation in 100 mTorr of oxygen. The MTJ sheet films were patterned into round junctions with radii ranging from 55 to 95 *u*m by photolithography, then Ar ion milling. The inverse TMR samples have a similar structure, but with an Ag bottom buffer layer: Si (001)/Ag fcc (200) (35 nm)/$Co_{75}Fe_{25}$ bcc (200) (20 nm)/ AlO_x (1.7~ 2 nm)/ $Co_{75}Fe_{25}$ (5 nm) / $Ir_{22}Mn_{78}$ (20 nm)/Ag (100 nm). Transport measurements were carried out by Dr. Hua Xiang using the standard dc four-probe method. The TMR curves and the bias voltage dependences of the TMR ratio were measured at room temperature. The annealing conditions for normal and inverse TMR samples were slightly different: for the annealed inverse TMR junctions, the annealing conditions were 300 °C for 3 min in air; for normal TMR junctions, we annealed them under 250 °C for 2 min. However, the annealing conditions made no substantial difference for the measurements. After annealing, two types of junctions were both cooled down under a 1000 Oe magnetic field.

The EELS conditions were different from what were described in Chapter 3.4. The probe convergence angle was 24.5 mrad, and the probe current was ~100 pA (spotsize 6), resulting in spatial resolution of ~0.1 nm. The EELS SIs were taken in EFSTEM mode with camera length CL = 248mm, convergence angle α = 17.5 mrad, probe current 71 pA, spatial resolution ~0.1

nm, and EELS collection angle $\beta = 52$ mrad. The smaller convergence angle was used to reduce the current, which is necessary to avoid beam damage to the specimens. It also generates a more compact probe for microanalysis. The SIs were all processed by weighted PCA for de-noising.[120] In this experiment, 30 principle components were used to maintain the energy loss near edge fine structures (ELNES). This relatively large number of principle components was required due to correlated noise in the spectrum image from imperfect gain normalization or dark subtraction.

Composition profiles were extracted from the corresponding EEL SIs and then integrated horizontally along the junctions. Quantifications were calculated without PCA denoising. We assumed the horizontal compositions were uniform for all the junctions, which is true for a SI with a small vertical drift rate. The reference for the measurement of Fe $L_{2,3}$ core level shifts is an artifact peak in the EELS around 700 eV, which is due to secondary emission of the Titan Schottky emission gun. This artifact peak is materials independent, but captures fluctuations in the high voltage and the lab EM fields, so it provides us a reliable reference to determine the Fe $L_{2,3}$ core level shifts.

Results and Discussions

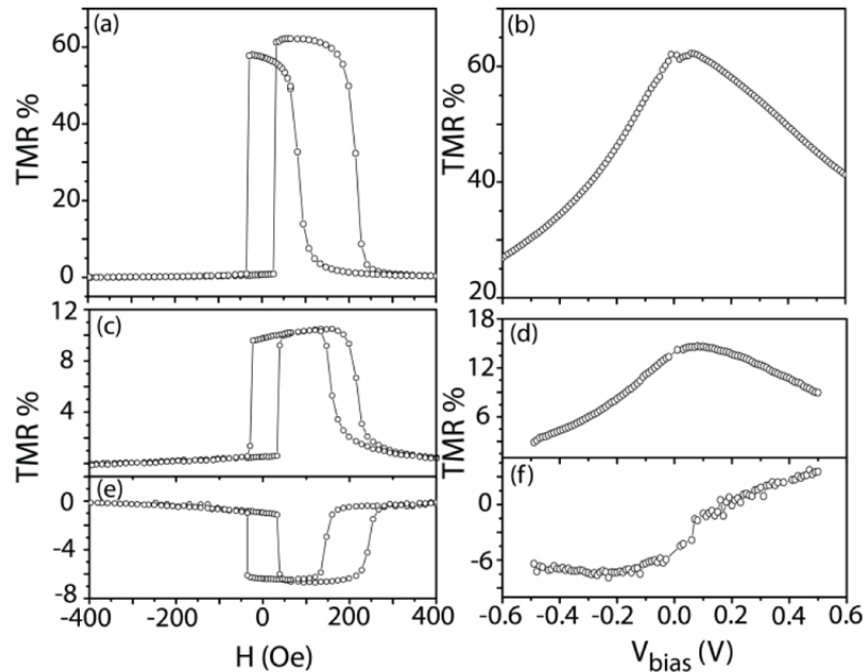

Figure 4.1.1 TMR loops and bias dependence for (a) and (b), a TiN-buffered, 250 °C field-cooled junction, (c) and (d), an as-prepared Ag-buffered junction, and (e) and (f), a Ag-buffered, 300 °C field-cooled junction. Only (e) and (f) show inverse TMR.

Figure 4.1.1 shows TMR loops and bias dependences for the TiN-buffered, 250 °C field-cooled junction (a and b), the as-prepared, Ag-buffered junction (c and d), and the Ag-buffered, 300 °C field-cooled junction (e and f). The TiN-buffered junction shows relatively high normal TMR signal (65%) with symmetric bias dependence. The as-deposited, Ag-buffered junction also shows normal TMR with symmetric bias dependence, although the TMR signal is lower, about 11% at room temperature under 0.035 V bias voltage. Only the Ag-buffered, field-cooled junction shows inverse TMR. Its TMR is about -7% under -0.3 V bias voltage, and the TMR bias dependence is asymmetric.

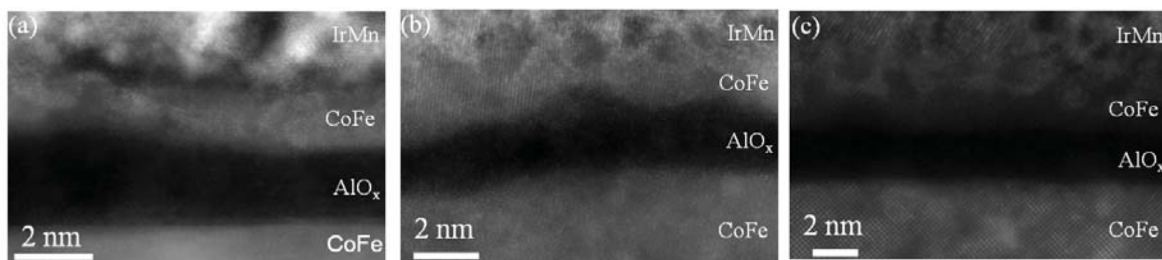

Figure 4.1.2 HRSTEM images for three different junctions: (a) a TiN-buffered, 250 ℃ field-cooled normal TMR junction, (b) an as prepared Ag-buffered normal TMR junction, and (c), a Ag-buffered, 300 ℃ field-cooled inverse TMR junction. No obvious extra layers are present in any of the junctions.

Figure 4.1.2 shows HRSTEM images of structures of all three junctions. Each image shows, from top to bottom, the IrMn, CoFe, AlO_x, and CoFe layers. The Ag or TiN buffer layer and the Si substrate are not shown. There are no obvious second-phase layers visible in these images. At a flat interface, continuous layers as thin as a monolayer are visible using this technique.[98,168,169] The CoFe/AlO_x interfaces are somewhat rough,[170] but even the nearly atomically flat local regions in the images have no second phase. However, these images view the sample in two dimensional projection along the beam direction, so small islands of a second phase that overlap with a more strongly scattering matrix can be difficult to image. **Figures 4.1.3, 4.1.4, and 4.1.5** show EEL SIs collected from the regions of the three junctions shown in **Figure 4.1.2**. Each SI was processed for the Co, Fe, Mn, and O composition. (Al was not included because it does not have an ionization edge within the 450 to 850 eV energy range of the EEL spectra.) We also used the fine structure on the O and Fe edges in the EEL SIs to determine the Fe chemical state and Fe-O phase.[148,171]

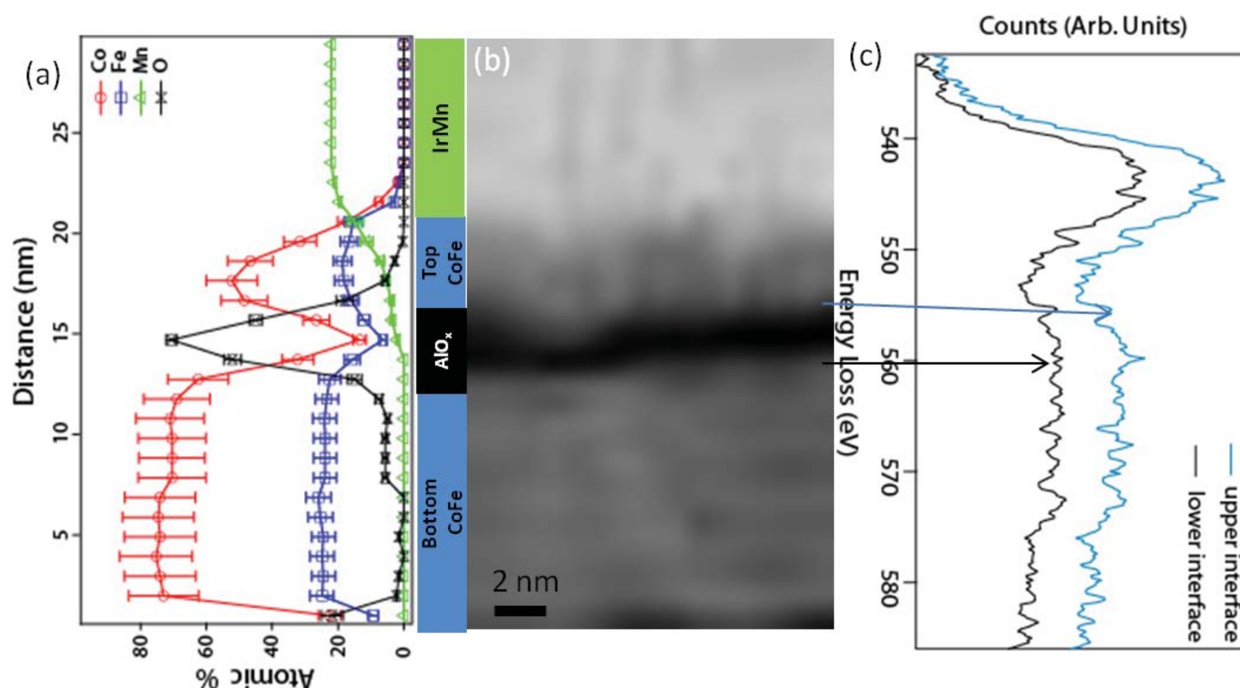

Figure 4.1.3 EELS results on normal TMR junctions: (a) the composition profile extracted from EEL SI (b) simultaneous ADF image acquired with the EEL SI (c) Typical O K edges for the upper and lower interfaces. The arrows indicate the positions where the spectra come from.

Figure 4.1.3 shows the EELS SI of the TiN-buffered normal TMR junction, acquired with 1 nm pixels. The center panel, **Figure 4.1.3 (b)**, is the HAADF signal acquired at the same time as the EEL spectra. Compared to the HAADF images in **Figure 4.1.2**, the HAADF map is acquired at much longer dwell time per pixel and much sparser pixel sampling. The left of **Figure 4.1.3 (b)** identifies the layers in the device, which are, from bottom to top, the IrMn, the top CoFe electrode, the AlO_x, and the bottom (near substrate) CoFe electrode. In the integrated composition profiles shown in **Figure 4.1.3 (a)**, the O concentration peaks in the tunnel barrier, and there is also a small amount of O in the bottom CoFe electrode. This low O concentration may be due to surface oxidation of the thin TEM samples, perhaps exacerbated by the plasma clean. Mn has diffused through the top CoFe but was stopped by the barrier layer, consistent with previous results of Samant *et al*.[172] **Figure 4.1.3 (c)** shows two O K edge EEL spectra extracted

from the top and bottom CoFe/AlO_x interfaces at the positions indicated by the arrows (each comes from one pixel in the SI). The two spectra have the same near-edge structure.

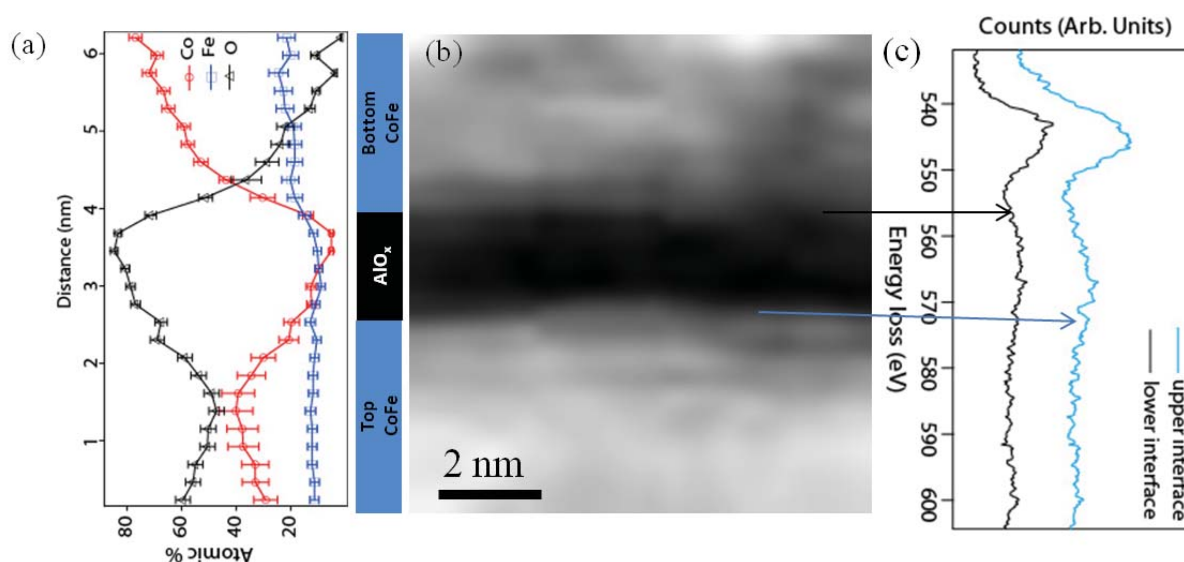

Figure 4.1.4 EELS results on an as prepared inverse TMR junctions: (a) the composition profile extracted from EEL SI. (b) The simultaneous HAADF images acquired with the EEL SI (c) the O K edges extracted from both upper and lower interfaces. The arrows indicated the positions where the spectrums come from.

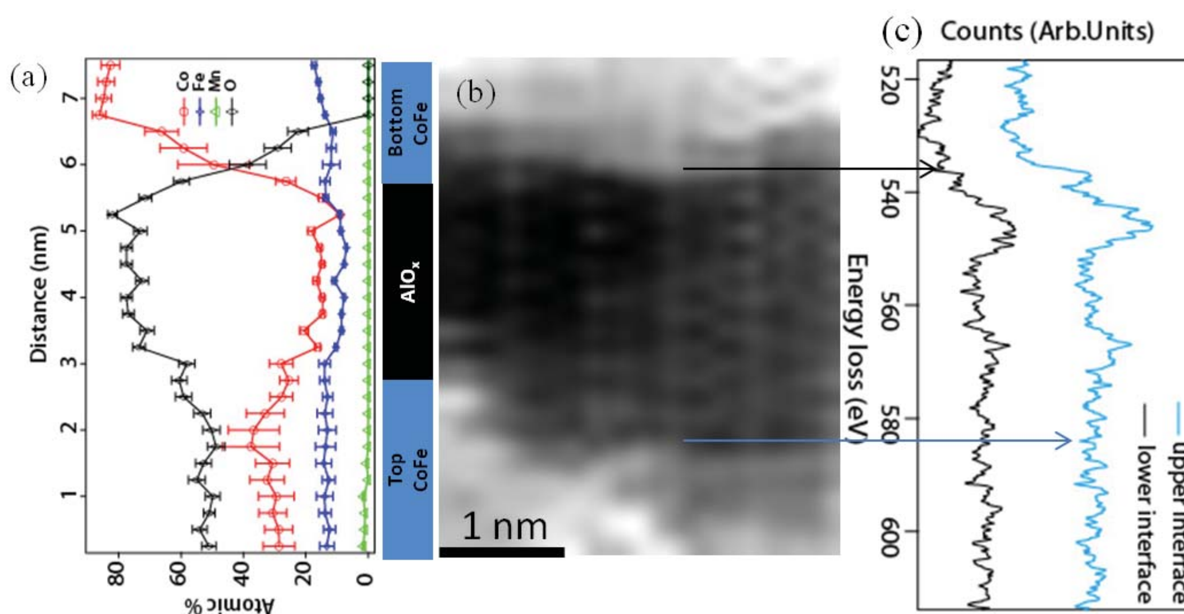

Figure 4.1.5 EELS results on annealed inverse TMR sample: (a) composition profile extracted based on EEL SIs (b) the simultaneous HAADF images acquired with EEL SI (c) the extracted O K edges from both upper and lower interfaces, the arrows indicate the position where the spectra come from

Figure 4.1.4 is an EELS SI of an as-deposited Ag-buffered normal TMR junction. The composition profiles in **Figure 4.1.4 (a)** show that the O concentration is high in the upper electrode. This concentration is too high for purely surface oxidation. However, the EEL spectra in **Figure 4.1.4** (c) from the two interfaces are the same.

Figure 4.1.5 is an EELS SI of an Ag-buffered, field-cooled, inverse TMR junction acquired with 0.25 nm pixels. The simultaneous HAADF image is shown in **Figure 4.1.5 (b)**. There are periodic dots visible in the barrier layer region, which may be caused by carbon contamination on the sample.[173] **Figure 4.1.5 (a)** shows the integrated composition profiles. There is a significant amount of O in the top CoFe layer, which is too large for surface oxidation. The O concentration decreases sharply in the bottom CoFe electrode. **Figure 4.1.5 (c)** shows two O K edge EEL spectra extracted from the top and bottom CoFe/AlO_x interfaces at the positions indicated by the arrows. The top interface spectrum has a strong pre-peak before the main O K edge. The bottom interface spectrum does not, like the spectra for MTJ (1) and MTJ (2) shown in **Figures 4.1.3 (c)** and **4.1.4 (c)**.

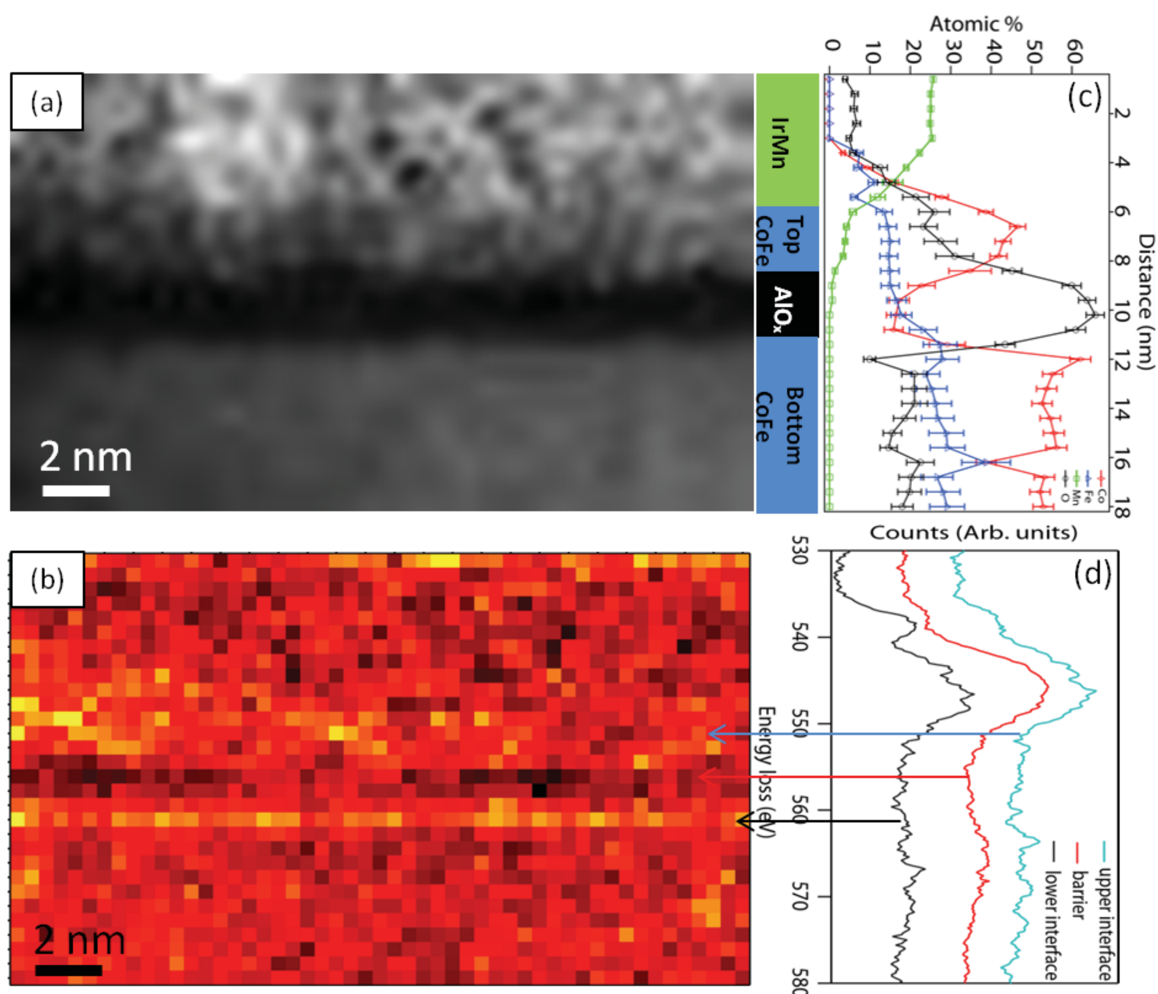

Figure 4.1.6 EELS results on annealed inverse TMR junctions: (a) the simultaneous HAADF images acquired with EEL SI (b) the mapping of the intensity of pre- peak of O K edge (c) the composition profile extracted from EEL SI (d) the extracted O K edges for upper interface, barrier and lower interface. The arrows indicate the positions where these spectrums come from.

Figure 4.1.6 is an EELS SI from a different area of the same inverse TMR junction, acquired with 0.6 nm pixels. The composition profile in **Figure 4.1.6 (c)** is similar to the composition profile on the TiN-buffered normal TMR junction in **Figure 4.1.4 (a)**, although with more O in the CoFe layers. Unlike **Figure 4.1.5 (c)**, the O K edge ELNES for the two interfaces in **Figure 4.1.6 (d)** show a pre-peak at the bottom interface and not at the top. **Figure 4.1.6 (c)** is a map of the O K edge pre-peak intensity, integrated from 528.4 to 529 eV. The color scale is normalized to the highest intensity of O K edge pre peak. The pre-peak intensity map shows a

thin (one pixel wide), uniform band at the bottom interface, and low average intensity at the top interface with a few hot spots due to noise. As in **Figure 4.1.5 (d)**, the color is normalized to the highest intensity of O K edge pre peak. **Figure 4.1.6 (d)** also shows an O K-edge from the AlO_x barrier, which does not have a pre-peak.

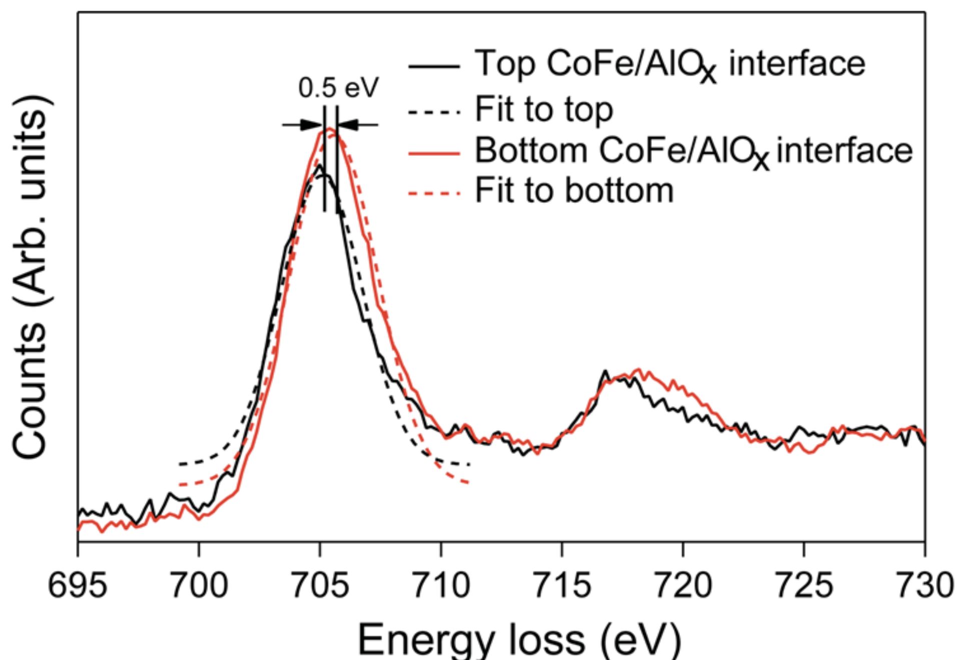

Figure 4.1.7 Fe L edge core level shift between upper and lower CoFe/AlOx interfaces

Figure 4.1.7 shows the Fe $L_{2,3}$ edges from the same two positions in the inverse TMR SI in **Figure 4.1.6** as the O K-edge spectra in **Figure 4.1.6 (d)**. The black line is the spectrum from the top interface in **Figure 4.1.6 (d)** that does not have the O K edge pre-peak. The red line is from bottom interface spectrum that does have the O K edge ELNES pre-peak. The dashed lines are the Gaussian fits to the Fe L_2 white lines, which provide sub-channel measurements of the peak position. The peak for the bottom interface has shifted approximately 0.5 eV higher in energy compared to the peak from the top interface. Similar analysis of Fe $L_{2,3}$ edges from the inverse TMR junction spectra in **Figure 4.1.5 (c)** shows a core level shift of 0.3 eV. No shift or other changes in fine structure are found for any of the Co $L_{2,3}$ edges in any SI.

Annealing and field cooling created inverse TMR for nominally symmetric Ag/CoFe/AlO_x/CoFe junctions which should, in principle, show positive TMR.[174] Based on EEL SIs and composition profiles from all three types of junctions, we believe that the inverse TMR is due to a Fe_3O_4 reaction layer at the interfaces between CoFe and AlO_x. The reaction layer is not always at the same interface, is not always the same thickness, and is discontinuous. There are also thin FeO layers, which may reduce the TMR.

We identified the Fe-O layers primarily based on the O K-edge pre-peak[171] and the Fe $L_{2,3}$ core level shift.[148] The O K edge corresponds to O 1*s* and 2*p* transitions. The pre-peak arises from unoccupied O 2*p* states that are hybridized with Fe 3*d* orbitals. O bonded to Al, on the other hand, has no prepeak.[175] Therefore, the regions with a strong pre-peak in **Figure 4.1.5 (d) and 4.1.6 (b)** are regions with Fe-O bonds. The absence of the pre-peak in **Figure 4.1.3 (c)** and **4.1.4 (c)** (and the in rest of those SIs) indicates no Fe-O bonding. The shape, energy, and relative intensity of the pre-peak depends on the Fe-O phase.[171] The separation of the pre-peak maximum and the main peak maximum is a convenient metric. Colliex *et al.* have reported that this separation is 10.7 ± 0.2 eV or Fe_3O_4, 11.0 ± 0.2 eV for α-Fe_2O_3, and 9.0 ± 0.2 eV for FeO.[171] In **Figure 4.1.7**, the peak separation is 10 eV, which is closest to the value for Fe_3O_4. However, the shape of O K edge in this Fe_3O_4 thin layer is consistent with that measured in a Fe_3O_4 standard under similar experimental conditions. More details will be discussed in Chapter 6.

The Fe $L_{2,3}$ edges correspond to an electron transition from Fe 2*p* states to empty 3*d* states. If the Fe is oxidized, some of the 3*d* electrons are transferred to the oxygen, so there are more empty 3*d* states on the Fe, which will shift the energy of the L_2 peak. The direction of shift is a more complicated problem.[106] As shown in **Figure 4.1.7**, the Fe L_2 edge from the top

electrode in the SI in **Figure 5.1.6** is 0.5 eV higher in energy than the L_2 edge from the bottom electrode. From the composition profiles in **Figure 5.1.6 (a)**, we know that both electrodes contain some Fe-O phase. The +0.5 eV shift is consistent with the difference in position between FeO and Fe_3O_4.[148] FeO does not have a strongly separated O K-edge prepeak. Instead, there is a small shoulder on the low energy side of the main peak.[171] The O K-edge from the top electrode in **Figure 4.1.6** may show such a shoulder, although it is not significantly above the noise in the spectrum. The core level peak shift of the Fe L_2 edge for the inverse TMR junction SI in **Figure 4.1.5** is +0.3 eV, which is consistent with the shift from Fe_3O_4 to Fe.[148]

The lack of shift in the Co $L_{2,3}$ edge means that the Co was not oxidized. The Gibbs free energy of formation ΔG of Fe_3O_4 is much lower than ΔG of CoO at the 300 °C temperature used for field cooling, so the reaction rate to oxidize Fe is much larger than for Co. The Fe_3O_4 layers are too thin for the rejected Co to create a large enough change in the underlying CoFe electrode composition to be detected in the EELS maps, as in **Figure 4.1.5 (a)** or **Figure 4.1.6 (a)**. Along similar lines, in CoFe/AlO_x/FeO_x/CoFe MTJs, Zhang *et al.* observed by Rutherford backscattering spectrometry (RBS) no incorporation of Co into the FeO_x at temperatures up to 400 °C, which is high enough to decompose the FeO_x.[176]

The thickness of the Fe_3O_4 layer of the upper electrode varies from 1.5 nm to 2 nm, although we have not captured the top edge of the layer due to the limited area of the SI. In **Figure 4.1.6**, the Fe_3O_4 at the bottom interface is only 0.6 nm (1 pixel) thick. That may or may not be sufficient Fe_3O_4 to exhibit negative spin polarization. Lu *et al.*[134] reported that epitaxial Fe_3O_4 films on GaAs (100) thicker than 1.6 nm have bulk-like magnetic properties, which suggests they would also have negative spin polarization. Thinner films, <1 nm, did not have bulk-like magnetic properties. However, very thin films may be discontinuous, or they may

incorporate such a high density of crystallographic defects such as anti-phase boundaries that they do not exhibit bulk-like magnetic properties,[22,143,177] even though they may still have interface-dominated negative spin polarization.

Our results indicate that the Fe-O layers are not continuous. They do not appear in the HRSTEM images in **Figure 4.1.2**, and the Fe/O ratio for the Fe_3O_4 reaction layer in **Figure 4.1.5** is 0.26±0.04 from the EELS quantification, well below the 0.75 of Fe_3O_4. The low Fe/O ratio indicates that through the thickness of the sample, we were averaging some thickness of Fe_3O_4 with some phase with lower O, possibly pure Fe. This might also explain the smaller O pre-peak / main peak energy difference we observed compared to the pure phases studied by Colliex *et al.*[171] The Fe_3O_4 pre-peak sits on a sloping pre-edge background of the pure Fe spectrum, which slightly shifts the energies of the peaks. There is some evidence of islanding in the O prepeak maps in **Figure 4.1.5 (d)**, which grows more intense towards the bottom and at the top electrode of **Figure 4.1.6 (d)** on the left-hand side.

We observed inverse TMR only in Ag-buffered samples after annealing and field cooling. O has a relatively high solubility in Ag (about 2.24 c.c./g at 300 °C),[178] especially, so we speculate that the annealing released the O from the Ag, which diffused to the tunnel barrier, and then reacted to form Fe_3O_4. We have not identified the source of O for the Fe_3O_4 in the top electrode, although high O in either electrode is correlated to the formation of Fe_3O_4, as shown by comparing the O profiles from a normal TMR junction in **Figure 4.1.4** (a) to the inverse TMR junction in **Figure 4.1.5** (a).

Only a junction with Fe_3O_4 on one side of the AlO_x and CoFe on the other side will exhibit inverse TMR. We found that the Fe_3O_4 can occur in either electrode and that other, non-ferromagnetic Fe-O phases may also be present. This may explain the low negative TMR (-7%)

exhibited by our junctions. It also significantly complicates efforts to explain the asymmetric bias dependence in **Figure 4.1.1** (f), since our junctions are effectively a combination of Fe_3O_4/AlO_x/CoFe inverse TMR junctions and CoFe/AlO_x/CoFe normal TMR junctions. In general, TMR bias dependence in MTJs is a complicated problem, depending on factors such as the increase in the conductance with bias, the excitation of magnons, and the energy dependence of the spin polarization due to band structure effects.[179]

Although these MTJs are not optimized for the inverse TMR, they represent a particularly simple processing path to achieving inverse TMR, just by annealing. This may point to an easier way to control inverse TMR by manipulating the O in Ag using the annealing time and temperature. Other materials as buffer or capping layers might also be useful as oxygen reservoirs, like Ta, Ti, Zr and Hf, which also have high O solubility.[180,181]

Conclusions

We found inverse TMR in a nominally symmetric, annealed, Ag buffered CoFe/AlO_x/CoFe junction. Aberration-corrected HRSTEM and STEM EELS were used to characterize the buried interfaces. In the inverse TMR junctions, we found a thin, discontinuous Fe_3O_4 layer at the top and bottom electrode/tunnel barrier interfaces by EELS SI. We believe that the Fe_3O_4 at the interfaces is the reason that the sign of TMR was reversed after annealing. These results may point to a simple processing route to achieving inverse TMR using well-established materials.

4.2 Fe_3O_4 Reaction Layer at Fe_4N/AlO_x Interface in a $Fe_4N/AlO_x/Fe$ MTJ

Introduction

As discussed in Chapter 1, Fe_4N with -100% spin polarization is promising as a ferromagnetic electrode in spintronic devices such as MTJs.[64] Therefore, MTJs with Fe_4N as ferromagnetic electrodes should show high TMR. Komasaki *et al.*[57] reported a -75% TMR at RT in a Fe_4N/MgO/CoFeB MTJ after structural optimization. In their experiment, an ultrathin Mg (0.4 nm) was inserted at Fe_4N/MgO interface to prevent the interfacial reaction between Fe_4N and oxygen during depositing MgO by rf sputtering. However, even using highly epitaxial Fe_4N electrode and controlling the oxidation at the Fe_4N/MgO interface, the absolute value of TMR is still not high compared to MTJs with CoFeB electrodes.[19] The reason for the low TMR in Fe_4N based MTJs is still not clear. Since Fe_4N is metastable and easily oxidized to Fe_3O_4 driven by thermodynamics as shown in Chapter 4, substantial interfacial oxidation might have happened even with the Mg protecting layer. The interfacial oxidation could substantially alter the performance of the MTJs.[89]

We used HRSTEM and STEM EELS to investigate the Fe_4N/AlO_x interface in a $Fe_4N/AlO_x/Fe$ MTJ before and after field cooling. Before field cooling, the TMR is positive (3.3% at 0.02 V). Afterwards, it is negative (-5.7 V at 0.02 V). We found that the bottom epitaxial Fe_4N electrode has been partially oxidized to Fe_3O_4 at the Fe_4N/AlO_x interface after field cooling. The formation of Fe_3O_4 explains the abnormal bias dependence found in this MTJ. A redistribution of oxygen at the Fe_4N /AlO_x interface was observed before and after field cooling, which helps explain the sign switching of the TMR in this junction.

MTJ Fabrications

MTJs with the structure Si(001)/TiN(10)/Fe_4N(20)/AlO_x(1.5)/Fe(6)/IrMn(40)/ Ag(100)

(numbers in parentheses are layer thickness in nm) were fabricated by dc and rf sputtering in a vacuum chamber with base vacuum better than 1×10^{-7} Torr. The bottom Fe_4N layer was deposited onto the TiN buffer at 300 ºC in an Ar and N_2 gas mixture, as described in detail elsewhere.[24] The resulting layers are epitaxial with the crystallographic relationship Si(004)[100]//TiN(002)[100]//Fe_4N(002)[100].[24] The AlO_x tunnel barrier was formed by rf sputtering of a 1.2 nm Al pre-metal followed by *in-situ* rf plasma oxidation in 100 mTorr oxygen. The rest of the layers were deposited at RT.

The sample was patterned by photolithography into discs with radii from 55 to 95 μm and then ion-milled in an Auger electron spectrometer. Field cooling was done in air by keeping the as-prepared sample at 210 or 250 ºC for 2 min and then cooling it to RT under a 1000 Oe magnetic field. Transport properties and the bias voltage dependence of the TMR ratio were measured using the standard dc four-probe method at RT. For consistency, all transport results are reported for devices 80 μm in radius. Characterizations done by STEM and STEM EELS are described in detail in Chapter 2.4.

Results and Discussions

Figure 4.2.1 shows that the sign of TMR has changed after field cooling. Positive TMR (3.3% under 0.02 V bias) is shown for the MTJ before the field cooling, which is abnormal for a MTJ with one ferromagnetic electrode having negative SP and the other electrode (Fe) with positive SP. However, after field cooling, we have a small negative TMR instead (-5.7% under 0.02 V bias).

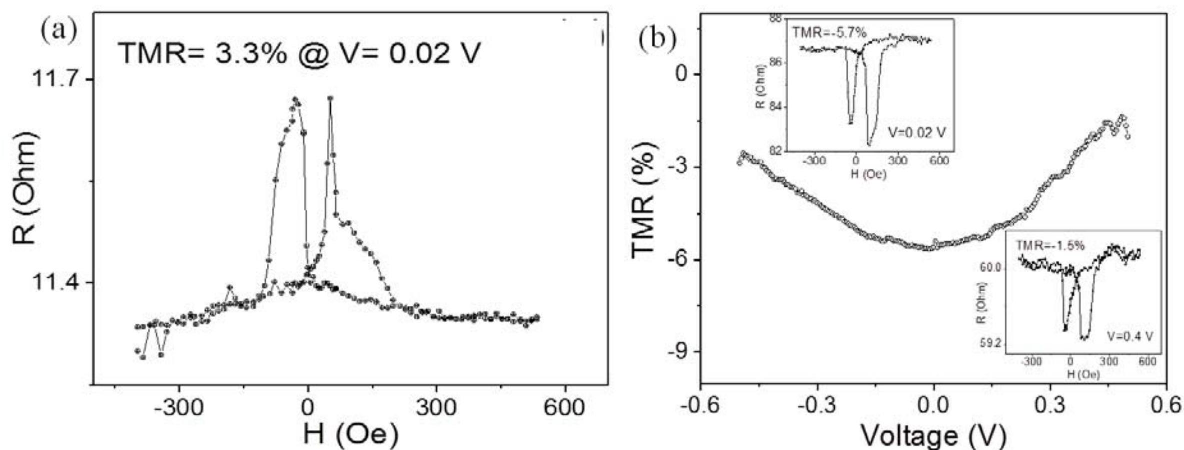

Figure 4.2.1 TMR of the $Fe_4N/AlO_x/Fe$ MTJs before and after field cooling as shown in (a) and (b), respectively. Data acquired by Dr. Hua Xiang.

Figure 4.2.2 (a) shows a HRSTEM image of a reaction layer at Fe_4N/AlO_x interface in the MTJ before field cooling. The EEL spectrum in **Figure 4.2.2** (b) shows a pre peak feature of the O K edge, which is consistent with the formation of a FeO_x compound.[171] An enlarged view of the pre peak feature is shown in the energy range near the O K edge in **Figure 4.2.2** (c). N signal was not observed in the EEL spectrum. We have conducted a quantitative analysis on the EELS results to resolve the composition of the reaction layer. The qualitative peak shape and peak splitting are consistent with the formation of Fe_3O_4. The quantification on the reaction layer, however, shows that the Fe/O ratio is 1.1±0.1, indicating that the reaction layer is a mixed phase of FeO and Fe_3O_4.

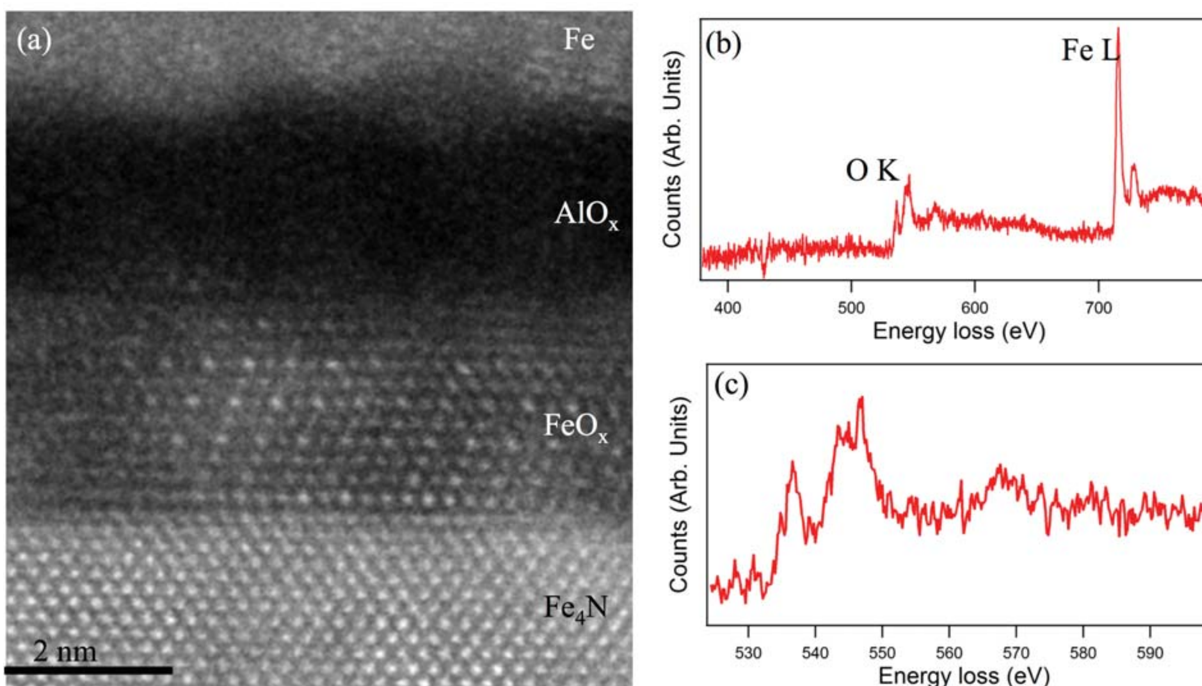

Figure 4.2.2 STEM and STEM EELS of the MTJ before annealing. (a) HRSTEM cross-section image of the MTJ before annealing. EEL spectra on (b) the FeO_x layer, (c) the enlarged view of O K edge in (b).

Figure 4.2.3 (a) shows an HRSTEM image of the $Fe_4N/AlO_x/Fe$ junction after field cooling. The reaction layer is still present at Fe_4N/AlO_x interface, but with improved crystallinity. The crystal structure of the reaction layer is similar to that of Fe_3O_4 along [110] zone axis discussed in detail in Chapter 3. To quantitatively identify the reaction layer, STEM EEL SI was done on the interface area. The extracted spectra on the upper electrode Fe, the reaction layer and the bottom electrode Fe_4N are shown in **Figure 4.2.3** (b) through (d), respectively. The EEL spectrum shows only Fe-L edge on Fe electrode, but both the N K and Fe L edges on the bottom electrode Fe_4N, as one would expect. In the reaction layer (**Figure 4.2.3** (c)), the EEL spectrum shows O K, Fe L edges and no N K edge. We have also observed similar pre peak of O K edge compared to the un-annealed MTJ. The quantification, however, provides key information that the Fe/O ratio from EELS is 0.8±0.1, which is consistent with the 0.75 Fe/O ratio of Fe_3O_4.

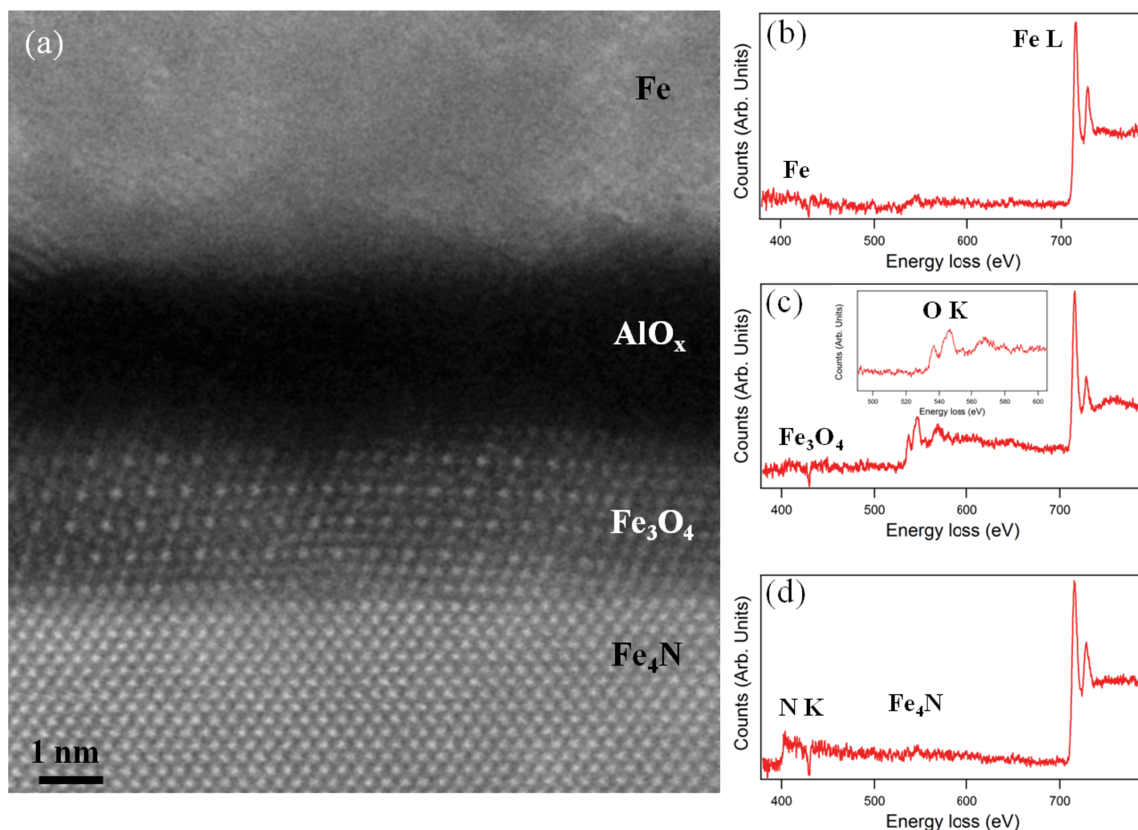

Figure 4.2.3 (a) HR-STEM cross-section image of the annealed multilayer; EEL spectra on (b) the Fe layer, (c) the reaction layer, and (d) the bottom Fe_4N layer.

The formation of Fe_3O_4 is driven thermodynamically during the oxidation of Fe_4N. The standard Gibbs free energy of formation is +3.8 $kJ \cdot mol^{-1}$ for Fe_3O_4 and -1015.4 $kJ \cdot mol^{-1}$ for Fe_4N, respectively,[182] so there will be -1018.25 kJ energy released with per mole of Fe_3O_4 formed from Fe_4N oxidation. In addition, both Fe_3O_4 and Fe_4N have cubic crystal structures. Since the lattice parameter of Fe_4N (0.3795 nm) is about half of that of Fe_3O_4 (0.8396 nm), eight Fe_4N unit cells can transform into one Fe_3O_4 unit cell with ~10% lattice mismatch, which makes the formation of Fe_3O_4 on Fe_4N lattice kinetically favorable. Phase transformation of the polycrystalline Fe_4N to Fe_3O_4, for example, has been reported in Liu *et al.*[58,183] using 400~1000 kV electron irradiation.

Oxygen has important impact on the TMR. Since oxygen was supplied by plasma oxidation of the Al layer for AlO_x to make the tunnel barrier, a fraction of the oxygen may remain at the electrode / tunnel barrier interface. We hypothesize that the remaining oxygen is more than sufficient for Fe_3O_4 formation, which is supported by the composition of the reaction layer. The extra oxygen, either in the form of FeO or not, especially near the tunneling interface, could be detrimental to the TMR. Zhang *et al.*[89] showed that theoretically, a single atomic layer of FeO in a Fe/FeO/MgO/Fe junction can greatly reduce the TMR due to the strong hybridization of the Fe and O orbitals in the FeO layer. In addition, an oxygen overlayer on top of a bcc Fe (001) surface in the vacuum leads to a positive surface SP at the Fermi energy, which reverses the sign of the intrinsic SP of Fe.[184,185] In our Fe_4N junction, the extra oxygen at the electrode / tunnel barrier interface may have destroyed the negative SP from the bulk Fe_3O_4 layer, resulting in the normal TMR for the as-prepared junction.

Conclusion

To conclude, HRSTEM characterization identified a reaction layer of FeO_x at the Fe_4N/AlO_x interface before and after field cooling. We believe that the reaction layer, FeO_x, is responsible for the abnormal behavior of the bias dependence in the MTJ. Before field cooling, the Fe/O ratio of the reaction layer is 1.1±0.1, indicating formation of FeO, but O K edge ELENS showed that the reaction layer was similar to Fe_3O_4. We believe that the reaction layer before field cooling is the combination of FeO and Fe_3O_4, which was responsible for the small positive TMR. After field cooling, the structure and the composition of the reaction layer became close to Fe_3O_4, but still showed a distorted crystal structure compared to the Fe_3O_4 thin film show in Chapter 3. This distorted Fe_3O_4 could be responsible for the small negative TMR. The

redistribution of O at Fe_4N/AlO_x interfaces drove the changes in the compositions of the reaction layer.

Chapter 5 Ferromagnet/Oxide Interfaces in Co_2MnSi/MgO Magnetic Tunnel Junctions

Table 2 Spin polarization (SP) of the density of states at the Fermi level, calculated by projecting onto the orbitals of the interface and sublayer atoms, for four terminations of the Co_2MnSi/MgO interface.[186]

Termination	MnMn/O	CoCo/O	MnSi/O	SiSi/Mg
SP	1.00	0.67	-0.01	-0.25

Imperfect spin-dependent tunneling at the Heusler alloy / insulator interface may significantly limit the performance of CMS/MgO MTJs.[186] As discussed in Section 1.6.3, CMS with 100% spin polarization has an $L2_1$ ordered structure. Based on first principles calculations, four interface terminations can exist at the CMS/MgO interface: CoCo/O, MnMn/O, MnSi/O and SiSi/Mg.[88,186,187] (CoCo/O means that at the interface a plane of entirely Co faces the MgO and bonds entirely to O; the other interface designations are analogous.) Miyajima *et al.* also proposed a disordered termination with a mixture of Co, Mn, and Si.[188] Other interfaces have been simulated, but found to be unstable.[187] Only MnMn/O termination, which is thermodynamically metastable, gives 100% spin polarization of the zero-temperature density of states at E_F as show in **Table 2**. The other terminations listed are stable, but have interfacial states at E_F in the minority spin band: CoCo/O is 67% spin polarized, and MnSi/O and SiSi/Mg have the opposite sign of spin polarization from the bulk CMS.[88,186,189] Even for half-metallic electrodes, minority-spin interface states create tunneling conductance for the antiparallel magnetization configuration at finite temperatures through spin-flip scattering, [39,43] so half-metallic interface states are needed to fully realize the potential of half-metallic electrodes like CMS.

5.1 MTJ Structure and Fabrications

The CoFe / MgO / CMS MTJs consist of MgO substrate / MgO buffer (10 nm) / $Co_{50}Fe_{50}$ (30 nm) / MgO barrier (1.4-3.2 nm) / $Co_2Mn_\alpha Si$ (3 nm) (α = 0.8, 1.0, or 1.29) / Ru (0.8 nm) / $Co_{90}Fe_{10}$ (2 nm) / $Ir_{22}Mn_{78}$ (10 nm) / Ru cap (5 nm). The multilayers were deposited in an ultrahigh vacuum chamber with a base pressure of $\sim 6\times10^{-8}$ Pa. The lower CoFe electrode was deposited by magnetron sputtering at room temperature and annealed *in situ* at 500 °C. The MgO barrier was deposited by electron beam evaporation at room temperature. The nominal thickness of the MgO barrier was varied from 1.4 to 3.2 nm on each 20×20 mm^2 substrate by a linear motion of a shutter during deposition. The CMS electrode was deposited at room temperature by magnetron co-sputtering from a nearly stoichiometric CMS target and an Mn target. Excess Mn in the CMS electrode suppresses Co antisite defects,[190,191] which reduce the bulk spin polarization of CMS.[82]

5.2 Determination of MnMn/O Interface Termination

A Z-contrast STEM image of a CMS/MgO MTJ viewed along the [110] projection of the CMS is shown in **Figure 5.2.1 (a)**. The junction has TMR of 1049% at 4.2 K and 335% at 290 K,[41] among the highest reported for CMS/MgO.[192] **Figure 5.2.1** (b) shows a closer view of the CMS/MgO interface in **Figure 5.2.1** (a). Based on the intensity variations in the atomic columns, the CMS has the $L2_1$ ordered structure away from the interface. Two different CMS/MgO interface terminations coexist in the image. Between the arrows in **Figure 5.2.1** (b), the final layer of the CMS facing the MgO is pure Co, so we identify this termination as CoCo/O. On the right hand side of **Figure 5.2.1** (b), a different termination occurs, in which the two planes in the CMS closest to the interface both have constant intensity. The horizontal profiles 1 to 3 in

Figure 5.2.1 (c) extracted from the indicated regions in **Figure 5.2.1** (b) show the difference between the MnSi planes in the CMS, which show clear contrast between Mn and Si columns from the $L2_1$ structure, and the terminating interface plane in profile 4, which has constant peak intensity.

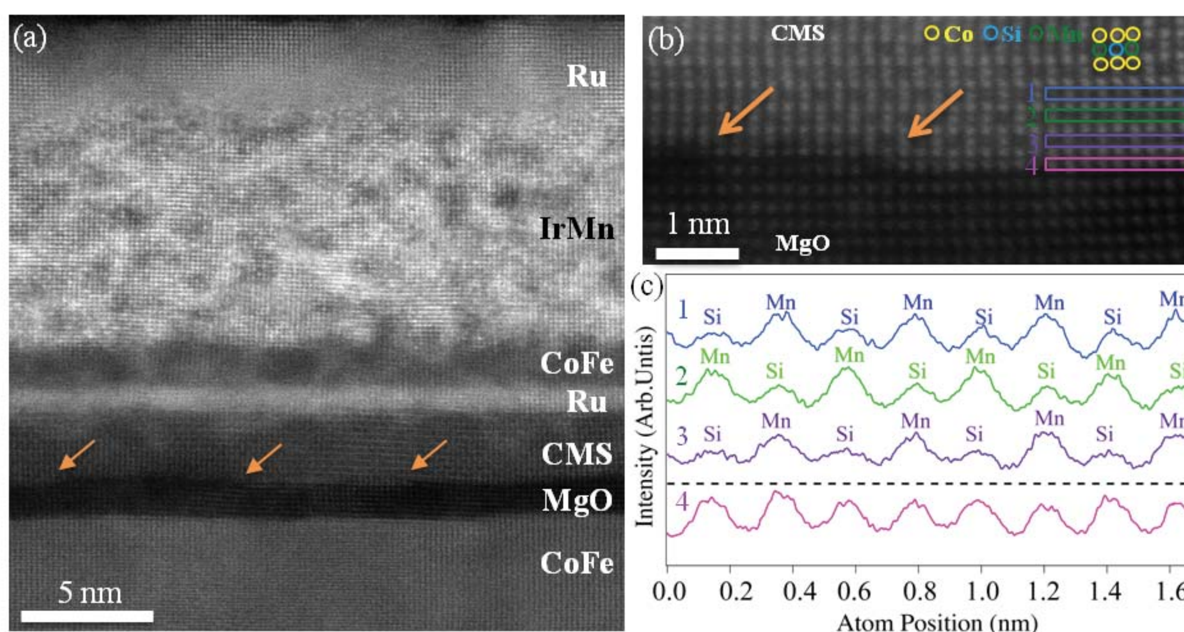

Figure 5.2.1 (a) Z-contrast STEM image of the MTJ structure, (from the bottom) CoFe/MgO/$Co_2Mn_{1.29}Si$/Ru/CoFe/IrMn/Ru, with steps at the MgO/CMS interface indicated by arrows. (b) Z-contrast image of the MgO/CMS showing two different interface terminations. Switching between terminations is caused by the steps on MgO marked with orange arrows. (c) Horizontal profiles taken on the numbered MnSi planes in (b) show $L2_1$ ordering within the film but not at the interface.

We propose that this second interface termination is MnMn/O, based on evidence contradicting the other possible stable terminations and on positive evidence consistent only with MnMn/O. **Figure 5.2.2** shows that the $Co_2Mn_{1.29}Si$/MgO interface has metal-oxygen bonding using annular bright field (ABF) STEM, which is particularly useful for imaging light elements.[193] **Figure 5.2.2** (a) and (b) are Z-contrast and ABF STEM images, respectively, of the structure we identify as MnMn/O rotated to the [100] projection of the CMS. In this orientation, the Mg and O sublattices are visible as separate atomic columns. The O is visible in the ABF

image, but not in the Z-contrast image due to its low Z. Both images show metal-oxygen bonding across the interface, which is consistent with MnMn/O and rules out the SiSi/Mg termination.

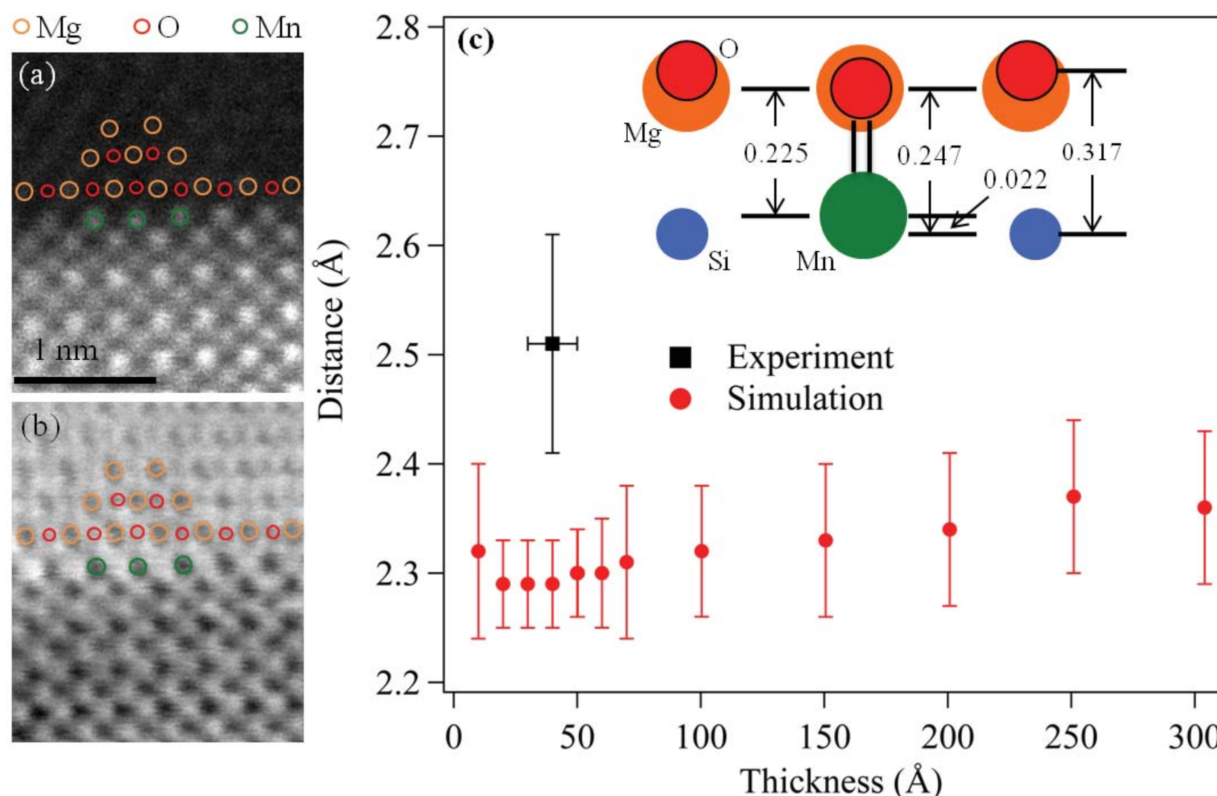

Figure 5.2.2 (a) Z-contrast and (b) ABF STEM images of the MnMn/O interface along the CMS [100] zone axis in the same MTJs used in Figure 5.2.1, showing metal-oxygen bonding across the interface. (c) Measured interplanar distance across the MnMn/O interface and simulated distance as a function of thickness for a disordered MnSi/O interface. The inset shows the ordered MnSi/O interface which is the basis for the disordered interface simulations.

The constant peak intensity in **Figure 5.2.1** (c) rules out the ordered MnSi/O termination, but the Z-contrast intensity does not provide much further information. As shown in **Figure 5.2.3**, the Z-contrast intensity perpendicular to the interface in **Figure 5.2.3** (b) decreases smoothly up to the interface over 2-4 planes inside the CMS, even though in the image the interface appears flat and compositionally abrupt. We attribute the spread of the intensity gradient to static strain disorder at the interface.[194] Higher detector inner angles suppress strain

contrast in Z-contrast STEM,[99] which we observed for the second interface type as shown in **Figure 5.2.3** (b)-(d). The intensity gradient decreases with increasing detector inner angles, consistent with the behavior of contrast from strain.[99] With larger detector angles, the intensity difference between Mn in CMS and Mn at the interface gets smaller, but even at the largest practical detector angle of 84.4 mrad, the interface plane intensity is still lower than either the Si or Mn columns in the bulk.

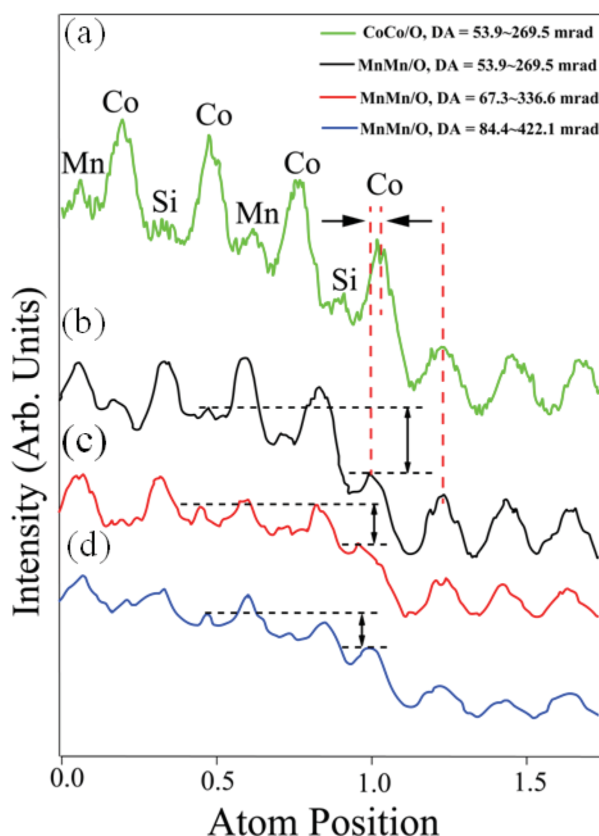

Figure 5.2.3 (a)-(d) Line profiles across the (a) CoCo/O and (b) MnMn/O interfaces in Figure 1(b). Both (a) and (b) show a decrease in intensity at the CMS/MgO interface caused by strain. (c) and (d) show that at larger detector inner angle, the intensity drop across the interface is smaller and more abrupt. The vertical lines mark the lattice distance across the interface.

The structure we identify as MnMn/O was also observed by Miyajima *et al.*[188] in Z-contrast STEM images of the CMS/MgO interface. They interpreted it as a disordered mixture of Mn, Si, and Co from the two planes of the CMS closest to the interface. They reported that

the Z-contrast intensity in the final plane of the CMS is higher than the intensity from ordered MnSi planes away from the interface and the intensity of the Co plane next to the interface is lower than Co planes away from the interface, consistent with their interface model. However, this pattern of intensities only exists after they have subtracted an arbitrary "smooth function" [188] from the experimental intensities to account for a strain-induced interface intensity gradient like the one we observe in **Figure 5.2.3**. Our samples show a smaller intensity gradient near the interface, perhaps because they are thinner, and if we suppress the strain contrast using large detector angles, as in **Figure 5.2.3** (c), the Co plane next to the interface is the same absolute intensity as Co planes in the bulk. The interface plane is lower in intensity than any plane in the bulk for all detector angles, but the peak-to-valley contrast along the interface layer in the profile in **Figure 5.2.1** (c) is quite similar to the contrast of the Mn columns in the plane away from the interface and substantially larger than the contrast of the Si columns. Thus, if we follow Miyajima *et al.*[188] and treat the strain contrast as an additive background that is constant along the interface plane, the interface plane contrast is more consistent with MnMn/O than a disordered mixture of Co, Mn, and Si.

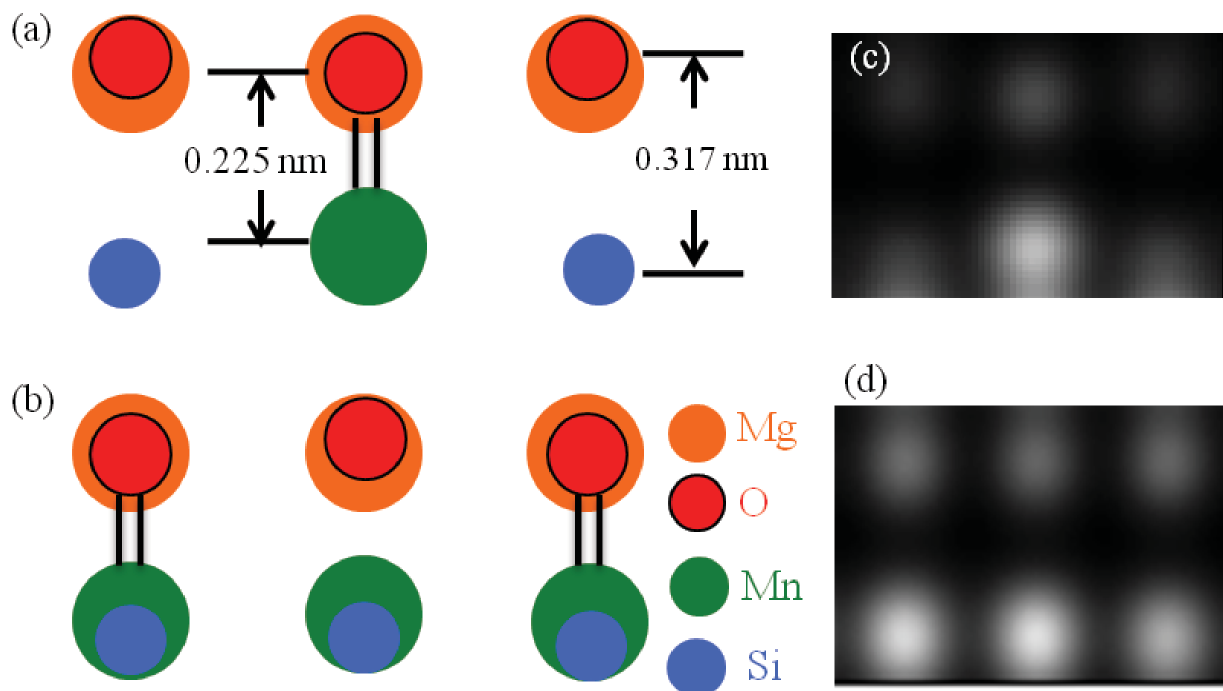

Figure 5.2.4 (a) and (b) are ball-stick models for the ordered and disordered MnSi/O terminated interfaces, respectively. Simulated images for (c) the ordered MnSi/O terminated interface at 5 nm thickness. and (d) the disordered MnSi/O terminated interface at 4 nm thickness.

More conclusive evidence for MnMn/O comes from the distance between the final CMS plane and the first MgO plane. For the interface we identify as MnMn/O, the distance is 0.25 ± 0.01 nm as shown in **Figure 5.2.2** (c), averaged over 30 interface bonds and with one standard deviation of the mean uncertainty. Similar values have been obtained for other images from other sample areas, with the STEM scan rotated by 90 degrees, and from the ABF image in **Figure 5.2.2** (b). This value agrees only with the simulated value for MnMn/O, 0.240 nm.[186] In addition, we measure a distance of 0.20 ± 0.01 nm from our STEM images for the CoCo/O interface, in good agreement with the simulated values of 0.20 nm[88] and 0.209 nm.[186] In both theoretical studies, the simulated CMS lattice parameter parallel to the interface[88,186] is in good agreement with the experimental value.[195]

We used STEM image simulation to further confirm the MnMn/O interface termination. We built models for investigating the ordered and disordered MnSi/O terminated interfaces

based on structures reported by Miura[88] and Hülsen.[186] **Figure 5.2.4** (a) and (b) show ball-stick models for the ordered and disordered MnSi/O terminated interfaces, respectively, viewed along the $[110]_{CMS}||[100]_{MgO}$ projection. The ordered interface in **Figure 5.2.4** (a) has a Mn-O bond distance of 0.225 nm and a Si-O distance of 0.317 nm.[88] Based on the distances reported by Miura *et al.*,[88] we calculated that because of the relaxation of the Si and O, the Si atoms moved 0.022 nm back into the CMS, and the first neighbor O of the interface Si moved 0.07 nm back into the MgO. The perpendicular distance from the Si to the Mg, which is primarily what is observed in Z-contrast STEM in this orientation, is thus 0.247 nm. To construct the disordered MnSi/O terminated interface, interface atoms of the CMS were randomly assigned to Mn or Si with equal probability, and then shifted to keep the same Mn-O, Si-O, and Mn-Si distances as the ordered interface. The disordered structure was not further relaxed, so homonuclear (Si-Si or Mn-Mn) interactions within the CMS interface plane or any second-neighbor interactions were not taken into account.

STEM image simulations were performed via the frozen phonon multislice algorithm[105] with a 40 Å × 40.8 Å × 304 Å supercell sampled with 2048×2048 pixel wavefunctions. The simulations were carried out with the same parameters used in the experiments: 200 keV, convergence semi-angle of 24.5 mrad, and high angle annular dark field (HAADF) detector inner and outer semi-angles of 53.9 and 270 mrad, respectively. Typical measured aberration values for our STEM up to A5 were used, although the exact lower-order aberrations for the experimental images are not known. Thermal diffuse scattering was introduced via the frozen phonon algorithm at 300 K. The Debye-Waller (D-W) factors for Co and Mn were obtained from the D-W factors of the Co_2MnGe at room temperature.[196] The D-W factor of Si was calculated from the factor for Ge atoms in Co_2MnGe,[196] scaled for the atomic mass of Si using the harmonic

oscillator approximation. The slice thickness was 2 Å. Simulations were averaged over 12 phonon displacement configurations for the disordered interface and 4 phonon configurations for the ordered interface. The simulated images were convolved with a Gaussian with a full width at half maximum of 88.2 pm after the simulation to account for incoherent source broadening. The Gaussian source size was determined by matching simulated and experimental images of GaN, following LeBeau *et al*.[197] **Figure 5.2.4** (c) and (d) are two simulated images of the disordered and ordered MnSi/O interfaces, respectively. For the disordered MnSi/O terminated interface, we calculated images for sample thicknesses of 1 nm, 2 nm, 3 nm, 4 nm, 5 nm, 6 nm, 7 nm, 10 nm, 15 nm, 20 nm, 25 nm and 30.4 nm. For the ordered interface, we calculated the images for sample thicknesses of 5 nm, 10 nm, 15 nm, 20 nm, 25 nm and 30.4 nm.

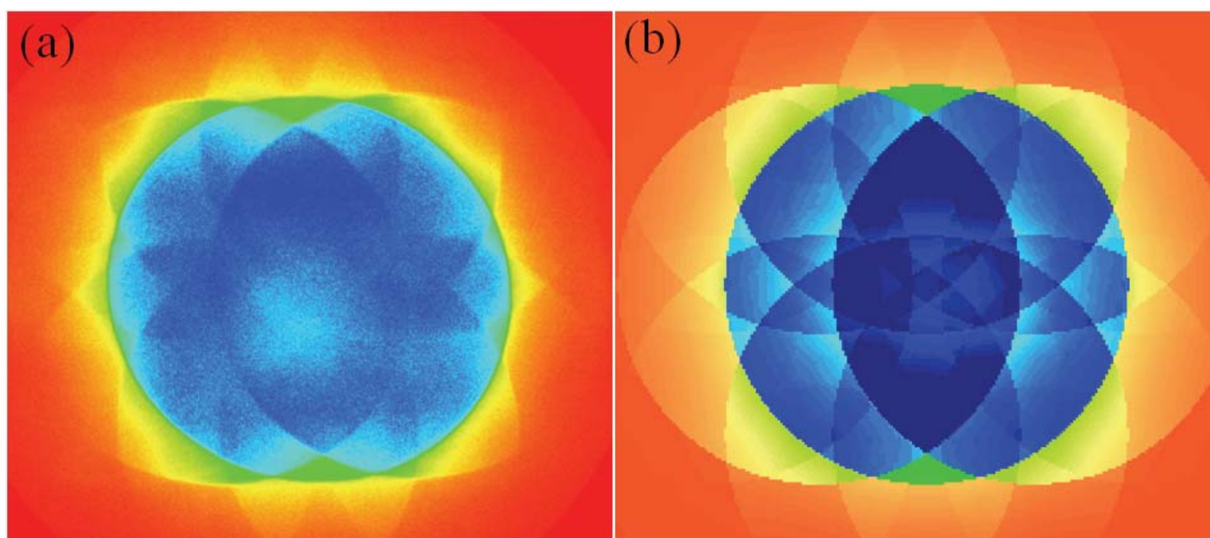

Figure 5.2.5 (a) Experimental PACBED pattern on a typical sample with clear CMS/MgO interface. (b) Simulated PACBED pattern of 4 nm thick CMS.

For comparing the experimental data with simulated one, specimen thickness needs to be determined. Position averaged convergence beam electron diffraction (PACBED)[112] was used to determine the sample thickness. We acquired an experimental PACBED pattern from inside the CMS, near an areas used to determine the interface termination. For the PACBED simulation,

we used the same parameters as the image simulations. Thermal diffuse scattering was introduced via the frozen phonon algorithm with 16 phonon configurations at 300 K. The best match between the measured and simulated PACBED determines the experimental thickness, as shown in **Figure 5.2.5** (a) (experimental) and (b) (simulated). The simulated PACBED pattern contains more fine structure inside the bright field disk than the experiment, indicating that there may be some point defects or thin amorphous surface layers in the experiment that are not present in the simulation. These features limit our ability to exactly match the experimental and simulated PACBED patterns, so we estimate the uncertainty in the thickness determined by this method to be ±1 nm, similar to LeBeau *et al.*'s result. [112]

As shown in the inset to **Figure 5.2.2** (c), in ordered MnSi/O, the simulated Mn-O distance is 0.225 nm[88] (0.227 nm[186]), inconsistent with our measured value. The Si and O are not bonded, leading to relaxation of the Si into the CMS and the O into the MgO, so the Si-O distance is 0.317 nm.[88] However, the perpendicular distance between the Si plane and Mg plane is 0.247 nm,[88] which is consistent with our measured value. Thus, we must consider an interface with MnSi/O termination but with site disorder of the Mn and Si in the termination plane as a possible explanation for both the constant contrast along the interface plane and the interface plane distance.

We extracted the inter-plane distance across the interface from the simulated images by fitting Gaussian peaks to line profiles drawn perpendicular across the interface, then calculating the difference between the Gaussian centers. This method is needed due to the relatively poor pixel sampling of the simulated images. The uncertainty in the distance arises from the fitting uncertainty and variation in measurements for several atom pairs across the interface in each simulation, reflected by the standard deviation. At very small sample thicknesses, the standard

deviation is larger because the fractional variation in the Mn and Si concentration from column to column is larger due to the small total number of atoms through the thickness. For the experimental thickness, the estimated interplanar distance is 0.229±0.004 nm, which is dominated by the Mn-O bond length, and smaller than the experimental value, as shown in **Figure 5.2.2** (c).

Image simulations show that for the disordered interface, the distance in the Z-contrast image is dominated by the stronger scattering from the Mn. **Figure 5.2.2** (c) shows interface plane distances measured from frozen-phonon multislice simulations of Z-contrast images of a disordered MnSi/O interface with the same interface bond distances as the ordered interface. The distances in the simulated images have some thickness dependence, which we speculate arises from probe channeling through the disordered interface plane. However, at the experimental thickness of 4±1 nm, determined by position averaged convergent beam electron diffraction[198] (**Figure 5.2.5**), the experimental distance is inconsistent with the disordered MnSi/O interface.

Therefore, from data inconsistent with CoCo/O, SiSi/Mg, mixed Co, Mn, and Si, and ordered and disordered MnSi/O, and from data consistent with MnMn/O, we conclude that the second termination type on the right of **Figure 5.2.1** (a) is MnMn/O, even though that termination is metastable. Attempts to confirm this assignment by high-resolution microanalysis using electron energy loss spectroscopy or energy-dispersive x-ray spectroscopy failed because the interface was destroyed by the high electron dose required by those experiments. The interface plane is in fact more beam-sensitive than the interior of either the CMS or MgO thin films.

The changes in interface termination in **Figure 5.2.1** (a) and (b) are associated with monolayer steps of the MgO. The MgO in this MTJ is deliberately wedge-shaped, which may

have oriented the steps parallel to the electron beam, enabling this observation. The change in interface termination accommodates the MgO surface steps without generating defects such as grain boundaries or antiphase boundaries in the CMS. The absence of extended defects, especially near the interface, may enhance coherent tunneling. Theoretical calculations of coherent tunneling at the CMS/MgO have only considered the CoCo/O termination[199] or the MnSi/O termination,[88] so further calculations considering coherent tunneling for the MnMn/O interface are needed. Interface roughness is well known to influence TMR by changing the tunnel barrier thickness, but the relationship between steps on the MgO and the CMS/MgO interface termination points to another mechanism by which interface roughness influences TMR.

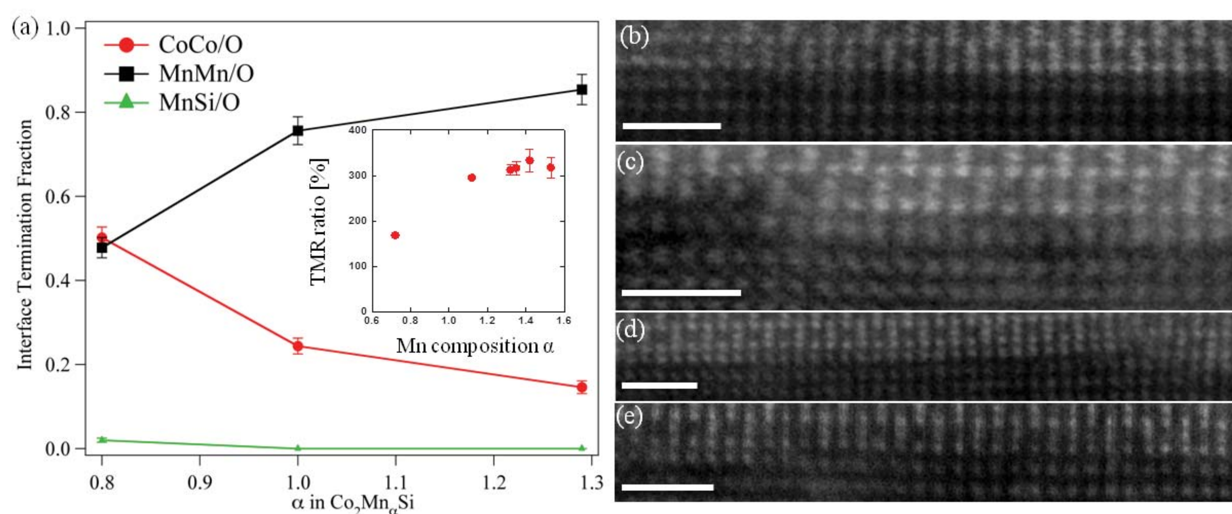

Figure 5.2.6 (a) Fraction of CoCo/O, MnMn/O and MnSi/O interface terminations as a function of Mn concentration in $Co_2Mn_\alpha Si$, estimated from Z-contrast images such as (b)-(e). The inset figure shows TMR for $Co_2Mn_\alpha Si$/MgO MTJs with different Mn concentration. (Data acquired by Dr. Hongxi Liu) (b) CoCo/O and (c) MnMn/O and MnSi/O termination in a $Co_2Mn_{0.8}Si$ MTJ. (c) and (d) Larger areas of MnMn/O and CoCo/O termination in a $Co_2Mn_{1.0}Si$ MTJ. The scale bars are 1 nm.

Although MnSi/O was calculated to be the most stable termination[186] and reported in previous experiments,[188,200] we do not observe it in our MTJs. We speculate that the lack of

MnSi/O and the presence of MnMn/O arise from high Mn chemical potential on the film surface during non-equilibrium growth by sputtering. To test this hypothesis, we examined a series of junctions with varying Mn content and estimated the fractions of MnMn/O, CoCo/O, and MnSi/O interface terminations, as shown in **Figure 5.2.6** (a). Mn concentration in the films was determined by inductively coupled plasma optical emission spectroscopy with an accuracy of 2% to 3% for Co or Mn and 5% for Si.[41] Typical images used to estimate the interface termination fractions are shown in Figure 3b-d. The estimates in Figure 3a are fractions of the observed interface length, but because termination switch is driven by steps and the steps run mostly parallel to the electron beam, we believe this is a good estimate of the interface area as well. Random uncertainties are estimated as the square root of the number of interface unit cells counted for each interface type.

Figure 5.2.6 (a) shows a clear trend toward higher MnMn/O fraction and lower CoCo/O fraction at higher Mn content, suggesting that high Mn chemical potential during non-equilibrium deposition may be responsible for the MnMn/O termination. Hülsen *et al.* calculated that MnMn/O is only stable at high Mn chemical potential,[186] outside the stability range of the bulk phases, so we must appeal to the out-of-equilibrium nature of thin film growth by sputtering, where kinetic constraints may prevent decomposition of the CMS film even at high Mn chemical potential on the surface.

We found only 2% MnSi/O interface termination at the CMS/MgO interface with $\alpha = 0.8$, the lowest Mn concentration we studied. Saito *et al*.[200,201] reported mainly MnSi/O termination in a Fe/$Co_2Mn_{0.91}Si_{0.93}$/MgO half junction from x-ray magnetic circular dichroism (XMCD) measurements as a function of film thickness. However, they did not consider the metastable MnMn/O termination in their modeling of the XMCD data. Hülsen *et al.*[186] suggested that

Saito's early results[201] may be consistent with MnMn/O. Miyajima *et al.*[188] studied MTJs with stoichiometric CMS layers and focused their attention primarily on observation of the MnSi/O termination, but did not report the interface termination fractions.

The inset figure of **Figure 5.2.6 (a)** shows the room temperature TMR also increases with the Mn concentration in the similar junctions. We expect MnMn/O termination to substantially increase the finite-temperature TMR of CMS/MgO-based MTJ by two mechanisms. First, the half-metallic MnMn/O termination has no minority spin states, so it reduces the tunneling conductance in the anti-parallel magnetization configuration by suppressing spin-flip tunneling through minority-spin interface states coupled to magnons. Second, more MnMn/O termination means less CoCo/O termination, and CoCo/O is subject to spin-flip tunneling in the antiparallel configuration due to instability of the interfacial Co spin moment.[43,202] More experimental and theoretical research is required to understand the influence of MnMn/O termination in detail, but we believe it is very encouraging for future device performance that Mn-rich CMS electrodes facing a MgO barrier can create a half-metallic interface as well as a half-metallic electrode.[191]

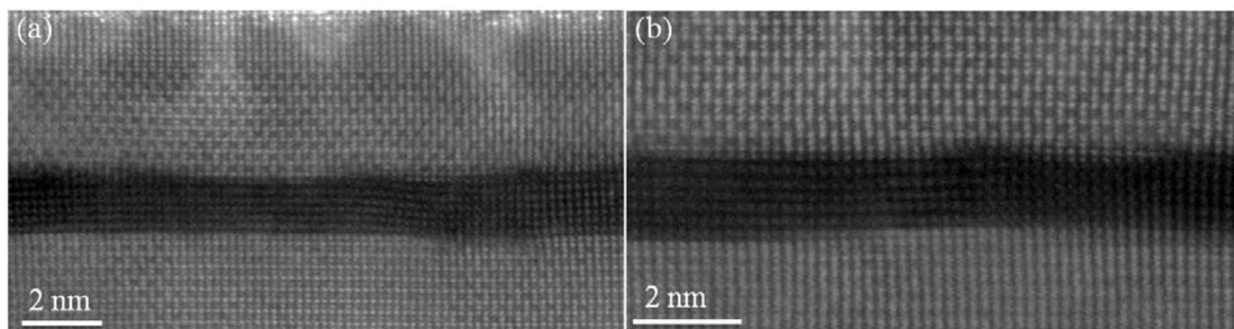

Figure 5.2.7 (a) and (b) are HRSTEM images of MTJs with CMS as both electrodes. The Mn concentration here in the CMS electrode is $\alpha = 0.72$

The junctions described so far have Co bottom electrodes and CMS upper electrodes. **Figure 5.2.7** shows images of junctions with CMS top and bottom electrodes. Both electrodes are Mn deficient. At the bottom CMS/MgO interface, mainly MnMn/O termination was observed,

but at the upper CMS/MgO interface, MnSi/O and CoCo/O terminations can also be found. We suspect the asymmetry is driven by surface roughness. The bottom CMS electrode is deposited on a very smooth CoFe buffer layer, and then annealed at high temperature to give it a smooth surface. The upper electrode is deposited on MgO, which typically has a rougher top surface and is not as readily smoothed by annealing. Since interface steps switch the termination, a rougher interface means more switching and more CoCo/O, even if MnMn/O is otherwise favored.

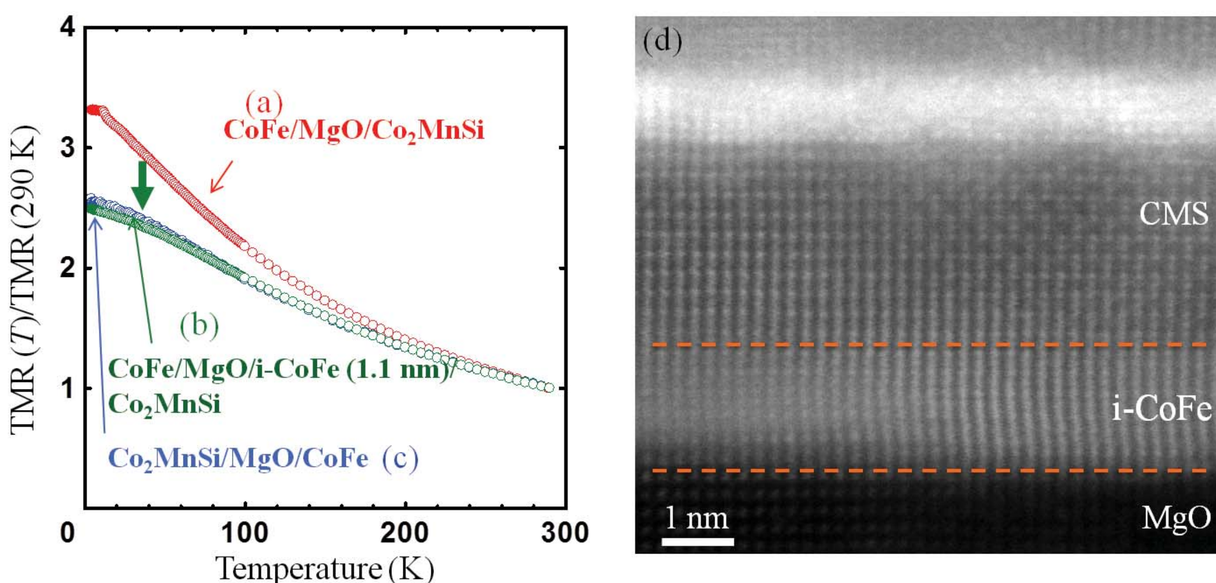

Figure 5.2.8 Temperature dependence of three types of junctions is shown in (a) through (c), respectively. CMS in all three MTJs are Mn rich, with $\alpha = 1.29$. (Acquired by Dr. Hongxi Liu, unpublished) (d) HRSTEM image of CoFe/MgO/i-CoFe/Co_2MnSi MTJ.

In Chapter 1.3, both theoretical and experimental work showing that FM/tunnel barrier interfaces affect the temperature dependence of TMR in CMS based MTJs is summarized. The magnetic moment of Co fluctuates easily, which causes spin flip scattering at the interface at finite temperature. Therefore, MTJs with CoCo/O interface terminated interfaces should show decrease in TMR with increasing temperature, exactly as shown in **Figure 5.2.8** (a), which compares an MTJ with an upper CMS electrode to an MTJ with CoFe / MgO interfaces only. MTJs with CMS as the lower electrode and with mainly MnMn/O terminated interface should

show weaker temperature dependence confirmed by **Figure 5.2.8** (c). The difference in the temperature dependence is the results of interface termination. **Figure 5.2.8** (d) shows how inserting an ultrathin CoFe at CMS/MgO interface avoids the problem of interface termination at the CMS / MgO interface entirely. Thus, the temperature dependence in **Figure 5.2.8** (c) of the junction shown in **Figure 5.2.8** (d) is similar to **Figure 5.2.8** (b).

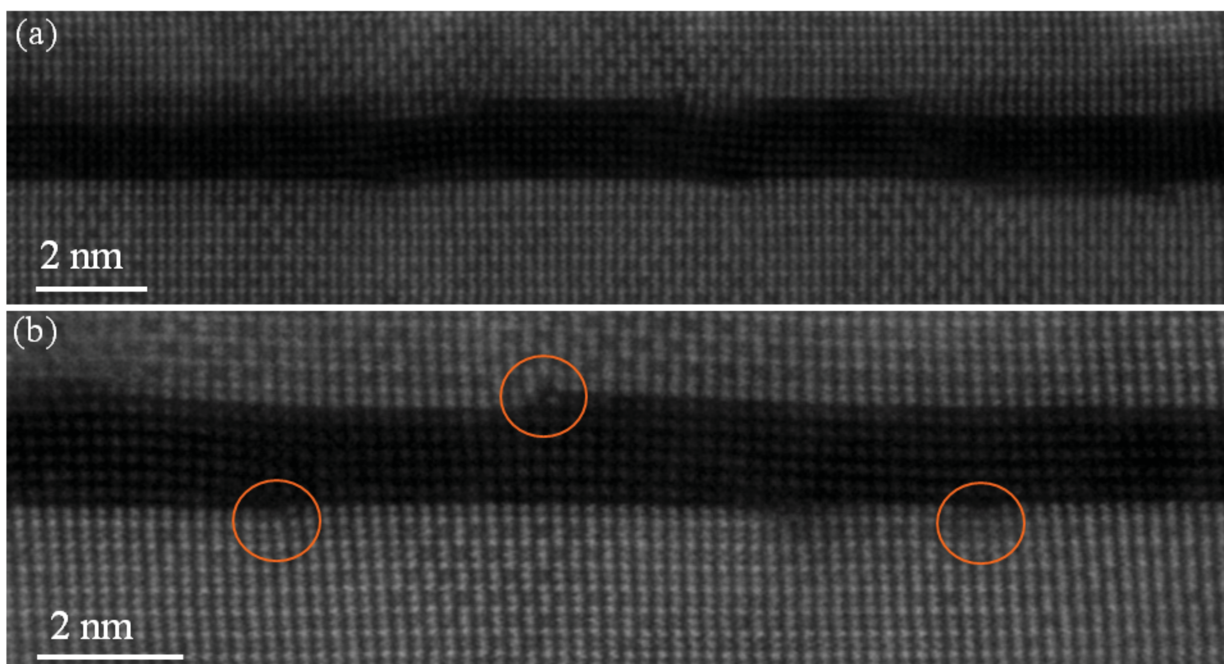

Figure 5.2.9 (a) and (b) HRSTEM images of CMFS/MgO/CMFS MTJs after ex-situ annealing. In (b), three defects are pointed out by the orange circles.

We applied the same analysis to investigate the interfaces of $Co_2Mn_{1.24}Fe_{0.16}Si$ (CMFS) with MgO in a junction with CMFS as both electrodes. The CMFS MTJ has TMR of 429 % at RT and 2611% at 4.2 K, which is much higher than MTJs with CMS electrodes. Fecher *et al.*[203] investigated spin polarizations of a series of $Co_2Mn_xFe_{1-x}Si$ with x = 0, 0.5 and 1. Their theoretical calculation shows that all three compounds are half metallic.[203] As shown in **Figure 5.2.9** (a) the upper CMFS/MgO interface is rougher than the lower interface. The main type of interface termination for both interfaces is Mn(Fe)Mn(Fe)/O. However, it is hard to determine the composition of the terminating plane because electron microanalysis such as EELS and EDX

destroys the interfaces. In **Figure 5.2.9** (b), misfit dislocations are highlighted by the orange circles. Right at the dislocations, the interface termination is Mn(Fe)Si/O, which is not half metallic across Fermi level.

Figure 5.2.10 shows a dark field TEM image of the $Co_2MnFeSi$/ MgO/ $Co_2MnFeSi$ interfaces, which both contain the periodic mismatch dislocations. The dislocation spacings for the upper and lower interfaces are 6.3 ± 0.3 nm and 6.1 ± 0.2 nm, respectively. Compared to images of CMS/MgO/CMS interfaces taken under the same condition **g** = $[200]_{MgO}$,[204] CMFS/MgO has a larger spacing, and lower mismatch dislocation density. Lower misfit dislocation density improves the coherent tunneling spin filtering and thus increases TMR.

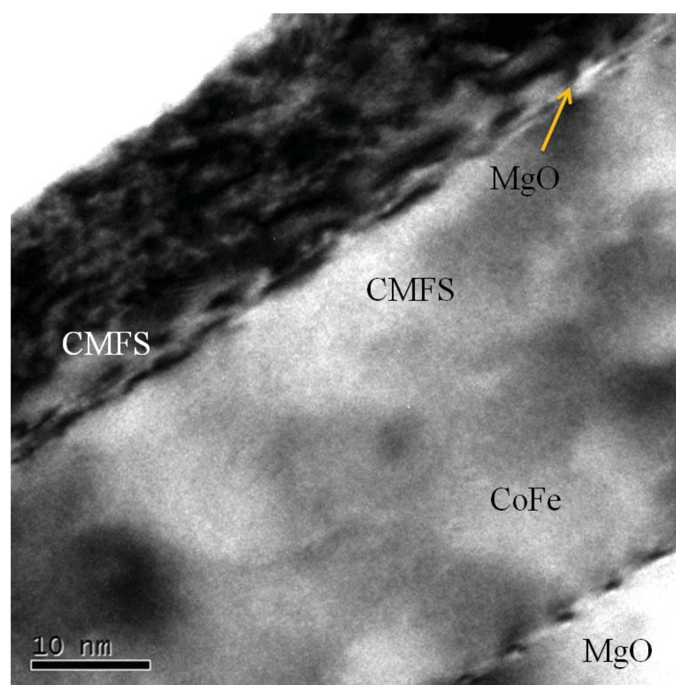

Figure 5.2.10 A dark field TEM image of MgO (sub)/CoFe/$Co_2MnFeSi$ (CMFS)/MgO/CMFS/CoFe/IrMn/Ru multilayer structure. I picked g = [020].

In conclusion, using high-resolution Z-contrast STEM we have found that the half-metallic MnMn/O interface termination dominates the MgO/CMS interface in CoFe / MgO / CMS MTJs. The next most prevalent interface termination is CoCo/O, and monolayer steps in

the MgO cause switching from one termination to the other. Increasing Mn co-sputtering during CMS growth increases the fraction of the interface with MnMn/O termination. Inserting an ultrathin CoFe layer eliminates the interfacial state that leads to strong temperature dependence of TMR. Design of structures with a higher fraction of MnMn/O termination may yet reach the promise of very high spin polarized currents from half-metallic CMS electrodes in MTJs and other spintronic devices.

5.3 Channeling Effect on EELS Quantification of CMS

When we investigated the series of CMS junctions with different Mn concentrations, tried to measure the CMS composition by EELS. However, EELS acquired with the sample oriented on the [110] zone axis shows a very small Si signal. We believe that probe channeling effect plays an important role on the quantifications of CMS. To reduce the effects of channeling, we tilted the sample off the zone axis. The farther we tilted away from [110] zone axis, the stronger the Si L edge becomes. Therefore, if we want to obtain the right compositions of CMS, avoiding strong channeling condition will be beneficial.

In Chapter 2.3, EELS is introduced to measure the energy loss characteristic of particular elements. The ELNES can provide information of the local DOS of unoccupied states in the sample. When the incident beam goes through the sample, it is deformed by the specimen lattice potential. If a crystal is orientated to a high-symmetric zone axis, the electrons that travel down the zone axis focus on the atom columns due to the attraction to the atomic nucleus screened by the inner core electrons. This channeling peak oscillates with depth in the specimen.[205] From another point of view, channeling effect is explained by Bloch waves. The solution of the Schrödinger equation for an electron moving in a crystal is a Bloch wave, even at 200 kV. Which Bloch waves are excited and with what amplitude are highly dependent on the crystal

orientation. If the sample is on a zone axis, the most intense Bloch state is a 1s state localized on the atom columns. The 1s Bloch state interferes with other Bloch states, leading to oscillations in the on-column electron amplitude. The cooperative focusing by a column of atoms is called channeling effect.[206] Channeling increases the resolution in STEM especially for a relatively thick samples. Tilting off the zone axis excites a broader range of Bloch states, resulting in less pronounced oscillations in the on-column intensity as a function of thickness.

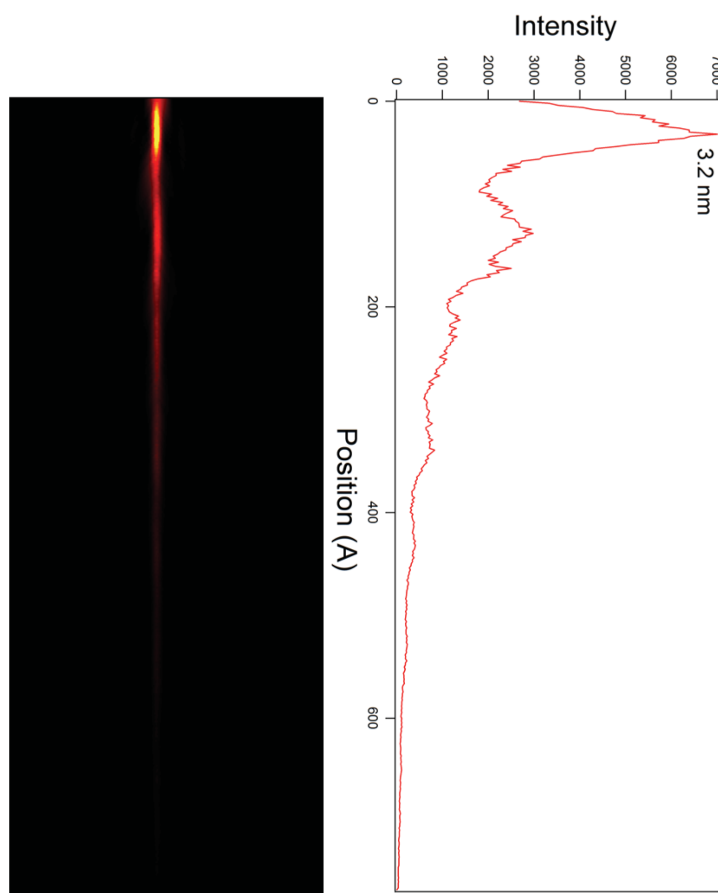

Figure 5.3.1 (a) A 200 kV probe channeling depth-sectioning image on Si column in CMS [110] zone axis. (b) Line profile just along the Si column shown in (a).

Figure 5.3.1 (a) shows simulated probe channeling on the Si column of CMS for a 200 kV probe with convergence angle 17.5 mrad. A line profile on the Si column is as shown in **Figure 5.3.1** (b). The first peak appears at 3.2 nm, which is close to the entrance surface of the

sample, The profile shows that the Si atoms see a large probe intensity only in the first 3 nm of the sample. After that, the probe is disperses throughout the sample, exciting all the atomic species equally, and at some thicknesses may re-condense on Co or Mn atomic columns with larger positive charge. Therefore, typical sample thickness used for EELS composition measurements (~0.5 λ, 50 nm), the signal that contributes to the Si EELS signal is less than 10% and the rest of sample only contributes the background as the Si edge energy, which makes the edge less prominent.

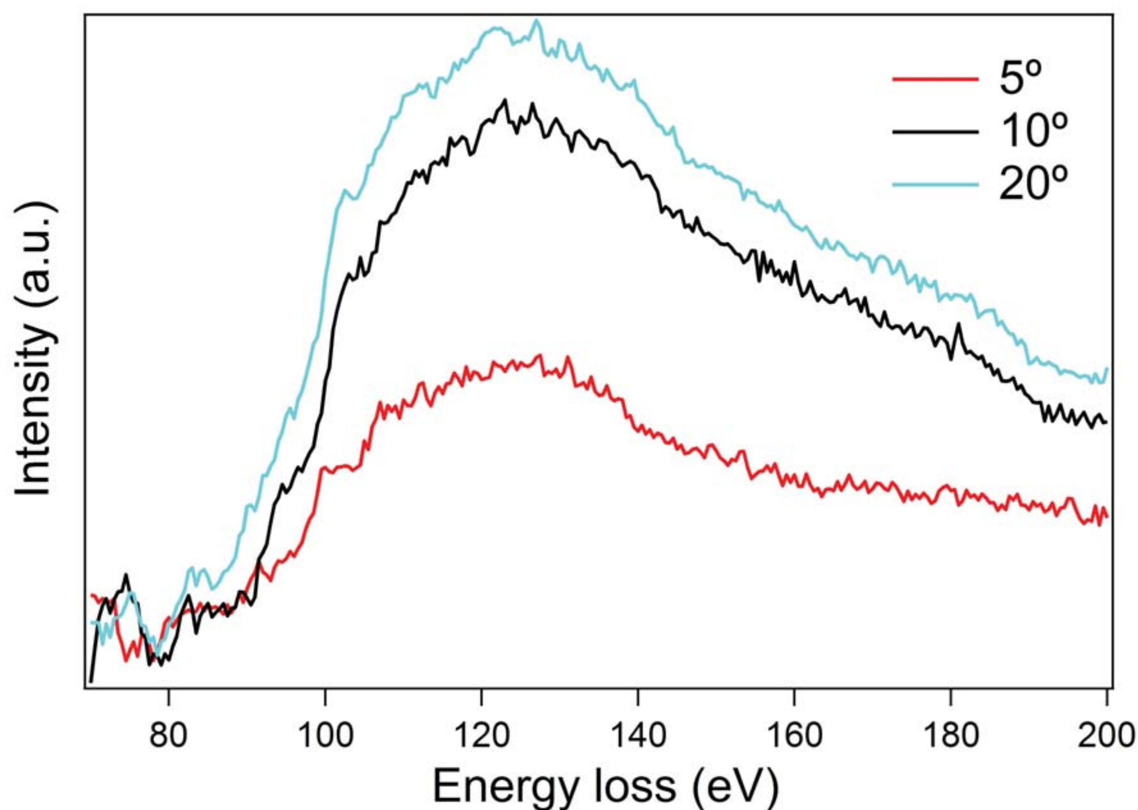

Figure 5.3.2 Normalized EEL spectra of CMS along [110] zone axis by (a) 5 degrees, (b) 10 degrees and (c) 20 degrees, respectively.

Multilayer thin film (from bottom to top) MgO (substrate) / $Co_2Mn_{1.15}Si_{0.88}$ / MgO / AlO_x was deposited using the same method described in Chapter 5.1. EELS experimental conditions are described in Chapter 2.4. The plural scattering was removed by Fourier log deconvolution.[111]

Figure 5.3.2 shows a series of normalized EEL spectra on the sample area but with different tilting angles 5º, 10º and 20º, respectively. The intensity of Si L edge increases with increasing tilt angles. The Si/Co atomic ratio from EELS quantification also show an consistent increase from 0.25 ± 0.04 to 0.40 ± 0.15 with increasing tilt angles away from CMS [110] zone axis. Thus, CMS must be tilted away from strong channeling conditions to obtain reliable composition measurements.

Chapter 6 O K edge ELNES of Fe oxides investigated by STEM EELS

Introduction

EELS is often used for detecting valence changes in transition metals in their oxide forms based on O K edge ELNES and transition metal L edge core level shifts.[207] Despite this, there are conflicting reports in the literature regarding the ELNES for the different crystal phases of iron oxide.[147,208-211] The disagreements of previous results are summarized in **Table 3** for FeO, α- and γ-Fe_2O_3, and Fe_3O_4. In addition to the pre-peak / main peak energy difference ΔE_1 we have used previously (e.g. Chapter 3 and 4) to determine the iron oxide phase, some studies with higher energy resolution report that the pre-peak splits into two narrow peaks separated by ΔE_2. Our EEL spectra do not have sufficient resolution to resolve the ΔE_2 splitting.

In an attempt to resolve some the discrepancies in the literature and develop a reliable standard for identifying differentiating α-Fe_2O_3 from Fe_3O_4 for our own use, we applied STEM EELS to study Fe_3O_4 and α-Fe_2O_3 standards, bought from Sigma-Aldrich. O K edges were acquired from several crystallographic orientations from each material with dispersion 0.05 eV/channel to obtain 0.7 eV energy unlike the usual conditions described in Chapter 2.4. Two different convergence angles, 24.5 and 10.5 mrad were used, and five different collection angles, 52 mrad, 41 mrad, 31.7 mrad, 25 mrad and 19.7 mrad were used. Probe current of 25 pA (spotsize 8) was used to minimize the beam damage to the Fe oxides standard.

Table 3 ΔE_1 (splitting between pre peak and main peak) and ΔE_2 (splitting of the pre peak) for different Fe oxides compound

Compounds	ΔE_1 (eV)	ΔE_2 (eV)	Energy resolution (eV)/ Method	References
Fe_3O_4	10.7+/- 0.2	N/A	1/EELS	[147]
	10.3	0.7	0.5/XAS	[208]
	11.1	N/A	0.5/XAS	[209]
	11.3	0.6	0.5/XAS	[210]
α-Fe_2O_3	11.0+/- 0.2	N/A	1/EELS	[147]
	11.1	1.3	0.5/XAS	[208]
	11.6	N/A	0.5/XAS	[209]
	11.2	1.3	0.5/XAS	[210]
FeO	9.0 +/- 0.2	N/A	1/EELS	[147]
	9.0	N/A	0.5/XAS	[208]
	10.2	N/A	0.5/XAS	[209]
	9.2	1.2	0.5/XAS	[210]
γ-Fe_2O_3	10.9 +/-0.2	N/A	1/EELS	[147]

Results and Discussions

HRSTEM images in **Figure 6.1** (a) and (d) show Fe_3O_4 along the [111] and [110] zone axes, respectively. EEL spectra in **Figure 6.1** (b) and (c) were taken along Fe_3O_4 along [111] zone axis, using convergence angle 24.5 mrad and 10.5 mrad, respectively. EEL spectra in Figure (e) and (f) were acquired under the same conditions but along the Fe_3O_4 [110] zone axis. Each figure (from **Figure 6.1** (b) (c) and (e) (f)) contains four EEL spectra, which were taken using different collection angles. Every spectrum contains four peaks labeled with numbers 1 to 4 as shown in **Figure 6.1** (b). Peak 1 is the pre peak due to unoccupied O *2p* states hybridized

with Fe *3d* states. Peak 2 is the main peak due to the unoccupied O *2p* hybridized with Fe *4sp* states. The main peak also involves multiple scattering events. Peak 3 and peak 4 arise from the single scattering event and are related to the scattering within the first oxygen shell of the Fe oxide compounds.[208,209] Therefore, the positions of peak 3 and 4 are expected to be different for different Fe oxides. In **Figure 6.1** (b) and (e), there is a 10 eV splitting between the main peak and pre peak for both [111] and [110] orientations of Fe_3O_4. In Figure 6.1 (b) and (c), the pre peaks (peak 1) are unchanged when changing collection angles and convergence angles. However, a shoulder on peak 2, labeled by the black arrows, changes with collection angle, and the changes are only visible when the convergence angle is 24.5 mrad. In EEL spectra taken along the Fe_3O_4 [110] zone axis, similar phenomenon are shown in **Figure 6.1** (e) and (f).

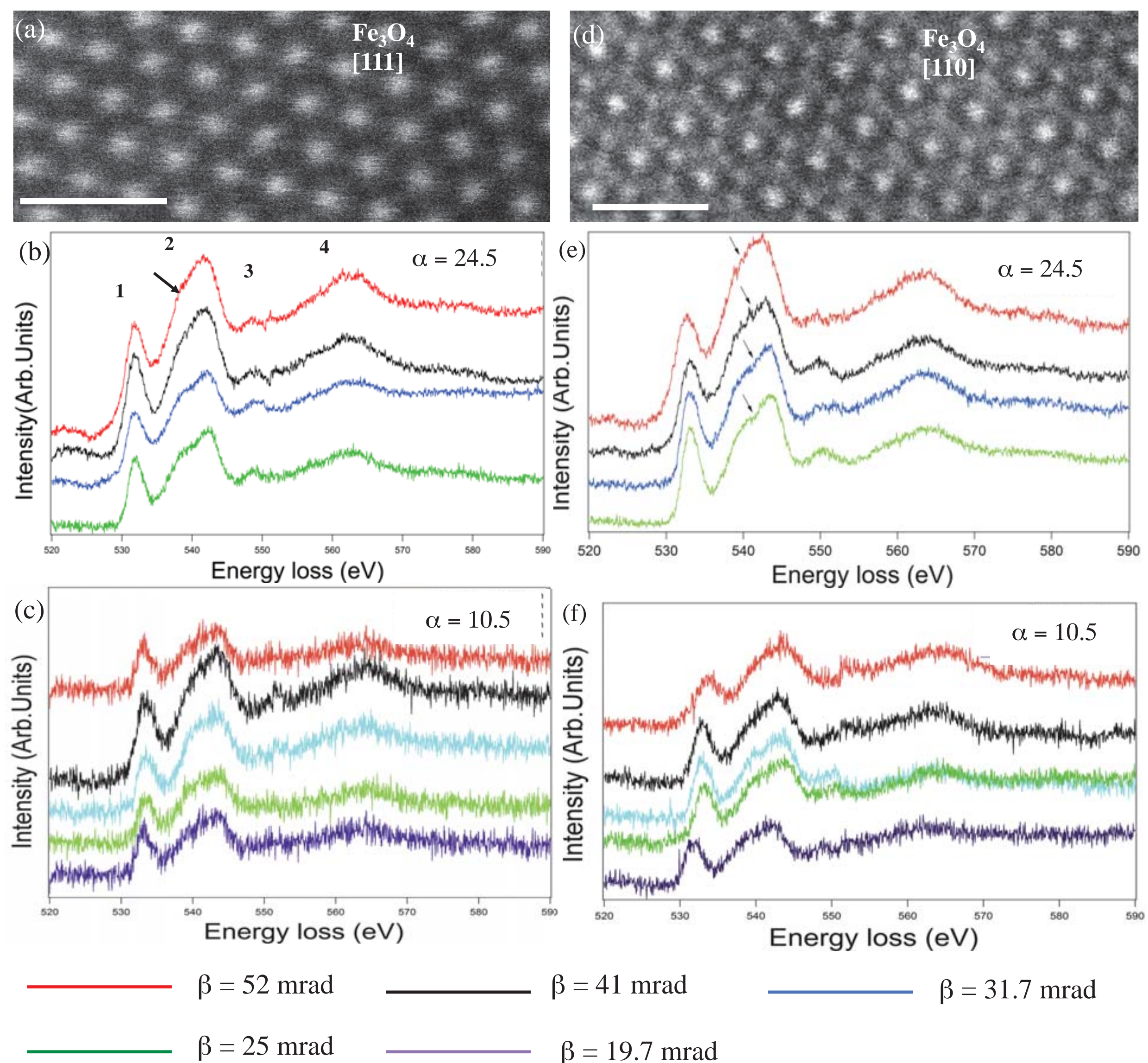

Figure 6.1 (a) and (d) are HRSTEM images along the [111] and [110] zone axes, respectively. EEL spectra in (b) and (c) were taken along the zone axis shown in (a), but with 24.5 mrad and 10.5 mrad convergence angles (α), respectively. EEL spectra in (e) and (f) were taken along the zone axis shown in (d) with 24.5 mrad and 10.5 mrad, respectively. Each figure from (b) (c) and (e) (f) contains spectra corresponding to different collection angles (β) as labeled at the bottom of the figures. Scale bars in (a) and (b) are 1 nm.

The shoulder labeled by black arrows in Figure 6.1 (c) could arise from a non-dipole. As shown in **Figure 6.2**, the entrance aperture selects what scattered vector **k** goes into the EELS spectrometer. Convergence angle (α) and collection angle (β) also affect the ELNES. Normally, the core level electrons transitions obey the dipole transition rule ($\Delta l = \pm 1$), but it is only true

when $|\mathbf{q}\cdot \boldsymbol{r_c}| \ll 1$, in which **q** is the momentum transfer (**q** = $k\times\Delta E/2E_0$) as defined in **Figure 6.2** and $\mathbf{r_c}$ is the radius of the core. In **Figure 6.2 (b)**, this requirement means the scattering angle θ has to be $\ll (\frac{E}{E_0})^{1/2}$, where E is the energy of inelastic scattered electron and E_0 is the incident electron energy.[212] For example, O K edge is at ~530 eV, so θ has to be ≪ 51 mrad. In our experimental setup, the collection angle β is equal to 52 mrad, which is sufficiently large to allow the detection of non-dipole transitions. Therefore, the shoulder feature labeled by black arrows in **Figure 6.1** (b) can be a result of non-dipole transition. This hypothesis could be tested by theoretical calculations.

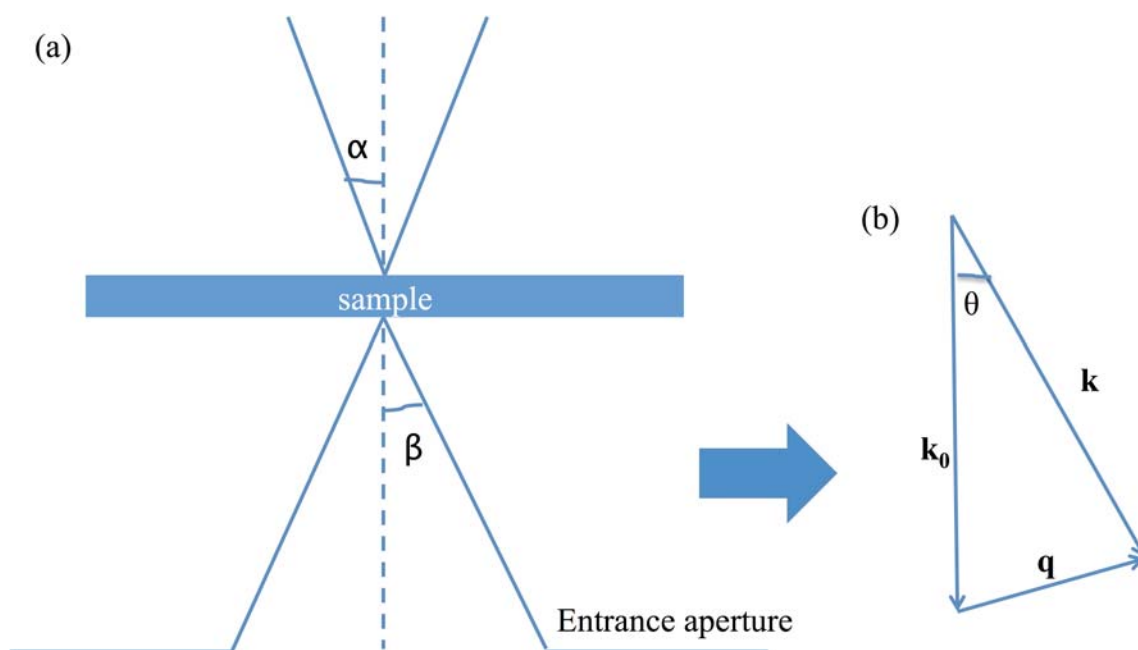

Figure 6.2 A schematic view of geometry of STEM EELS without any lenses, which shows the convergence angle α and collection angle β. (b) Definitions of the incident beam $\mathbf{k_0}$, scattered beam **k** and the momentum transfer **q.**

Because [111] Fe_2O_3 in Figure 6.3 (a) and [110] Fe_3O_4 in Figure 6.1 (d) have indistinguishable STEM images, we also studied the effect of crystal orientation on the O K-edge ELNES. As shown in **Figure 6.1** (b) and (e), it has little effect on the fine structure of the O K edge taken under our experimental conditions. In Fermi's golden rule in **Equation (3.14),** the

unoccupied final state reflects any anisotropy in the crystal. Thus if the DOS of the unoccupied states is anisotropic, the resulting ELNES will depend on the crystal orientation. The choice of a scattering vector allows the selection of a particular final crystal orbital for the transitions and thus affects ELNES. This effect can be significant for materials with strong anisotropy such as BN[213] and graphite[212]. In our case, no obvious difference was observed for Fe_3O_4 between two orientations in Figure 6.1, as expected for the high-symmetry cubic space group.

EEL spectra from Fe_2O_3 are similar to spectra from Fe_3O_4, comparing the spectra in **Figure 6.3** (b) and (c). The peak splitting between pre peak and the main peak in Fe_2O_3 is the same as the splitting in Fe_3O_4, which means that the peak splitting value is not a reliable way to distinguish Fe_3O_4 from Fe_2O_3.

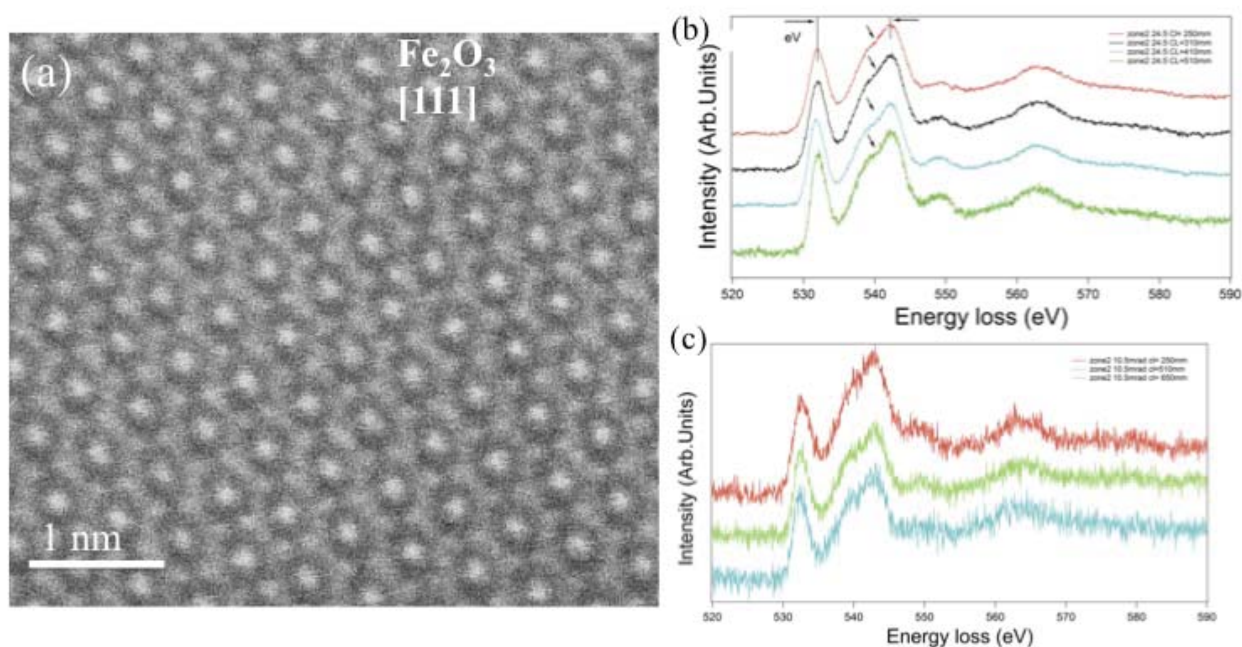

Figure 6.3 (a) HRTEM image of Fe_2O_3 along [111]. EELS spectra along Fe_2O_3 [111] are shown in (b) and (c). In (a) we kept convergence angle to be 24.5 mrad and varied the collection angles. The arrows on the main peak indicate the changes of find features according to the collection angles. In (b), we kept convergence angle to be 10.5 mrad and varied the collection angles.

EEL spectra from Fe_3O_4 and Fe_2O_3 each in two different orientations are compared directly in **Figure 6.4**. As pointed out earlier, both Fe_3O_4 and Fe_2O_3 a pre peak and the main peak. However, there are two differences in the spectra between Fe_3O_4 to Fe_2O_3. First, the position of the peak 3 and peak 4 in Fe_3O_4 shifts 0.64 eV to lower energy compared with Fe_2O_3, as labeled by the solid black lines. Positions and shapes of peak 3 and peak 4 were not studied in detail in the previous reports.[147,208-211] Therefore, our study reveals a difference that is significant to distinguish Fe_2O_3 from Fe_3O_4.

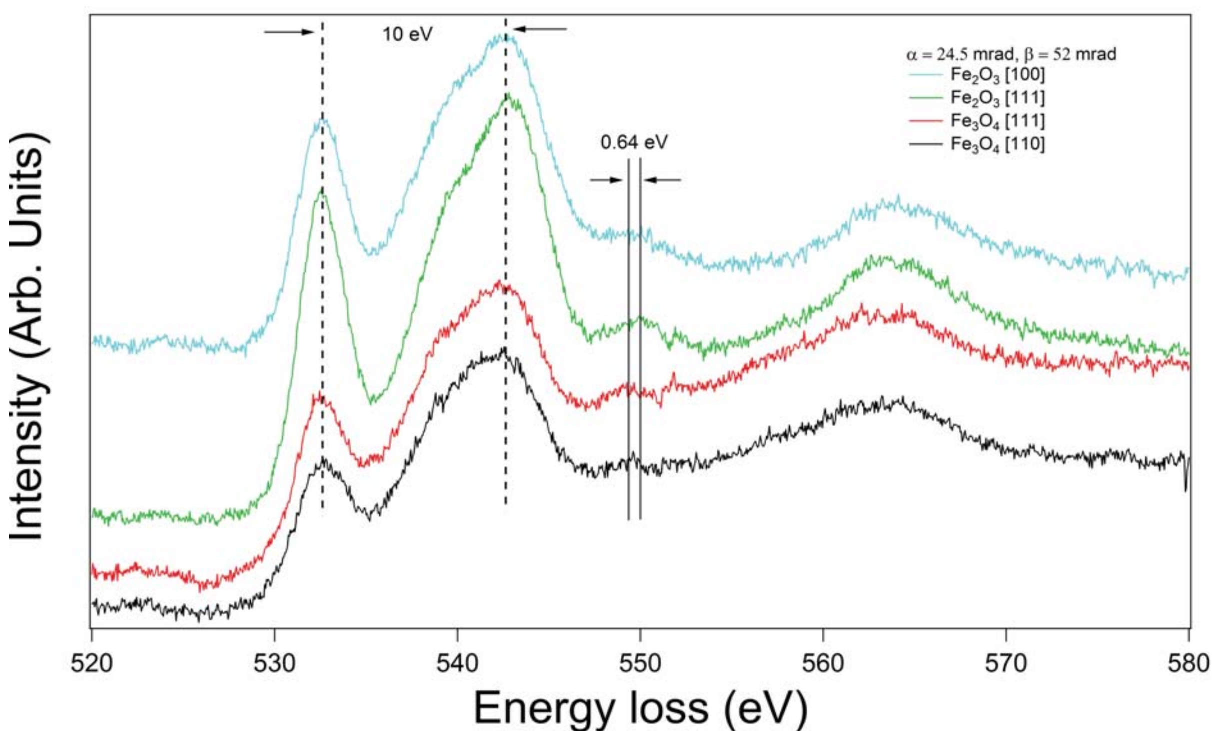

Figure 6.4 EEL spectra from Fe_3O_4 and Fe_2O_3 with different zone axis under the same experimental conditions: convergence angle α = 24.5 mrad, collection angle β = 52.

Second, the intensity ratio between the pre peak and main peak differs sufficiently sufficiently to distinguish Fe_3O_4 from Fe_2O_3. However, determining the exact background underneath peak 1 and peak 2 is difficult, so this method is difficult to transfer from one set of experimental conditions to another, and possibly difficult to transfer from microscope to

microscope. For spectra acquired under exactly the same conditions on the same microscope, we can compare the experimental data with the spectrum acquired on the standard by overlaying them together. We have applied this idea to compare the spectra acquired in Fe_3O_4 thin film and standard, and found a perfect agreement in the intensity ratio between these two systems under the same experimental conditions as shown in **Figure 4.1.5**.

Conclusions

To conclude, we have studied the ENLES of O K edges for Fe_3O_4 and Fe_2O_3 with different convergence angles and collection angles. We have found that peak 3 serves as a good criterion to distinguish Fe_3O_4 from Fe_2O_3, which was studied in previous reports. In addition, the intensity ratio of the pre peak and main peak is also a good reference to distinguish these two materials. We found that at large big convergence angles, the shoulder on the main peak (peak 2) changed dramatically with deceasing collection angles for both Fe_3O_4 and Fe_2O_3. This change may correspond to suppression of the non-dipole transition captured at the large collection angles.

Chapter 7 References

[1] S. Yuasa and D. Djayaprawira, Journal of Physics D: Applied Physics **40**, R337 (2007).

[2] M. Julliere, Physics Letters A **54**, 225–226 (1975).

[3] X.-F. Han, A. Yu, M. Oogane, J. Murai, T. Daibou, and T. Miyazaki, Phys. Rev. B **63**, (2001).

[4] M. Bowen, M. Bibes, A. Barthélémy, J.-P. Contour, A. Anane, Y. Lemaître, and A. Fert, Applied Physics Letters **82**, 233–235 (2003).

[5] E.Y. Tsymbal, O.N. Mryasov, and P.R. LeClair, Journal of Physics-Condensed Matter **15**, R109–R142 (2003).

[6] M.B. Stearn, Journal of Magnetism and Magnetic Materials **5**, 167–171 (n.d.).

[7] J. Slonczewski, Phys. Rev. B **39**, 6995–7002 (1989).

[8] G. Prinz, Science **282**, 1660–1663 (1998).

[9] M. Tondra, J. Daughton, D. Wang, R. Beech, A. Fink, and J. Taylor, Journal of Applied Physics **83**, 6688–6690 (1998).

[10] S. Bader and S. Parkin, Annual Review of Condensed Matter Physics **1**, 71–88 (2010).

[11] T. Miyazaki and N. Tezuka, Journal of Magnetism and Magnetic Materials **139**, L231–L234 (1995).

[12] J. Moodera, L. Kinder, T. Wong, and R. Meservey, Phys. Rev. Lett. **74**, 3273 (1995).

[13] W. Dexin, C. Nordman, J. Daughton, Q. Zhenghong, and J. Fink, Magnetics, IEEE Transactions on **40**, 2269–2271 (2004).

[14] H. Xiang, C. Ji, J. Yang, and Y. Chang, Applied Physics a: Materials Science &Amp; Processing **98**, 707–710 (2010).

[15] S. Yuasa, T. Nagahama, A. Fukushima, Y. Suzuki, and K. Ando, Nat Mater **3**, 868–871 (2004).

[16] S. Parkin, C. Kaiser, A. Panchula, P. Rice, B. Hughes, M. Samant, and S.-H. Yang, Nat Mater **3**, 862–867 (2004).

[17] W. Butler, X. Zhang, T. Schulthess, and J. MacLaren, Phys. Rev. B **63**, 054416 (2001).

[18] J. Mathon and A. Umerski, Phys. Rev. B **63**, (2001).

[19] S. Ikeda, J. Hayakawa, Y. Ashizawa, Y.M. Lee, K. Miura, H. Hasegawa, M. Tsunoda, F. Matsukura, and H. Ohno, Applied Physics Letters **93**, 082508–082508–3 (2008).

[20] W. Butler, X. Zhang, T. Schulthess, D. Nicholson, A. Oparin, and J. MacLaren, in (1999), pp. 5834–5839.

[21] J. Moodera and G. Mathon, Journal of Magnetism and Magnetic Materials **200**, 248–273 (1999).

[22] H. Xiang, F. Shi, M. Rzchowski, P. Voyles, and Y. Chang, Applied Physics Letters **97**, 092508–092503 (2010).

[23] H. Xiang, F.-Y. Shi, C. Zhang, M.S. Rzchowski, P.M. Voyles, and Y.A. Chang, Scripta Materialia **65**, 739–742 (2011).

[24] H. Xiang, F. Shi, M. Rzchowski, P. Voyles, and Y. Chang, Journal of Applied Physics **109**, 07E126 (2011).

[25] H. Xiang, F.-Y. Shi, M.S. Rzchowski, P.M. Voyles, and Y.A. Chang, Appl. Phys. A **110**, 487–492 (2012).

[26] F. Shi, H. Xiang, J.J. Yang, M.S. Rzchowski, Y.A. Chang, and P.M. Voyles, Journal of Magnetism and Magnetic Materials **324**, 1837–1844 (2012).

[27] J. Moodera, J. Nassar, and G. Mathon, Annual Review of Materials Science **29**, 381–432 (2003).

[28] R. Meservey and P. Tedrow, Physics Reports **238**, 173–243 (1994).

[29] S. Parkin, J. Xin, C. Kaiser, A. Panchula, K. Roche, and M. Samant, Proceedings of the IEEE **91**, 661–680 (2003).

[30] J. De Teresa, Barth, eacute, A. my, A. Fert, J. Contour, R. Lyonnet, F. Montaigne, P. Seneor, Vaur, egrave, and A. s, Phys. Rev. Lett. **82**, 4288 (1999).

[31] E. Tsymbal and D. Pettifor, Journal of Physics-Condensed Matter **9**, L411 (1997).

[32] M. Sharma, S. Wang, and J. Nickel, Phys. Rev. Lett. **82**, 616 (1999).

[33] H. Itoh and J.-I. Inoue, Surface Science **493**, 748–756 (2001).

[34] E.Y. Tsymbal, I.I. Oleinik, and D.G. Pettifor, Journal of Applied Physics **87**, 5230 (2000).

[35] C. Tiusan, M. Sicot, M. Hehn, C. Belouard, S. Andrieu, F. Montaigne, and A. Schuhl, Applied Physics Letters **88**, 062512–062513 (2006).

[36] P. LeClair, H. Swagten, J. Kohlhepp, R. van de Veerdonk, and W. de Jonge, Phys. Rev. Lett. **84**, 2933–2936 (2000).

[37] P. LeClair, B. Hoex, H. Wieldraaijer, J. Kohlhepp, H. Swagten, and W. de Jonge, Phys. Rev. B **64**, 100406 (2001).

[38] C. Shang, J. Nowak, R. Jansen, and J. Moodera, Phys. Rev. B **58**, R2917 (1998).

[39] P. Mavropoulos, M. Ležaić, and S. Blügel, Phys. Rev. B **72**, (2005).

[40] T. Ishikawa, N. Itabashi, T. Taira, K.-I. Matsuda, T. Uemura, and M. Yamamoto, Applied Physics Letters **94**, 092503–092503 (2009).

[41] H.-X. Liu, Y. Honda, K.-I. Matsuda, M. Arita, T. Uemura, and M. Yamamoto, Japanese Journal of Applied Physics **51**, 093004 (2012).

[42] S. Parkin, C. Kaiser, A. Panchula, P. Rice, B. Hughes, M. Samant, and S.-H. Yang, Nat Mater **3**, 862–867 (2004).

[43] Y. Miura, K. Abe, and M. Shirai, Phys. Rev. B **83**, (2011).

[44] S. Zhang, P. Levy, A. Marley, and S. Parkin, Phys. Rev. Lett. **79**, 3744–3747 (1997).

[45] W. Wulfhekel, H.F. Ding, and J. Kirschner, Journal of Magnetism and Magnetic Materials **242-245**, 47–52 (2002).

[46] P. LeClair, J. Kohlhepp, C. van de Vin, H. Wieldraaijer, H. Swagten, W. de Jonge, A. Davis, J. MacLaren, J. Moodera, and R. Jansen, Phys. Rev. Lett. **88**, (2002).

[47] J.M. de Teresa, Science **286**, 507–509 (1999).

[48] Z. Zhang and S. Satpathy, Phys. Rev. B **44**, 13319 (1991).

[49] Y. Dedkov, U. Rüdiger, and G. Güntherodt, Phys. Rev. B **65**, (2002).

[50] P.-H. Huang, C.-H. Lai, and R.T. Huang, Journal of Applied Physics **97**, 10C311 (2005).

[51] L.B. Zhao, W.B. Mi, E.Y. Jiang, and H.L. Bai, Applied Physics Letters **91**, 052113 (2007).

[52] R. Arras, L. Calmels, and B. Warot-Fonrose, Phys. Rev. B **81**, 104422 (2010).

[53] P. Seneor, A. Fert, J.-L. Maurice, F. Montaigne, F. Petroff, and A. Vaurès, Applied Physics Letters **74**, 4017–4019 (1999).

[54] J. Du, W. Sheng, L. Sun, B. You, M. Lu, A. Hu, Q. Xu, Y. Wang, Z. Zhang, and J. Xiao, Physica Status Solidi (a) **199**, 289–293 (2003).

[55] K.-I. Aoshima and S.X. Wang, Journal of Applied Physics **91**, 7146–7148 (2002).

[56] H. Matsuda, M. Takeuchi, H. Adachi, M. Hiramoto, N. Matsukawa, A. Odagawa, K. Setsune, and H. Sakakima, Jpn. J. Appl. Phys. **41**, 4 (2002).

[57] Y. Komasaki, M. Tsunoda, S. Isogami, and M. Takahashi, Journal of Applied Physics **105**, 07C928–07C928–3 (2009).

[58] Z. Liu, H. Hashimoto, E. Sukedai, M. Song, K. Mitsuishi, and K. Furuya, Phys. Rev. Lett. **90**, 255504 (2003).

[59] D. Margulies, F. Parker, F. Spada, R. Goldman, J. Li, R. Sinclair, and A. Berkowitz, Phys.

Rev. B **53**, 9175–9187 (1996).

[60] D. Margulies, F. Parker, M. Rudee, F. Spada, J. Chapman, P. Aitchison, and A. Berkowitz, Phys. Rev. Lett. **79**, 5162 (1997).

[61] S. Kale, S. Bhagat, S. Lofland, T. Scabarozi, S. Ogale, A. Orozco, S. Shinde, T. Venkatesan, B. Hannoyer, B. Mercey, and W. Prellier, Phys. Rev. B **64**, (2001).

[62] W. Eerenstein, T. Palstra, S. Saxena, and T. Hibma, Phys. Rev. Lett. **88**, 247204 (2002).

[63] F. Voogt, T. Palstra, L. Niesen, O. Rogojanu, M. James, and T. Hibma, Phys. Rev. B **57**, R8107 (1998).

[64] S. Kokado, N. Fujima, K. Harigaya, H. Shimizu, and A. Sakuma, Phys. Rev. B **73**, 172410 (2006).

[65] W. Zhou, L.-J. Qu, Q.-M. Zhang, and D.-S. Wang, Phys. Rev. B **40**, 6393 (1989).

[66] M. Tsunoda, Y. Komasaki, S. Kokado, S. Isogami, C.-C. Chen, and M. Takahashi, Applied Physics Express **2**, 083001 (2009).

[67] A. Narahara, K. Ito, T. Suemasu, Y. Takahashi, A. Ranajikanth, and K. Hono, Applied Physics Letters **94**, 202502–202503 (2009).

[68] X.G. Ma, J.J. Jiang, P. Liang, J. Wang, Q. Ma, and Q.K. Zhang, Journal of Alloys and Compounds **480**, 475–480 (2009).

[69] K. Sunaga, M. Tsunoda, K. Komagaki, Y. Uehara, and M. Takahashi, Journal of Applied Physics **102**, – (2007).

[70] R. de Groot, F. Mueller, P. Engen, and K. Buschow, Phys. Rev. Lett. **50**, 2024 (1983).

[71] W. Pickett and J. Moodera, Physics Today **54**, 39–44 (2001).

[72] I. Galanakis and P. H Dederichs, *Half-Metallicity and Slater-Pauling Behavior in the Ferromagnetic Heusler Alloys* (2005), pp. 1–39.

[73] S. Bader and S. Parkin, Annual Review of Condensed Matter Physics **1**, 71–88 (2010).

[74] A. Hütten, S. Kämmerer, J. Schmalhorst, and G. Reiss, *Heusler Alloyed Electrodes Integrated in Magnetic Tunnel-Junctions* (2005), pp. 241–265.

[75] P. Brown, K. Neumann, P. Webster, and K. Ziebeck, Journal of Physics-Condensed Matter **12**, 1827–1835 (2000).

[76] V. Irkhin and M. Katsnel'son, Physics-Uspekhi **37**, 659–676 (1994).

[77] S. Kammerer, A. Thomas, A. Hutten, and G. Reiss, Applied Physics Letters **85**, 79–81 (2004).

[78] M. Yamamoto, T. Marukame, T. Ishikawa, K. Matsuda, T. Uemura, and M. Arita, Journal of Physics D: Applied Physics **39**, 824–833 (2006).

[79] T. Marukame, T. Ishikawa, K. Matsuda, T. Uemura, and M. Yamamoto, Applied Physics Letters **88**, – (2006).

[80] P.J. Webster, J. Phys. Chem. Solids **32**, 1221–1231 (1971).

[81] S. Picozzi, A. Continenza, and A. Freeman, Phys. Rev. B **69**, 094423 (2004).

[82] S. Picozzi, A. Continenza, and A. Freeman, Phys. Rev. B **69**, 094423 (2004).

[83] B. Ravel, M. Raphael, V. Harris, and Q. Huang, Phys. Rev. B **65**, (2002).

[84] W. Butler, X.G. Zhang, T. Schulthess, and J. MacLaren, Phys. Rev. B **63**, 054416 (2001).

[85] W. Butler, X. Zhang, T. Schulthess, D. Nicholson, A. Oparin, and J. MacLaren, in (1999), pp. 5834–5839.

[86] S. Yuasa, A. Fukushima, H. Kubota, Y. Suzuki, and K. Ando, Applied Physics Letters **89**, 042505–042503 (2006).

[87] S. Yuasa, Y. Suzuki, T. Katayama, and K. Ando, Applied Physics Letters **87**, 242503–242503 (2005).

[88] Y. Miura, H. Uchida, Y. Oba, K. Abe, and M. Shirai, Phys. Rev. B **78**, (2008).

[89] X. Zhang, W. Butler, and A. Bandyopadhyay, Phys. Rev. B **68**, 092402 (2003).

[90] C. Tusche, H. Meyerheim, N. Jedrecy, G. Renaud, A. Ernst, J. Henk, P. Bruno, and J. Kirschner, Phys. Rev. Lett. **95**, 176101 (2005).

[91] P.-J. Zermatten, F. Bonell, S. Andrieu, M. Chshiev, C. Tiusan, A. Schuhl, and G. Gaudin, Applied Physics Express **5**, 023001 (2012).

[92] S. Yuasa, T. Nagahama, A. Fukushima, Y. Suzuki, and K. Ando, Nat Mater **3**, 868–871 (2004).

[93] P.M. Voyles, J.L. Grazul, and D.A. Muller, Ultramicroscopy **96**, 251–273 (2003).

[94] A. Petford-Long and A. Chiaramonti, Annual Review of Materials Research **38**, 559–584 (2008).

[95] M. De Graef, (2003).

[96] A. Ramos, J. Moussy, M. Guittet, A. Bataille, M. Gautier-Soyer, M. Viret, C. Gatel, P. Bayle-Guillemaud, and E. Snoeck, Journal of Applied Physics **100**, 103902–103908 (2006).

[97] D.B.W.A.C.B. Carter, *TRANSMISSION ELECTRON MICROSCOPY, II Diffraction* (n.d.).

[98] S. Pennycook, M. Chisholm, A. Lupini, M. Varela, A. Borisevich, M. Oxley, W. Luo, K. van Benthem, S.-H. Oh, D. Sales, S. Molina, J. García-Barriocanal, C. Leon, J. Santamaría, S. Rashkeev, and S. Pantelides, Philosophical Transactions of the Royal Society a: Mathematical, Physical and Engineering Sciences **367**, 3709–3733 (2009).

[99] S. Pennycook, (1999).

[100] U. Falke, A. Bleloch, M. Falke, and S. Teichert, Phys. Rev. Lett. **92**, 116103 (2004).

[101] K. van Benthem and S. Pennycook, Applied Physics a: Materials Science &Amp; Processing **96**, 161–169 (2009).

[102] A. Bleloch and A. Lupini, Materials Today **7**, 42–48 (2004).

[103] S. Findlay, N. Shibata, H. Sawada, E. Okunishi, Y. Kondo, and Y. Ikuhara, Ultramicroscopy **110**, 903–923 (2010).

[104] S. Findlay, N. Shibata, H. Sawada, E. Okunishi, Y. Kondo, and Y. Ikuhara, Ultramicroscopy **110**, 903–923 (2010).

[105] J. Kirkland, Plenum Press (1998).

[106] William and Carter, *TRANSMISSION ELECTRON MICROSCOPY, IV Spectroscopy* (1995).

[107] J. LeBeau and S. Stemmer, Ultramicroscopy **108**, 1653–1658 (2008).

[108] LeBeau J, Findlay S, Allen L, and Stemmer S, Microsc Microanal **15**, 494–495 (2009).

[109] J.M. Zuo and J.C.H. Spence, Ultramicroscopy **35**, 185–196 (1991).

[110] S.C.C.R.F.E. T Malis, Journal of Electron Microscopy Technique **Vol 8**, (2005).

[111] R.F. Egerton, Electron Energy loss Spectroscopy (1996).

[112] J. LeBeau, S. Findlay, L. Allen, and S. Stemmer, Ultramicroscopy **110**, 118–125 (2010).

[113] J. Hwang, J.Y. Zhang, J. Son, and S. Stemmer, Applied Physics Letters **100**, 191909–191909–3 (2012).

[114] N.D. Browning, M.F. Chisholm, and S.J. Pennycook, Nature **366**, 143–146 (1993).

[115] P. Rez, J. Bruley, P. Brohan, M. Payne, and L.A.J. Garvie, Ultramicroscopy **59**, 159–167 (1995).

[116] P. Rez and D.A. Muller, Annual Review of Materials Research **38**, 535–558 (2008).

[117] S. Pennycook, M. Varela, A. Lupini, M. Oxley, and M. Chisholm, Journal of Electron Microscopy **58**, 87–97 (2009).

[118] A. Maigne and R.D. Twesten, Journal of Electron Microscopy **58**, 99–109 (2009).

[119] W. Sigle, Annual Review of Materials Research **35**, 239–314 (2005).

[120] M. Bosman, M. Watanabe, D. Alexander, and V. Keast, Ultramicroscopy **106**, 1024–1032

(2008).

[121] C. Park, Y. Peng, J.-G. Zhu, D. Laughlin, and R. White, Journal of Applied Physics **97**, 10Q515 (2005).

[122] K.-I. Aoshima and S. Wang, Journal of Applied Physics **93**, 7954–7956 (2003).

[123] T. Kado, Applied Physics Letters **92**, 092502–092502–3 (2008).

[124] P. Seneor, A. Fert, J.-L. Maurice, F. Montaigne, F. Petroff, and A. Vaurès, Applied Physics Letters **74**, 4017–4019 (1999).

[125] S. Yuasa, T. Nagahama, A. Fukushima, Y. Suzuki, and K. Ando, Nat Mater **3**, 868–871 (2004).

[126] D.D. Djayaprawira, K. Tsunekawa, M. Nagai, H. Maehara, S. Yamagata, N. Watanabe, S. Yuasa, Y. Suzuki, and K. Ando, Applied Physics Letters **86**, 092502 (2005).

[127] A. Fujimori, M. Saeki, N. Kimizuka, M. Taniguchi, and S. Suga, Phys. Rev. B **34**, 7318–7328 (1986).

[128] W. Eerenstein, T. Palstra, T. Hibma, and S. Celotto, Phys. Rev. B **68**, 014428 (2003).

[129] S.K. Arora, Han-Chun Wu, Hongzhi Yao, W.Y. Ching, R.J. Choudhary, I.V. Shvets, and O.N. Mryasov, Ieee Transactions on Magnetics **44**, 2628–2631 (n.d.).

[130] H. Xiang, F. Shi, M. Rzchowski, P. Voyles, and Y. Chang, Applied Physics Letters **97**, 092508–092503 (2010).

[131] H. Yan, M. Zhang, and H. Yan, Journal of Magnetism and Magnetic Materials **321**, 2340–2344 (2009).

[132] M.L. Paramês, J. Mariano, Z. Viskadourakis, N. Popovici, M.S. Rogalski, J. Giapintzakis, and O. Conde, Applied Surface Science **252**, 4610–4614 (2006).

[133] S.S.A. Hassan, X. Yongbing, W. Jing, and S.M. Thompson, Ieee Transactions on Magnetics

45, 4357–4359 (2009).

[134] Y. Lu, J. Claydon, Y. Xu, S. Thompson, K. Wilson, and G. van der Laan, Phys. Rev. B **70**, 233304 (2004).

[135] P.K.J. Wong, W. Zhang, X.G. Cui, Y.B. Xu, J. Wu, Z.K. Tao, X. Li, Z.L. Xie, R. Zhang, and G. van der Laan, Phys. Rev. B **81**, (2010).

[136] K. Mori, M. Yamazaki, T. Hiraki, H. Matsuyama, and K. Koike, Phys. Rev. B **72**, (2005).

[137] H.J. Kim, J.H. Park, and E. Vescovo, Phys. Rev. B **61**, 15284–15287 (2000).

[138] R. Dehoff, *Thermodynamics in Materials Science*, second edition (CRC Press, 2006, Boca Raton, n.d.).

[139] K. Jagannadham, J. Narayan, R. Chowdhury, Z. Tsvetanka, and P. Tiwari, Journal of Electronic Materials **23**, 861–874 (1994).

[140] H. Xiang, C. Ji, J. Yang, and Y. Chang, Applied Physics a: Materials Science &Amp; Processing **98**, 707–710 (2010).

[141] J. Narayan and B. Larson, Journal of Applied Physics **93**, 278–285 (2003).

[142] J. Orna, P. Algarabel, L. Morellón, J. Pardo, J. De Teresa, R. López Antón, F. Bartolomé, L. García, J. Bartolomé, J. Cezar, and A. Wildes, Phys. Rev. B **81**, 144420 EP– (2010).

[143] J. Moussy, S. Gota, A. Bataille, M. Guittet, M. Gautier-Soyer, F. Delille, B. Dieny, F. Ott, T. Doan, P. Warin, P. Bayle-Guillemaud, C. Gatel, and E. Snoeck, Phys. Rev. B **70**, 174448 (2004).

[144] D. Margulies, F. Parker, M. Rudee, F. Spada, J. Chapman, P. Aitchison, and A. Berkowitz, Phys. Rev. Lett. **79**, 5162 (1997).

[145] V. Brabers, Physica B: Condensed Matter **205**, 143–152 (1995).

[146] T.C. Droubay, C.I. Pearce, E.S. Ilton, M.H. Engelhard, W. Jiang, S.M. Heald, E. Arenholz, V. Shutthanandan, and K.M. Rosso, Phys. Rev. B **84**, 125443 (2011).

[147] C. Colliex, T. Manoubi, and C. Ortiz, Phys. Rev. B **44**, 11402 (1991).

[148] H. Hoefer, G. Brey, B. Schulz-Dobrick, and R. Oberhaensli, Eur J Mineral **6**, 407–418 (1994).

[149] M. Sankararaman and D. Perry, Journal of Materials Science **27**, 2731–2733 (1992).

[150] Z. Ka-cedillakol, J. Sabol, and J. Honig, Phys. Rev. B **43**, 649 (1991).

[151] K. Lawless, Reports on Progress in Physics **37**, 231 (1974).

[152] H.G. Tompkins, Journal of Applied Physics **70**, 3876–3880 (1991).

[153] H.-Y. Chen and F.-H. Lu, J. Vac. Sci. Technol. A **23**, 1006–1009 (2005).

[154] C. Navío, J. Alvarez, M.J. Capitan, J. Camarero, and R. Miranda, Applied Physics Letters **94**, 263112–263112–3 (2009).

[155] X.L. Wu, W. Zhong, H.Y. Jiang, N.J. Tang, W.Q. Zou, and Y.W. Du, Journal of Magnetism and Magnetic Materials **281**, 77–81 (2004).

[156] J.Q. Xiao and C.L. Chien, Applied Physics Letters **64**, 384 (1994).

[157] M. Somers, B. Kooi, W. Sloof, and E. Mittemeijer, Surface and Interface Analysis **19**, 633–637 (1992).

[158] S. Matar, A. Houari, and M. Belkhir, Phys. Rev. B **75**, (2007).

[159] Y. Imai, Y. Takahashi, and T. Kumagai, Journal of Magnetism and Magnetic Materials **322**, 2665–2669 (2010).

[160] M. Matsuoka and K. Ono, Applied Physics Letters **49**, 1644–1646 (1986).

[161] L. Maya, M. Paranthaman, J.R. Thompson, T. Thundat, and R.J. Stevenson, Journal of Applied Physics **79**, 7905–7910 (1996).

[162] K. Ito, K. Harada, K. Toko, M. Ye, A. Kimura, Y. Takeda, Y. Saitoh, H. Akinaga, and T. Suemasu, Applied Physics Letters **99**, 252501–252501–3 (2011).

[163] J. Moodera, L. Kinder, T. Wong, and R. Meservey, Phys. Rev. Lett. **74**, 3273 (1995).

[164] J. Moodera, J. Nassar, and G. Mathon, Annual Review of Materials Science **29**, 381–432 (2003).

[165] K.-I. Jun, J. Lee, K. Shin, K. Rhie, and B. Lee, Journal of Magnetism and Magnetic Materials **286**, 158–161 (2005).

[166] J. Yang, A. Bengtson, C. Ji, D. Morgan, and Y. Chang, Journal of Applied Physics **103**, 056102–056103 (2008).

[167] J. Yang, H. Xiang, C. Ji, W. Stickle, D. Stewart, D. Ohlberg, R. Williams, and Y. Chang, Applied Physics Letters **95**, 233117–233113 (2009).

[168] S. Pennycook, M. Chisholm, A. Lupini, M. Varela, A. Borisevich, M. Oxley, W. Luo, K. van Benthem, S.-H. Oh, D. Sales, S. Molina, J. García-Barriocanal, C. Leon, J. Santamaría, S. Rashkeev, and S. Pantelides, Philosophical Transactions of the Royal Society a: Mathematical, Physical and Engineering Sciences **367**, 3709–3733 (2009).

[169] A. Ziegler, J.C. Idrobo, M.K. Cinibulk, C. Kisielowski, N.D. Browning, and R.O. Ritchie, Applied Physics Letters **88**, 041919 (2006).

[170] J. Yang, A. Bengtson, C. Ji, D. Morgan, and Y. Chang, Journal of Applied Physics **103**, 056102–056103 (2008).

[171] C. Colliex, T. Manoubi, and C. Ortiz, Phys. Rev. B **44**, 11402 (1991).

[172] M. Samant, J. Luning, J. Stohr, and S. Parkin, Applied Physics Letters **76**, 3097–3099 (2000).

[173] A. Griffiths and T. Walther, Journal of Physics: Conference Series **241**, 012017 (2010).

[174] K. Yoon, J. Park, J. Yang, C. Kim, and J. Hong, Journal of Applied Physics **91**, 7953–7955 (2002).

[175] V. Edlmayr, T.P. Harzer, R. Hoffmann, D. Kiener, C. Scheu, and C. Mitterer, J. Vac. Sci.

Technol. A **29**, 041506 (2011).

[176] Z. Zhang, S. Cardoso, P. Freitas, P. Wei, N. Barradas, and J. Soares, Applied Physics Letters **78**, 2911–2913 (2001).

[177] D. Margulies, F. Parker, M. Rudee, F. Spada, J. Chapman, P. Aitchison, and A. Berkowitz, Phys. Rev. Lett. **79**, 5162 (1997).

[178] J. Simons, The Journal of Physical Chemistry **36**, 652–657 (1932).

[179] J. Moodera, J. Nowak, and R. van de Veerdonk, Phys. Rev. Lett. **80**, 2941 (1998).

[180] R. Wasilewski, Journal of the American Chemical Society **75**, 1001–1002 (1953).

[181] P. Kofstad, *High-Temperature Oxidation of Metals* (1966).

[182] D.D. Wagman, W.H. Evans, V.B. Parker, R.H. Schumm, I. Halow, S.M. Bailey, K.L. Churney, and R.L. Nuttall, J. Phys. Chem. Ref. Data **18**, 1807 (1989).

[183] Z. Liu, H. Hashimoto, M. Song, K. Mitsuishi, and K. Furuya, Acta Materialia **52**, 1669–1674 (2004).

[184] E.Y. Tsymbal, I.I. Oleinik, and D.G. Pettifor, Journal of Applied Physics **87**, 5230–5232 (2000).

[185] K. Belashchenko, E. Tsymbal, I. Oleynik, and M. van Schilfgaarde, Phys. Rev. B **71**, (2005).

[186] B. Hulsen, M. Scheffler, and P. Kratzer, Phys. Rev. Lett. **103**, 046802 (2009).

[187] H.L. Yu, X.F. Jiang, Y. Zheng, and G.W. Yang, Journal of Physics D: Applied Physics **45**, 325002 (2012).

[188] T. Miyajima, M. Oogane, Y. Kotaka, T. Yamazaki, M. Tsukada, Y. Kataoka, H. Naganuma, and Y. Ando, Applied Physics Express **2**, 093001 (2009).

[189] B. Wu, H. Yuan, A. Kuang, H. Chen, and Y. Feng, Applied Surface Science, **258,** 4945–4951 (2012).

[190] T. Ishikawa, H.-X. Liu, T. Taira, K.-I. Matsuda, T. Uemura, and M. Yamamoto, Applied Physics Letters **95**, 232512–232513 (2009).

[191] M. Yamamoto, T. Ishikawa, T. Taira, G.-F. Li, K.-I. Matsuda, and T. Uemura, Journal of Physics-Condensed Matter **22**, 164212 (2010).

[192] H.-X. Liu, Y. Honda, T. Taira, K.-I. Matsuda, M. Arita, T. Uemura, and M. Yamamoto, Applied Physics Letters **101**, 132418 (2012).

[193] S. Findlay, N. Shibata, H. Sawada, E. Okunishi, Y. Kondo, and Y. Ikuhara, Ultramicroscopy **110**, 903–923 (2010).

[194] G. Duscher, S.J. Pennycook, N.D. Browning, R. Rupangudi, C. Takoudis, H.-J. Gao, and R. Singh, in *Characterization and Metrology for Ulsi Technology* (ASCE, 1998), pp. 191–195.

[195] P. Webster, Contemporary Physics **10**, 559–577 (1969).

[196] S. Ouardi, G.H. Fecher, B. Balke, A. Beleanu, X. Kozina, G. Stryganyuk, C. Felser, W. Klöß, H. Schrader, F. Bernardi, J. Morais, E. Ikenaga, Y. Yamashita, S. Ueda, and K. Kobayashi, Phys. Rev. B **84**, (2011).

[197] J. LeBeau, S. Findlay, X. Wang, A. Jacobson, L. Allen, and S. Stemmer, Phys. Rev. B **79**, 214110 (2009).

[198] J. LeBeau, S. Findlay, L. Allen, and S. Stemmer, Ultramicroscopy **110**, 118–125 (2010).

[199] Y. Miura, H. Uchida, Y. Oba, K. Nagao, and M. Shirai, Journal of Physics-Condensed Matter **19**, 365228 (2007).

[200] T. Saito, T. Katayama, D. Asakura, T. Koide, Y. Miura, and M. Shirai, Phys. Rev. B **81**, (2010).

[201] T. Saito, T. Katayama, A. Emura, N. Sumida, N. Matsuoka, T. Ishikawa, T. Uemura, M. Yamamoto, D. Asakura, and T. Koide, Journal of Applied Physics **103**, 07D712–07D712–3

(2008).

[202] A. Sakuma, Y. Toga, and H. Tsuchiura, Journal of Applied Physics **105**, 07C910–07C910–3 (2009).

[203] G.H. Fecher, B. Balke, S. Ouardi, C. Felser, G. Schonhense, E. Ikenaga, J.-J. Kim, S. Ueda, and K. Kobayashi, Journal of Physics D: Applied Physics **40**, 1576–1581 (2007).

[204] T.M. Nakatani, Y.K. Takahashi, T. Ishikawa, M. Yamamoto, and K. Hono, Journal of Magnetism and Magnetic Materials **322**, 357–361 (2010).

[205] E.J. Kirkland, Ultramicroscopy **102**, 199–207 (2005).

[206] R.F. Loane, E.J. Kirkland, and J. Silcox, Acta Crystallogr a Found Crystallogr **44**, 912–927 (1988).

[207] R. Egerton, *Electron Energy-Loss Spectroscopy in the Electron Microscope* (1996).

[208] F. de Groot, M. Grioni, J. Fuggle, J. Ghijsen, G. Sawatzky, and H. Petersen, Phys. Rev. B **40**, 5715–5723 (1989).

[209] Z.Y. Wu, Phys. Rev. B **55**, 2570–2577 (1997).

[210] J. Crocombette, M. Pollak, F. Jollet, N. Thromat, and M. Gautier-Soyer, Phys. Rev. B **52**, 3143 (1995).

[211] M. Pollak, M. GAUTIER, N. Thromat, S. Gota, W. MACKRODT, and V. SAUNDERS, Nuclear Instruments and Methods in Physics Research Section B: Beam Interactions with Materials and Atoms **97**, 383–386 (1995).

[212] R. Leapman, P. Fejes, and J. Silcox, Phys. Rev. B **28**, 2361–2373 (1983).

[213] C. Souche, B. Jouffrey, G. Hug, and M. Nelhiebel, *Micron,* **29**, No. 6, 419–424, (1998).